2011

Effect of initial conditions on molecular mixing in a high Schmidt-number Rayleigh-Taylor mixing layer

Lakshmi Ayyappa Raghu Mutnuri

Department:

EFFECT OF INITIAL CONDITIONS ON MOLECULAR MIXING IN A HIGH SCHMIDT-NUMBER RAYLEIGH-TAYLOR MIXING LAYER

by

LAKSHMI AYYAPPA RAGHU MUTNURI

A THESIS

Presented to the Faculty of the Graduate School of the

MISSOURI UNIVERSITY OF SCIENCE AND TECHNOLOGY

In Partial Fulfillment of the Requirements for the Degree

MASTER OF SCIENCE IN MECHANICAL ENGINEERING

2011

Approved by

Arindam Banerjee, Advisor
Bassem F. Armaly
Kakkattukuzhy M. Isaac

ABSTRACT

Characterizing molecular mixing in Rayleigh-Taylor instability (RTI) driven flows where the density and velocity fields are coupled is essential for developing exacting predictive models. Sensitivity of the Rayleigh Taylor mixing layer to initial conditions is a topic that is being explored extensively in interests of accurate turbulent mix model development and its direct consequence in various applications like deign of inertial confinement fuel capsule and atmospheric modeling. As part of the current work, an experimental investigation of the effect of initial conditions on molecular mixing in a low Atwood number ($\sim 7.5 \times 10^{-4}$), high Schmidt number (~ 1000), RTI driven mixing layer is undertaken. An experimental facility for observing the evolution of an RTI driven mixing layer to a buoyancy Reynolds number of ~ 10000 was developed. Diagnostics for measuring volume fraction evolution through passive scalar (Nigrosine) estimates and mixture fraction evolution through reactive scalar (Phenolphthalein) measurements were calibrated and established. The initial perturbations at the interface were modeled from the passive scalar runs and validated using an Implicit Large Eddy simulation (ILES). Molecular mixing parameter estimates were calculated by combining the results from the passive scalar and reactive scalar runs. An examination of molecular mixing measurements vis-à-vis variations in initial conditions has revealed that that the low wave number loading of the initial density perturbation spectrum has a profound effect on molecular mixing in the mixing layer. The variation was observed in both local and global mixing with possible implications pointing to the delay in mixing transition.

ACKNOWLEDGMENTS

I wish to express my sincere thanks to my advisor Prof. Arindam Banerjee who guided me throughout the Masters program and made it a memorable experience. He has always been extremely helpful, encouraging and a constant source of motivation. I would like to thank my committee members Prof. Bassem F. Armaly and Prof. Kakkattukuzhy M. Isaac for their support and cooperation. In addition, I express my sincere appreciation to Dr. Nicholas J. Mueschke for providing helpful suggestions during the project. I acknowledge the financial support from the University of Missouri Research Board (UMRB) and National Science Foundation (NSF) which made this work possible. I would also like to acknowledge my fellow members of Turbulent Mixing and Alternative Energetics Laboratory: Aaron, Suchi, Pamela, Varun and Tim for sharing useful thoughts, food and engaging in fruitful discussions over the duration of this work. I would like to extend a special thanks to my friend Deepak Somayajula for his classic company over the past decade. I would like to thank my parents for their constant support, cooperation and love; without them none of this would have been possible.

TABLE OF CONTENTS

Page

ABSTRACT iii

ACKNOWLEDGMENTS iv

LIST OF ILLUSTRATIONS vii

LIST OF TABLES ix

SECTION

1. INTRODUCTION 1
   1.1. OVERVIEW AND MOTIVATION 1
   1.2. THE RAYLEIGH-TAYLOR INSTABILITY 3
   1.3. PREVIOUS WORK 7
   1.4. CURRENT WORK 12
2. EXPERIMENTAL SET-UP 15
3. DIAGNOSTICS AND UNCERTAINITY IN MEASUREMENTS 22
   3.1. WORKING PRINCIPLE OF THE DIAGNOSTIC 22
   3.2. REACTION CHEMISTRY 23
   3.3. CALIBRATION PROCEDURE 24
   3.4. UNCERTAINTY QUANTIFICATION 26
4. RESULTS AND DISCUSSION 29
   4.1. MIXING LAYER GROWTH FROM PASSIVE SCALAR RUNS 30
      4.1.1. Qualitative Results From Passive Scalar 30
      4.1.2. Quantitative Results From Passive Scalar 32
   4.2. INITIAL CONDITION ESTIMATES FROM PASSIVE SCALAR RUNS 37
      4.2.1. Governing Equations. 38
      4.2.2. Simulation Setup. 39
      4.2.3. Simulation Results. 43
   4.3. CONCENTRATION MEASUREMENTS FROM REACTIVE SCALAR RUNS 44
      4.3.1. Qualitative Results From Reactive Scalar 44
      4.3.2. Quantitative Results From Reactive Scalar. 46

4.4. MIXING ESTIMATES 52
4.4.1. Local Mixing. 53
4.4.2. Global Mixing 57
5. CONCLUSIONS AND FUTURE WORK 62
5.1. SUMMARY 62
5.2. FUTURE WORK 64
APPENDICES
A. WAVELENGTH ESTIMATION FROM PASSIVE SCALARS 66
B. SCRIPTS FOR IMAGE ANALYSIS 71
C. UNCERTAINTY QUNATIFICATION 92
BIBLIOGRAPHY 97
VITA. 104

LIST OF ILLUSTRATIONS

Figure Page

Figure 1.1 Evolution along a plane of an RTI driven mixing layer for a miscible liquid combination taken from a three dimensional DNS[44] at an A_t of 7.5×10^{-4} , *Sc* of 7 and a grid resolution of $1152 \times 760 \times 1280$ (x,y,z), sing initial conditions measured from the water channel [45].....6

Figure 2.1 Pictorial representation of the experimental facility. 15

Figure 2.2 Pictures of the experimental facility. 16

Figure 2.3 Schematic of the barrier withdrawal concept.....17

Figure 2.4 Schematic of the experimental set-up (Green filter is used only in the reactive scalar experiments). 18

Figure 2.5 Pictures of the light source and the camera.....20

Figure 3.1 Nigrosine calibration curve (σ has uncertainty bounds of $\pm$ 1.5%). 25

Figure 3.2 Phenolphthalein calibration curve (σ has uncertainty bounds of $\pm$ 1.23%).....26

Figure 4.1 Evolution of the RTI driven mixing layer with passive scalar (A_t=7.5 $\times 10^{-4}$). 31

Figure 4.2 Evolution of the heavy fluid volume fraction at various non at τ ranging from 0.25 to 2 at an interval of 0.25. 33

Figure 4.3 Growth of the bubble height based on 5%-95% fiducials as a function of (a)$A_t g t^2$- the most dominant length scaling and (b) τ 34

Figure 4.4 Evolution of integral mix width 36

Figure 4.5 Evolution of self-similarity parameter calculated using Ristorcelli & Clark definitions based on bubble height and integral mix-width. 37

Figure 4.6 (a)Schematic of the computational domain showing with the heavy fluid on the top(red) the light fluid at the bottom (blue) and a perturbed interface; (b) and (c) show initial perturbations for simulating water channel and the current experiment, respectively.....40

Figure 4.7 (a) and (b) depict the spectrum of initial conditions that were modeled from the current experiment and the water-channel[77], respectively.....41

Figure 4.8 (a) and (b) depict the contours of density perturbations at z = 0 plane that were modeled from the current experiment and the water-channel[77] , respectively.....42

Figure 4.9 Comparison of α_b values obtained from simulations and experiment. 43

Figure 4.10 Evolution of RTI driven mixing layer with reactive scalar (A_t=7.5 $\times 10^{-4}$) ...45

Figure 4.11 Evolution of planar averaged concentration profiles for τ ranging from 0.25 to 2 at an interval of 0.25 for different pH combinations (pH_1=11.5 in all the cases).....47

Figure 4.12 Comparison of planar averaged concentration profiles for τ ranging from 0.25 to 2 at an interval of 0.25 for different pH combinations (pH_1=11.5 in all the cases) between the current experiment and the water channel facility[9]. 50

Figure 4.13 Comparison of equivalent product thickness evolution between current investigation and the water channel (pH_1= 11.5 and pH_2= 7). 52

Figure 4.14 Comparison of evolution of molecular mixing parameter from the current investigation (a) and the water channel (b). 52

Figure 4.15 Comparison of evolution of volume fraction variance from the current investigation (a) and the water channel (b).. 52

Figure 4.16 Evolution of global mixing parameter as a function of τ along with values reported by previous investigations. 58

Figure 4.17 Evolution of global mixing parameter as a function of Re_h along with values reported by previous investigations.....60

Figure 5.1 Pictorial representation of the methodology for controlled variations.....65

LIST OF TABLES

Table Page

Table 2.1 Listing of parameters in the experimental set-up for different configurations 19

Table 3.1 Summary of uncertainty bounds for measured quantities. 27

Table 4.1 Summary of experiments performed. 29

1. INTRODUCTION

1.1. OVERVIEW AND MOTIVATION

The study of unstably stratified fluids has long been pursued in the interests of understanding and quantifying the phenomenological physics associated with turbulence. Instability driven flows in this category evolve much faster into the chaotic regime and are instrumental in development of predictive models for turbulence. Special cases of such instabilities are the Kelvin-Helmholtz (shear driven)[1-2] instability and the Rayleigh-Taylor (buoyancy driven) instability[3-4]. The Kelvin – Helmholtz instability (KHI) in its most general form arises when the different layers of a stratified heterogeneous fluid are in relative motion. Turbulence induced by KHI has received extensive experimental and numerical attention in a configuration where in there are two participating pure fluids which are superimposed with a relative velocity [5-6]. Instabilities derived from the nature of equilibrium of incompressible fluids of variable density outline the class of buoyancy driven flows. Rayleigh-Taylor instability (RTI) pertains to a specific configuration of buoyancy driven flows where in two participating heterogeneous fluids of different density are accelerated towards one another. Quantifying turbulence in RTI driven flows is by large unexplored as the flow evolution is characterized by coupling of the density and the velocity fields, requiring a complete detail of molecular mixing for accurate modeling of the phenomenon[6].

The extent to which Direct Numerical Simulations (DNS) can be used for exploring RTI driven flows is severely constricted by the resolution requirements for resolving all the involved scales to obtain the mixing detail. The smallest scale to be resolved in case of gas phase flows (Schmidt number (Sc) ~ 1) are dictated by the smallest velocity scales (Kolmogorov scales - λ_K)[7]. In liquid phase, where in the Schmidt number is > 1 and generally varies between 600-3000, momentum diffusion dominates scalar diffusion and the scalar scales contribute to turbulent diffusion and so the smallest scales to be resolved are governed by the smallest scalar field scales (Batchelor scales - λ_B)[8] given by:

$$\lambda_B \propto \lambda_K Sc^{-1/2} \propto \mathrm{Re}^{-3/4} Sc^{-1/2}; \lambda_K \equiv \left(\frac{\nu^3}{\varepsilon}\right)^{1/4} \propto \mathrm{Re}^{-3/4} \tag{1.1}$$

where in ν is the kinematic viscosity of the fluid, ε is the average kinetic energy dissipation rate and Re is the flow Reynolds number. With increasing Schmidt numbers domain resolutions required for resolving the flow in 3 dimensions scales as λ_B^3 in space and as λ_B in time. Therefore, the associated computational cost involved with Direct numerical investigations of High Schmidt number turbulent mixing layer scales as $1/\lambda_B^4$ which translates to a Re^3Sc^2 scaling(from 1.1) [6] and is unviable with the current computational means to several generation of computational power[9]. Large Eddy Simulations (LES) have been instrumental in determining the flow metrics with fairs accuracy when the internal structure represented by the sub-grid scale(SGS) model was dictated by the velocity scales rather than scalar scales[10-11]. Development of SGS for high Sc flows is still an open area of research and requires a complete understanding of the role of Schmidt number on the internal structure especially with fluid entrainment occurring at the largest scales of the flow[12]. The result of energy cascade from the small scales to the large scales poses high resolution requirements throughout the evolution to capture the flow physics accurately and is therefore computationally taxing. RTI driven flows are marked by inherent inhomogeneity and anisotropy due to the associated characteristics such as memory of initial conditions, preset directionality of the force field, material discontinuities and baroclinic vorticity[13] thereby rendering the modeling of the flow very challenging. Traditional turbulence models that could very well characterize the turbulence associated with passive scalar mixing using scaling arguments on the first order statistics of the flow cannot characterize RTI driven flows due to the above set complexities that violate the pivotal assumptions on which the modeling was based. Early efforts in modeling this specific class of flows have led to independent theories based on large scale observations which were often limited in their accuracy to a specific phase of evolution of the instability and even so their universality was constrained to specifics of the flow conditions from where the observations were derived. Further developments using two fluid models have shown a reasonable agreement with experiments[14] but their universality is debated due to the simplifying ansatz applied within. A complete understanding of the flow characteristics is therefore a pressing need for the development and calibration of accurate predictive models wherein the inherent flow physics would be depicted without the environment specific bias.

Apart from the intrinsic theoretical interest of investigating variable density flows, motivation for studying RTI in its phenomenological form is derived as it manifests in a wide range of spatial and temporal scales across various natural and artificial processes. On the astrophysical scales RTI driven mixing limits heavy element formation in stellar implosions (Supernovae) [15-16]. At the geographical scales RTI influences atmospheric and oceanographic currents due to temperature or concentration gradients [17-18]. At smaller scales fuel droplet breakup in IC engines has been attributed to RTI due to the unstable interface formed between the air-fuel interface and the resulting acceleration due to the local air movement[19]. At the smallest scales RTI has been observed in the implosion phase of an inertial confinement fusion capsule where in the cold shell material induced into the high temperature core results in fuel contamination during the implosion of an inertial confinement fusion capsule thereby decreasing the overall thermonuclear yield per capsule [20-22] and thus lays out the impetus for probing the area in the interests of developing predictive models. Development of turbulence models encompassing such a wide range of spatio-temporal scales are challenging, especially when the mixing process needs to be modeled to accurately predict the flow phenomenon.

1.2. THE RAYLEIGH-TAYLOR INSTABILITY

RTI arises from interfacial perturbations between two fluids of different densities ($\rho_1, \rho_2; \rho_1 > \rho_2$) that are unstably stratified such that the pressure (*p*) accelerates the heavy fluid towards the light fluid [3-4], mathematically given by $\nabla p.\nabla \rho < 0$. The current investigation is a realization of the RTI driven flow where in the pressure field is generated by the earth's gravitational field. The generation of baroclinic vorticity resulting from misalignment of the density and the pressure gradients, stretches the interfacial perturbations in general and in miscible, fluids mixes them, and the flow evolves unbounded. This is evident from the inviscid variable density vorticity equation given below:

$$\frac{D\omega}{Dt} - (\omega.\nabla)u = -\frac{1}{\rho^2}\nabla\rho \times \nabla p \tag{1.2}$$

The vorticity generated by the instability is initially concentrated at the interface between the two fluids, but in miscible fluids undergoing molecular mixing, the region over which there are large density gradients enlarges with time, and so too does the region generating vorticity. Rayleigh-Taylor instability is one of the purest fluid systems in which molecular mixing can be initiated, since the instability exists independently of boundary conditions. Despite its apparent geometric simplicity, a horizontal density interface in free space gives rise to some of the most complex, important and least well-understood phenomena in classical mechanics. Once vorticity has been generated baroclinically, it non-linearly advects according to equation 1.2, progressively increasing its spatial complexity and leading to turbulence. The onset of instability is insensitive to the spectral content of the perturbation at the interface [23] and the configuration is implicitly unstable, however independent numerical investigations have reported that the evolution of the low- and high-order statistics characterizing the growth of the mixing layer, at a given Atwood number A_t, given by:

$$\mathrm{A}_t = \frac{\rho_1 - \rho_2}{\rho_1 + \rho_2} \tag{1.3}$$

are sensitive to and strongly influenced by the spatial structure of the initial perturbations [24-31]. In general, the initial growth of an RT unstable interface, when the amplitudes of the perturbations are much smaller than the wavelength ($a < 0.1\lambda$), is exponential as predicted by linear instability theory [23, 32]. During this phase the modes grow independently until the effects of viscosity result in the emergence of the most unstable wavelength given by:

$$\lambda_m \approx 4\pi\left(\frac{\nu^2}{gA_t}\right) \tag{1.4}$$

[33] where g is the net acceleration at the interface and ν is the averaged kinematic viscosity defined as:

$$\nu = \frac{\mu_1 + \mu_2}{\rho_1 + \rho_2} \tag{1.5}$$

where, μ is the dynamic viscosity of the corresponding fluid indicated by the suffix. The growth rates deviate from the exponential behavior and the predictions from linear

stability theory when the amplitudes of the perturbations are comparable to their wavelength [33-34]. During this phase, marked by non-linear mode coupling, slower growth rates are observed accompanied by emergence of dominant interpenetrating structures of the light (bubble) and heavy fluids (spikes). Following the onset of non-linearity, secondary Kelvin-Helmholtz instabilities develop as regions of high vorticity form between rising bubbles and falling spikes. As the instabilities grow, an increase in the range of scales present in the mixing layer is driven by the nonlinear interactions between buoyant structures. Bubbles and spikes merge to form larger buoyant structures, while shearing forces generate smaller-scale structures, as well as more topologically-complex interfaces. The growth rate of bubbles and spikes is essentially the same at low A_t, while this symmetry is skewed at higher A_t with the spikes advancing significantly faster. During these initial phases of evolution, the growth of the mixing layer is dominated by longer wavelengths as they have a larger terminal bubble velocity given by[35] :

$$\frac{dh_b}{dt} \propto \sqrt{\lambda_b} \tag{1.6}$$

The flow evolves through the dynamics of the non-linear growth phase until the dominant wavelength, $\lambda_d \sim 10\lambda_m$ [33]. The flow then takes a final transition to a regime of self-similar turbulent mixing where in the most significant length scales - the mix-widths can only be scaled as a function of gt^2, and the growth rates at a constant acceleration are defined by:

$$h_i = \alpha_i A_t g t^2 \tag{1.7}$$

where the subscript i refers to the bubbles "b" or the spikes "s" and α is a dimensionless, self similar growth constant. The above scaling argument has been established by extensions to classical linear stability theory [33], dimensional analysis [26, 36], self-similarity analysis [29], bubble merger and competition models[30, 37-38], experiments [24, 39-42] and numerical simulations [16, 30, 43]. At low A_t, $h_b \approx h_s$ and $\alpha_b \approx \alpha_s = \alpha$. Figure 1.1 shows a representation of various phases of evolution described above taken from a DNS[44].

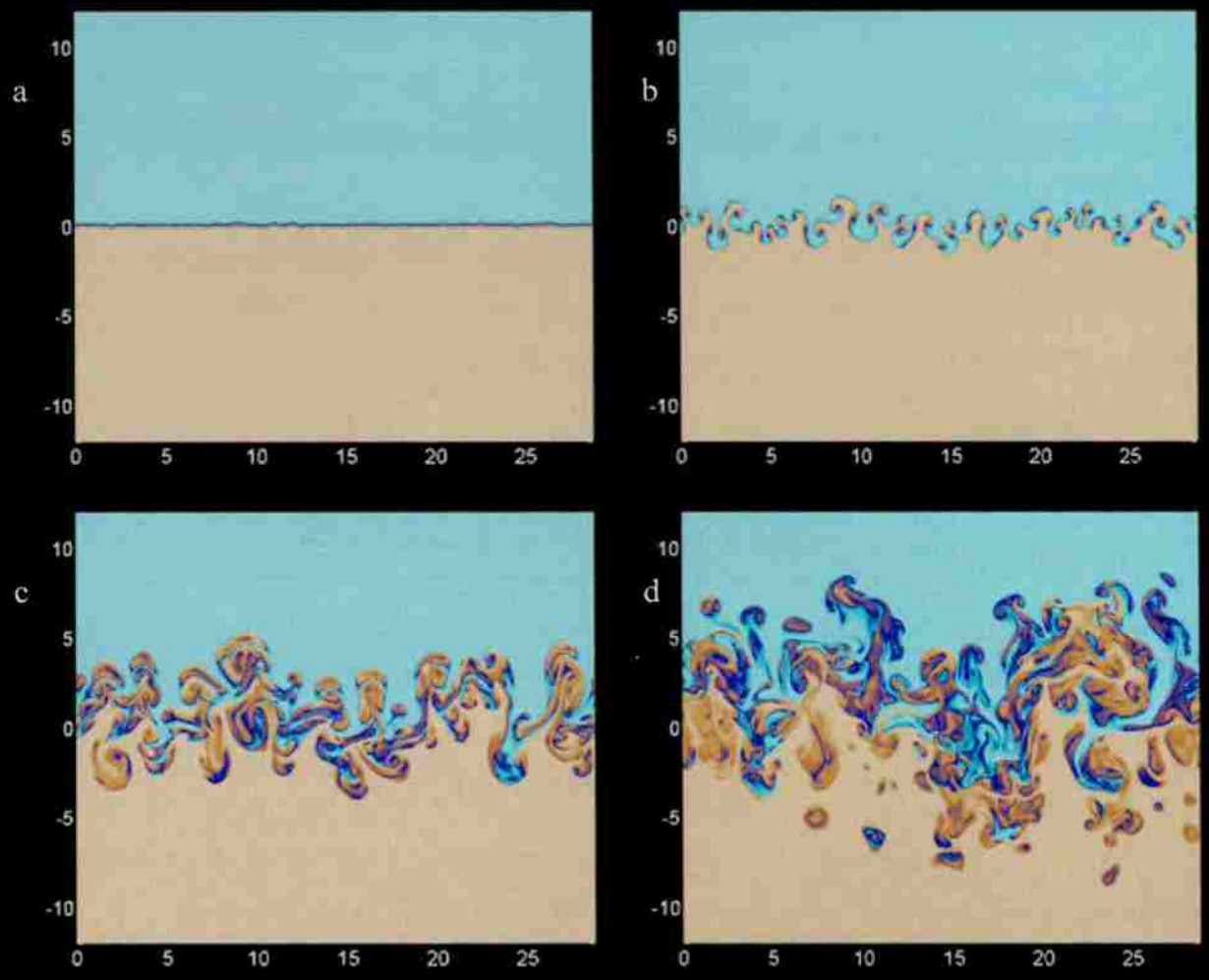

Figure 1.1 Evolution along a plane of an RTI driven mixing layer for a miscible liquid combination taken from a three dimensional DNS[44] at an A_t of 7.5×10^{-4} , *Sc* of 7 and a grid resolution of $1152 \times 760 \times 1280$ (x,y,z), using initial conditions measured from the water channel [45].

In sequence, the figure represents an initial perturbed RT unstable interface (at time - $t = 0$ s), initial exponential growth of modes ($t = 2.82$ s), the non-linear mode coupling phase ($t = 7.62$ s) and the final self similar regime ($t = 10.53$ s) of the miscible, binary fluid system with the color scaling representative of the volume fraction of the fluids. As it can be noted, an increased amount of mixing of the constituent fluids can be seen in the turbulent regime setting the importance of molecular mixing as a governing parameter in characterizing the flow dynamics. Despite the importance of the coupled dynamics involved with molecular mixing and their direct relation to aiding several

practical problems, the comprehension of the question is very limited due to the very few molecular mixing measurements that are available.

The current work targets at quantifying molecular mixing during the evolution of a transient, high Schmidt number, RTI driven mixing layer. The transition from the non-linear growth phase to self-similar evolution was defined by two limiting theories namely the bubble merger theory- involving non-linear coupling of two or more bubbles to form larger structures and the bubble competition theory-where in the transition occurs by saturation of modes present in the initial perturbations. The first theory postulates the process of nonlinear coupling of saturated modes and resulting in a universal α_b [46-47] while the second process retains a memory of the initial conditions. For a long time the stark dissimilarity in the value of α_b obtained from experimental investigations and numerical simulations has been attributed to numerical diffusion until recent work has indicated a strong correlation to the dependence of α_b on low-wave number loading of the initial perturbation spectrum [26-27, 29, 48]. Subsequent work published on quantifying the extent of the influence of the bubble merger and bubble competition theories [28, 30] have proposed that a universal value of α_b is attained only when the transition is purely achieved by the mode-coupling mechanism as put forth by bubble merger theory and that this can be fully realized by inducing only short wavelength perturbations. Real time scenarios and experiments cannot be free from long wavelength disturbances and so the theory offers a possible explanation by underlining the existence of a definite correlation between the growth parameters and the initial conditions. However there is no explanation as to how the isolated effect of dynamics explained by each theory can be coupled in a realistic scenario when both the transition mechanisms interoperate and this severely curtails development of mix-models based on the knowledge of the limiting mechanisms individually.

1.3. PREVIOUS WORK

Prior efforts in characterizing turbulent flows from experimental measurements have been focused on shear-driven flows such as jets and shear layers where in KHI is the fundamental form of instability that was driving the transition to turbulence. Data

pertaining to statistical measurements of turbulence from buoyancy driven flows and in specific RTI driven flows is limited due to factors such as difficulty associated with setting up such experiments and establishing high fidelity diagnostics.

Lord Rayleigh's initial attempts at observing the instability experimentally [3] used warm salty dyed water supported by a porous membrane above cold fresh water. Thermal diffusion of heat to the atmosphere then allowed the upper layer to become cool, and reach parity of buoyancy with the lower layer. Under further cooling, the upper layer started to migrate into the lower layer in thin vertical finger like strands. Rayleigh believed he was observing the baroclinically driven process we know today as Rayleigh-Taylor instability. However, he had inadvertently discovered a diffusion driven process known as viscous fingering[49]. However the observations were qualitative in nature and accounted for phenomenological detail. Baroclinic vorticity was completely and repeatedly observed in the experimental work by Lewis [50] and Emmons et al.[51] following Taylors analytical study[4]. Subsequent interest into the problem was driven by the technological imperative pressing insight into the phenomenon. Experimental study conducted on the Rocket Rig experiment[52] which used the rocket propulsion to reverse the acceleration on a configuration stable at gravity established flow behavior establishing (1.8) and the quest for obtaining the value of $\alpha_{b,s}$ began. Subsequent investigations involving experiments designed on the Rocket-Rig principle of inverting gravity over stable configurations were the Gas-gun experiment [53] which employs compressed gases for generating the requisite acceleration and the Linear-electric motor[54] which leveraging the principle of reactive force produced by electro-magnetic induction in coil over a vertical armature for the thrust. These experiments reported $\alpha_{b,s}$ at large acceleration for a range of A_t using both miscible and immiscible fluids. All these investigations accounted for the largest scales of flow and power laws governing the growth at late time. The inherent complexity associated with the experiments and the diagnostics of the age inhibited the investigations from adopting techniques necessary to account for higher order turbulence statistics or sampling initial conditions. Most of the numerical work that was performed in conjunction with these experiments so as to establish models was seeded with random perturbations judged by visual inspection and resulted in large discrepancies in the results.

The simplest experimental designs that had the cleanest realizable form of the RT unstable configurations at the earth's gravity were the sliding barrier experiment at University of Cambridge[25, 55], the Water channel[56] and Gas-channel[57] experiments at Texas A&M. The set-up at Cambridge involves an initially unstable configuration of fluids separated by a barrier which is removed manually to study the evolution. Though the Cambridge experiment established that the underlying assumptions on the nature of turbulence to be modeled as given by (1.8) are valid, the experiment could not deliver values of $\alpha_{b,s}$ with a high degree of statistical confidence[25] due to the degree of manual intervention and the transient nature of the experiment. The Texas A&M experiments have velocity matched streams of different fluids evolving spatially into steady state RTI driven mixing layer and so provide for very precise measurements. The static nature of these experiments simplified the complications associated with setting up high fidelity diagnostics (in comparison to moving reference frames) for the measurement of fluctuating quantities and initial conditions. Numerical investigations seeded with initial conditions as measured and modeled from experiments were performed on the sliding barrier experiment [25] and the water channel experiment [45, 58]. There was a far greater agreement between numerics and experiments in these investigations with regard to the evolution of macroscopic and microscopic quantities. These recent investigations have led to the appreciation of the significance of the initial condition spectrum in the subsequent growth of the instability. This also offers a possible explanation to the wide spread in the value of $\alpha_{b,s}$ reported from different experimental designs. The turbulence models developed on these investigations relate accurately to flow scenario under the influence of the initial conditions they were calibrated against but do not provide an explanation or an accounting for the initial condition and *Sc* dependency [13]. Moreover initial condition and *Sc* dependency of microscopic quantities that relate to internal structure and molecular mixing could not be related between DNS and the experiments due to constraints on computational expense posed by the high *Sc* of experiments and the question of their sensitivity has been an issue of debate [25-26, 58-60]. It is necessary to ascertain data pertaining to the role of varying initial conditions and *Sc* at different A_t on the evolution of molecular mixing parameter

(θ) so as to relate to the questions above and in developing a frame work that would fit in the effect of Sc and initial conditions into turbulence models.

Molecular mixing in classical, shear-driven mixing was monitored and quantified in variety of experiments. In contrast, experimental investigation of buoyancy-driven flows and RTI driven flow in specific are limited due to factors such as the difficulty in establishing the experiment and the diagnostics. Initial experiments reporting molecular mixing in gas phase shear layer at $Sc \sim 7$ were designed by Konard[61]. Breidenthal[62] reported molecular mixing in liquid phase turbulent shear layers operating at a $Sc \sim 1000$. Both the measurements employed backlit optical techniques to quantify the degree of molecular mixing by measuring the amount of light absorbed by a specific chemical species. Equivalent product thickness given by P/δ, where P is the equivalent thickness of chemical product across the mixing layer and δ is the mix-width (Vorticity thickness in shear driven flows) of the turbulent shear layer, was the prime metric of their investigation. The technique involved the usage of a diffusion limited chemical reaction and so the amount of product formed was representative of the amount of molecular mixing of the participating fluids. It has been observed that as the flow crossed the transition Re, turbulent fluctuations stretched the interfacial surface area between the participating fluids resulting in enhanced mixing of the fluids and an increased formation of products at a rate that was much greater than the amount of pure fluid that was entrained into the mixing layer. Furthermore, these observations were found to be invariant with the initial conditions of the flow or the velocity ratio, but strongly dependent on the Schmidt number of the participating fluids. This work was extended by Koochesfahani and Dimotakis[63] where in a combination of scalar and reactive flow techniques were used to quantify the mixing in the post transition region of the mixing layer. Similar reactive flow techniques were employed for the study of mixing in turbulent jets by Shea [64] to study the effects of equivalence ratio and Reynolds number in effect to reduce initial fuel consumption. Zhang et al.[65] employed the same technique and reported that enhanced mixing was observed by modifying the geometry of the jet exit. Few measurements made in RTI driven flows in this direction have been reported in the Water channel where point wise measurements of θ across the mixing layer have been provided using a high resolution thermocouple at $Sc \sim 7$[45] and

complete evolution of the span wise integrated θ was reported using chemical reactions[9] at a $Sc \sim 1000$. Point wise measurements of θ using hot wires were reported from gas channel measurements for a range of A_t [66]. Concentration estimates at a single equivalence ratio and point wise measurements of mixing using conductivity probes were reported from draw plate experiment[24]. Efforts in the direction of controlled initial conditions have been reported by the Magnetic immobilization facility[67] which employs magnetorheological fluids and control of initial conditions is achieved by using magnetic fields; and the drop-tank facility which is similar in principle to the Linear Electric motor where in controlled initial conditions are achieved by using a shaker motor leveraging on the principle of Faraday waves[68].

Even though experimental studies of buoyancy driven flows yield quantitative measures of θ, there is a limited amount of data and it is very difficult to apply high fidelity diagnostics to the flow. Recent increase in computational power has led to an increased number of numerical investigations of the RTI driven instability. Similar to simulations of shear driven turbulent layers, buoyancy driven instabilities require a large domain so as to observe growth without interference from the boundaries. With increasing computational power numerical investigations till date have progressively focused on larger spatial and temporal evolution over each generation and have been successful in resolving the flow to a good detail at high Re_h pertinent to the turbulent regime. However all the investigations have operated at a low Sc (< 7) due to limitations in the computational power posed by the Batchelor scales which is not likely to be viable for several generations of computational capability. The first major numerical work that resolved the turbulent regime and predicted quadratic growth rate was performed by Youngs[33] working in parallel to Read's[52] work. Molecular mixing has been reported by a number of DNS. Subsequent DNS conducted by Ristorcelli and Clark [29] who reported θ in $Sc = 1$ RTI driven mixing layer with different initial conditions. Cook and Cabot[16] reported mixing at a high Re and reported global mixing parameters in a Sc=1 mixing layer. Livescu and Ristorcelli[69] performed DNS to examine homogenous, variable-density turbulent mixing which was intended to mimic the internal turbulent core of an RTI driven mixing layer. However the study was limited to $Sc < 2$ due to computational constraints. In an effort to develop a higher order mix model for RTI

driven flows, Mueschke and Schilling [58] performed DNS at a Sc of 7 using initial conditions measured from the water channel experiment and were combined with the data from the same. In an attempt to answer the persistent deviation of α measured from experiment and even between different numerical investigations, the 'Alpha group'[70] performed a series of simulations that which simulated a series of simple well-defined test problems aimed at definitively establishing a universal $\alpha_{b,s}$. On these test cases, with few exceptions, the computer codes predict similar growth rates, and this confirmed that in general the spread of values was not caused by algorithmic variation. In the direction of increasing the computational efficiency and to relax small scale requirements and to increase the Re the flow could evolve to, implicit large eddy simulations(ILES) and monotonic implicit large eddy simulations(MILES) were widely adopted in numerical studies of RTI driven mixing[11, 24-25, 28, 30]. Both the methods conform to the class of LES but do not include any sub-grid scale models (SGS) but rather allow numerical diffusion which operates analogous to physical diffusion in dampening the small scales (of both scalar and velocity) and operate at a $Sc \sim 1$. Simulations based on MILES and ILES were used to predict θ till late time when the flow evolved to a high Re and showed good conformance among all the LES schemes that were employed, they are restricted to a Sc of 1 without proper sub-grid scale modeling.

1.4. CURRENT WORK

The current work is an experimental investigation of the effects of initial conditions on molecular mixing in a miscible, low-A_t, turbulent, high-Sc, RTI driven mixing layer. As part of the current work an experimental facility for producing an unstable density stratification and observing the evolution of an RTI driven mixing layer were designed. The design and working principle of the experiment are similar in configuration to the facility at University of Cambridge [25]. The quintessential signature of the experiment is a static tank holding unstably stratified fluids initially separated by a solid barrier, the removal of which allows the study of a transient, RTI driven mixing layer evolving from an imposed initial perturbation issued in the wake of the barrier removal. The dimensions chosen in the design of the facility allow for capturing the

evolution of the instability till a non-dimensional time of $\tau = 2$ which corresponds to an actual time of 18 seconds, where τ is given by:

$$\tau = t\sqrt{\frac{A_t g}{H}} \tag{1.8}$$

where H is the height of the domain and t is time and a buoyancy Reynolds number (Re_h) of ~ 10000, where Re_h is based on the definition provided in [71] as:

$$\mathrm{Re}_h = 0.35\sqrt{Agh^3}/\nu \tag{1.9}$$

where is h is the total width of the mixing layer. A detailed description of all the elements of the experimental set-up will be discussed in section 2. Well calibrated, non-intrusive, optical diagnostics are employed to measure the mixing layer evolution using a passive scalar (Nigrosine) and a reactive scalar (Phenolphthalein), independently. Following the methodology developed at the Texas A&M water channel facility, the measurements of volume fraction from the passive scalar experiments are coupled with the chemical product formation estimates from a diffusion limited chemical reaction [9, 56, 62-63] using the reactive scalar, to accurately quantify the degree of molecular mixing in the mixing layer. The details of the diagnostics, their calibration and the uncertainty in the measurements are detailed in section 3. The results section focuses on examining the variations of important macroscopic parameters (such as α_b) and microscopic parameters (such as molecular mixing parameter-θ) in a turbulent RTI driven mixing layer at an $A_t = 7.5 \times 10^{-4}$ and a $Sc \sim 1000$ for different initial conditions with particular emphasis on the microscopic parameters. The results from the passive scalar are used to model the initial density perturbation spectrum and are validated using an implicit large eddy simulation. An in house CFD code RTI-3D[72] is used to this end. Comparisons are then drawn between molecular mixing metrics from water channel in view of the variations in the initial conditions between both the experiments. Temporal evolution of volume fraction estimates, h_b, α_b, integral mix width (W_b) are presented from the passive scalar concentration measurements. Variation in normalized concentration profiles at various equivalence ratios is discussed for the reactive scalar runs. The spatio-temporal evolution of θ and volume fraction variance of the heavy fluid ($\overline{f_1'^2}$) derived using the data from passive and reactive scalar runs, Equivalent product thickness (*P/h)* and global mixing

parameter (Θ) variations are studied in comparison with the results from the water channel facility so as to explore the extent of influence of initial conditions on the metrics of molecular mixing.

2. EXPERIMENTAL SET-UP

The experimental facility comprises of a static tank made of 0.5 inch thick Lexan sheets (PALRAM Industries Ltd.). The shape of the test section is essentially a cuboid with a square cross section. The inner dimensions of the tank measure 305 mm in length and width, and 635 mm in height. The heavy fluid and the light fluid that are placed in the tank in the unstable configuration are initially separated by a rigid stainless steel barrier. The instability is set in as the barrier is progressively withdrawn from a slot machined on one of the end walls. The other end wall and the side walls are grooved to support portions of the barrier to help insertion and withdrawal. The design and principle of the experimental set is similar to the facility pioneered by Dalziel et al. [25] at University of Cambridge. Figure 2.1 shows a pictorial representation of the tank assembly with the flat plate barrier.

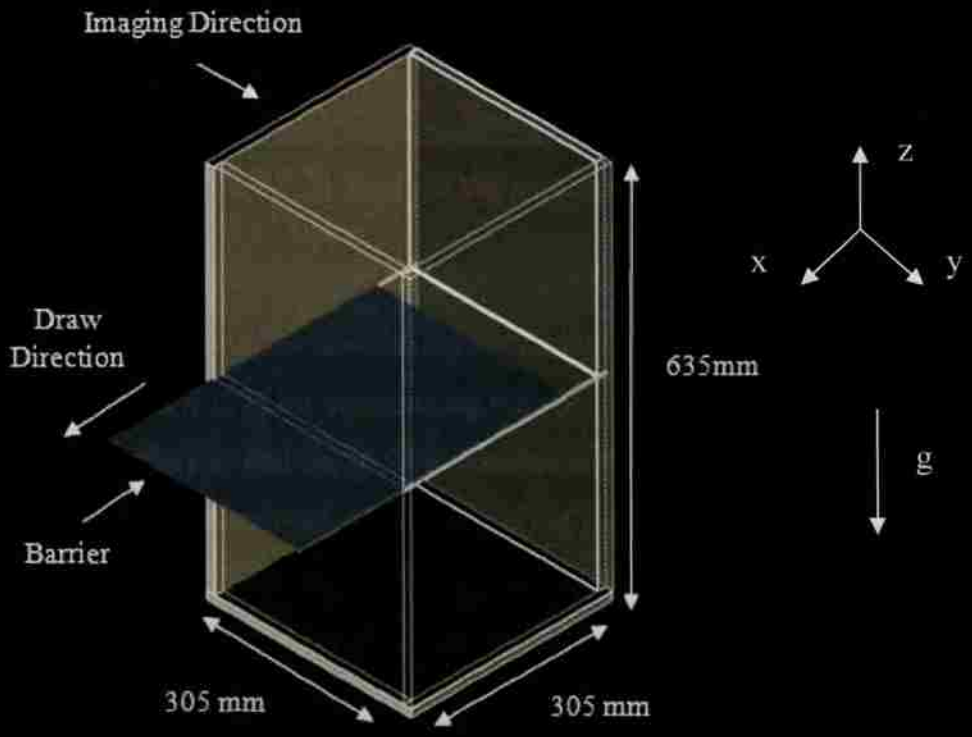

Figure 2.1 Pictorial representation of the experimental facility.

Imaging of the mixing layer is performed through the viewing sides which are as marked in the above schematic. One of the most important requirements for the viewing sides is for the surfaces to be clear and devoid of scratches or particulate depositions. Scratch resistance is one of the attributes behind the choice of Lexan as the construction material for the test section apart from strength, toughness and superior optical properties. Figure 2.2 shows pictures of the test section

Figure 2.2 Pictures of the experimental facility.

The facility incorporates into the barrier design, an implementation of the idea conceived by Lane-Serff [73] for minimizing the shear layers arising from relative motion between the barrier and the fluid in contact with its surfaces. The design requires that the barriers are hollow extrudes (tube forms) of the respective 2-D shape forms running along the length of the tank and extending outward in excess by about 102 mm. Two strips of Nylon fabric, one running over the top surface and the other over the bottom surface of the barrier cover 85% of the barrier width all along the portion inside the tank at any instant of the barrier withdrawal. One end of each fabric piece is fastened to the tank, and the other free end is used to pull. The Nylon strips running on the outer surface of the barrier wrap through the inside of the barrier at one end and run out from

the opening at the front end of the barrier. The barrier is withdrawn by pulling the fabric and simultaneously pushing the barrier so as to maintain a tension in the fabric. Figure 2.3 presents a schematic of the barrier withdrawal concept explained above. This way the portion of the fluid at the inner edge perceives the motion of the barrier while the rest of the fluid in contact with the barrier surfaces remains stationary, thereby minimizing the effects of the ensuing shear layer.

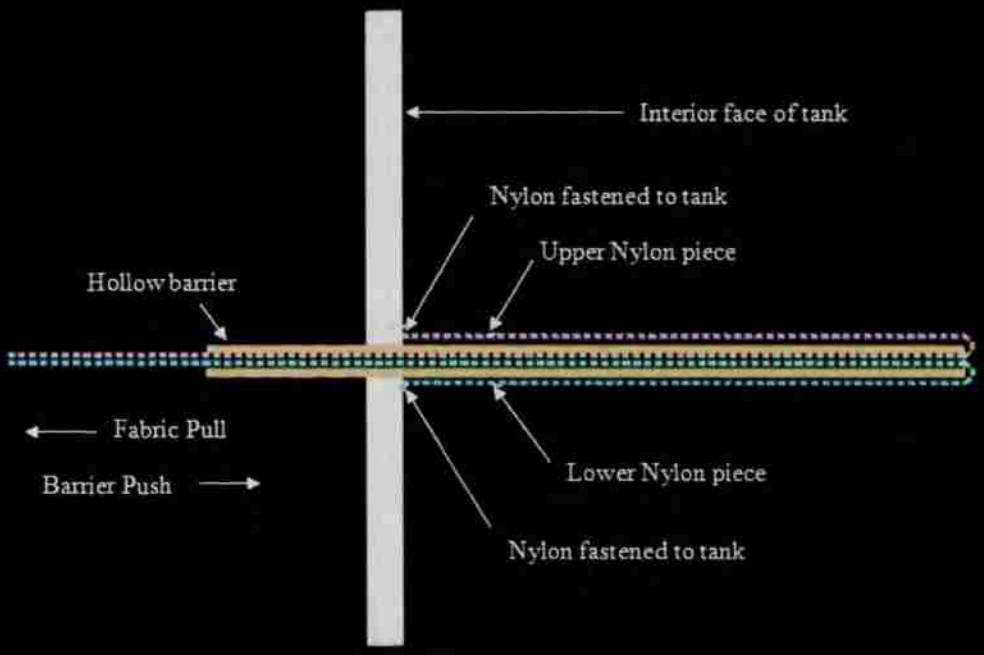

Figure 2.3 Schematic of the barrier withdrawal concept.

Even so, the combined effect of liquid from the top of the tank moving through the finite void due to barrier removal, the shear action between the fluid and the barrier at the tip and the uncovered regions of the plate pose a significant disturbance at the interface. One of the key requirements for the experiment is the complete withdrawal of the barrier from the interior of the test section. This requires that the barrier to be brought to halt within 0.25 inches of after completely leaving the domain as it still needs to cover the opening in slot from where it is retracted. To help this two L – shaped guides are used in the inverted configuration which supports the barrier as it is pulled out. The guides are

aided by configurable stops in order to precisely halt the barrier within a given tolerance after exiting the interior of the test section. This arrangement can be seen from the pictures in Figure 2.2

By design, the experiment ensues a transient RTI driven mixing layer upon removing the barrier. The dimensions of the test section allow for examining the mixing layer till a non-dimensional time of τ =2, corresponding to an actual time of 18 seconds and a Re_h ~10000. De-ionized water procured from the campus power plant is stored in separate 25 gallon tanks (Den Hartog Industries Inc) and exposed to the laboratory ambient for a period of 8 hours so as to reach thermal equilibrium is used as the base fluid for conducting the experiment. The density difference between the liquids is brought about by adding Sodium chloride to the water in one of the tanks. Gravimetric measurements of 50 ml samples of the solutions are taken using electronic scales and densities are adjusted to the required A_t. The current investigation is limited to a small $A_t = 7.5 \times 10^{-4}$ as refractive index effects become prominent at larger A_t [74]. Figure 2.4 presents a schematic of the experimental configuration for the passive scalar and the reactive scalar configurations and Table 2.1 lists values for parameters a,b,c and d (control distances) depicted in the figure for the set-up of experiment in different configurations.

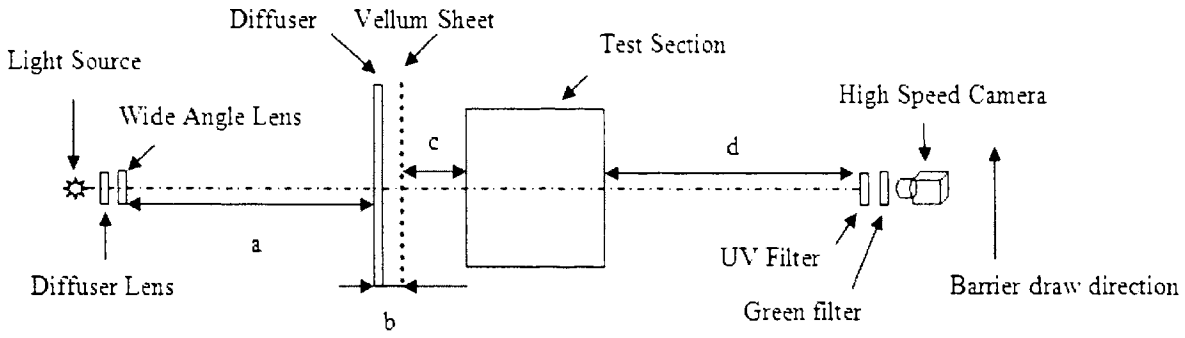

Figure 2.4 Schematic of the experimental set-up (Green filter is used only in the reactive scalar experiments).

Table 2.1. Listing of parameters in the experimental set-up for different configurations.

Variable	**Value for Passive scalar setup (cm)**	**Value for Reactive scalar setup (cm)**
a	394	204
b	4.2	4.2
c	26	22
d	195	195

The test section is illuminated from the side using a 200W Metal Halide arc lamp housed and stabilized in ARRILUX 200 POCKETPAR system (ARRI). The lamp head is used in a full flood configuration along with a frosted diffuser lens and a beam widening lens mounted on an inbuilt lens holder. A fluorescent light cover and a sheet of vellum paper are placed behind the test section to produce a uniform intensity back ground for backlit imaging. PHOTRON 1024 PCI, a CMOS based high speed camera operating at a 512 x 1024 pixel resolution, 60 frames per second and 1/60 sec shutter speed is used for recording 8-bit black and white images as the experiment progresses. The images are then corrected for variations in the background intensity and analyzed using MATLAB scripts. All the necessary coding for extracting and processing pertinent information from the image analysis is provided in Appendix-B. Pictures of the light source and the camera involved are shown in Figure 2.5.

Figure 2.5 Pictures of the light source and the camera.

Concentration measurements of Nigrosine dye (Sigma Aldrich) and Phenolphthalein indicator (Sigma Aldrich, derived from intensity readings, directly relate to the span averaged values of volume fraction of the heavy fluid and the quantity of the mixed fluid (at a given ratio), respectively. Nigrosine absorbs most of the visible spectrum and its emissions are limited to upper blue region[75], so in conjunction with passive scalar experiments the camera was used along with a UV filter. Phenolphthalein, on the other hand selectively absorbs green light (552 nm wavelength)[75], so the physical presence of the indicator tracing the mixture ratio is marked by pink color. For the light source and camera combination used here the CMOS was saturated by the energy from rest of the spectral content as it was rich in energy across all the wavelengths in the visible spectrum as compared to a conventional light source and could not detect phenolphthalein. A band pass optical filter operating at 550±10 nm (Edmund Optics) was used to measure green light absorptions for the reacting flow experiments. Figure 2.6 shows the spectral signature of the current light source as given by the manufacturer of the Lamp (GE®).

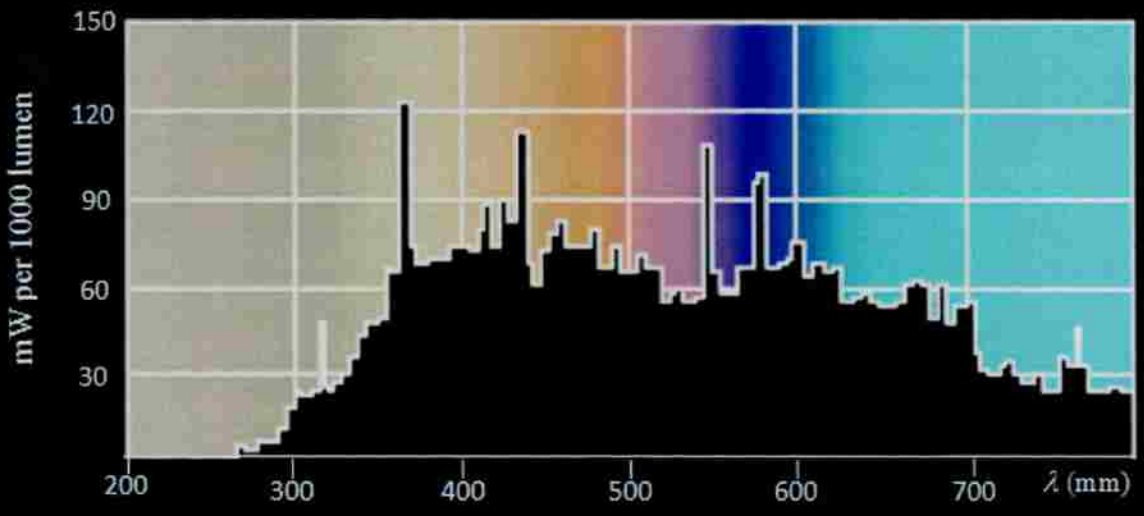

Figure 2.6 Spectral signature of the light source used in the present investigation.

3. DIAGNOSTICS AND UNCERTAINITY IN MEASUREMENTS

The current investigation uses optical diagnostics via backlit imaging techniques to measure and quantify the metrics reported. The usage of optical diagnostic renders the measurement process non-intrusive and free of probe resolution constraints. The resulting measurements of the primary quantities which in the current investigation are essentially concentrations of the passive and the reactive scalar are span integrated values. The derived quantities scale from plane averaged values and above.

3.1. WORKING PRINCIPLE OF THE DIAGNOSTIC

All the liquids used in the current investigation are transparent and do not attenuate light except for the passive scalar-Nigrosine and the reactive scalar-Phenolphthalein in its ionized form. The reaction chemistry detailing the ionization states and the optical nature of Phenolphthalein during the different pH ranges encountered during the course of the experiment will be detailed subsequently. The indicators are therefore detected by absorption in light characteristic of their absorption spectrum. The attenuation of light ray passing through the span of the test section, marked by a decrease in intensity over the incident intensity as recoded by the camera is related to the span integrated concentration of the indicator in the mixing layer by the Beer-Lambert law [75], given by:

$$\sigma = -\ln\left(\frac{I}{I_0}\right) = \varepsilon \int_0^L [In]dy = \varepsilon L\left[\overline{In}\right] \tag{3.1}$$

where σ is the absorption of light by the indicator, measured as attenuation in the measured intensity I with respect to the incident intensity I_0. According to this law, the amount of absorption is directly proportional to the length of the path travelled by light ray, at a given concentration of the indicator – *In*, denoted by the square brackets [*In*], ε being the constant of proportionality called as the molar absorptivity coefficient. As a direct consequence of the above relation it follows that for a calibrated value of ε the concentration of the indicator can be linearly related to the absorption of light. Though the law is universal, the non-linearity of the imaging sensor sensitivity at low intensities sets the concentration bounds under which the set up needs to be operated for a given

span of the test section - L. $\left[\overline{In}\right]$ denotes the span wise averaged concentration of the solution which is the measured quantity in the current set-up.

3.2. REACTION CHEMISTRY

It is important in the current investigation to study the behavior of the reaction mixture and the reactive scalar (phenolphthalein) in order to measure its concentration accurately. In the current experiments involving the reactive scalar the pH of the heavy fluid is maintained alkaline ($pH_1 > 7$) and the pH of the lighter fluid is maintained either acidic or neutral ($pH_2 \leq 7$). Measured concentration of phenolphthalein is mixed along with the lighter fluid during all the runs.

In aqueous solutions, the concentration of hydrogen and hydroxide ions remain balanced as per the reversible reaction:

$$H_2O \rightleftharpoons H^+ + OH^- \tag{3.2}$$

The equilibrium constant for the above reaction is given by:

$$K_w = [H^+]\,[OH^-] = 10^{-14} \tag{3.3}$$

where the square brackets denote the molar concentrations in moles/liter. As the light and the heavy fluids mix the local concentration of H^+ and OH^- adjust to a new equilibrium satisfying 3.3. The pH of the mixture is then given by $pH_{mix} = -\log_{10}[H^+]_{mix}$. The pH is controlled by adding either NaOH or HCl to either stream. The acid and the base react in stoichiometric amounts to produce NaCl and H_2O and liberate 59.8 KJ of heat per mole. For the extreme pH case considered in the current study where the pH of the streams is 11.5 and 2 the reaction produces a local temperature change of ~0.02°C and therefore has a negligible effect on the Atwood number or on the buoyancy effects driving the mixing.

To track this neutralization reaction a small amount of indicator ($5x10^{-6}$ Mole/liter), phenolphthalein ($C_{20}H_{14}O_4$) is injected into the bottom stream. While the chemistry of neutralization is straight forward the chemistry of the indicator is complex. Phenolphthalein is a weak acid dissociates based on the local pH according to the reaction:

$$\text{Transparent Indicator} + 2OH^- \rightarrow \text{Colored indicator} \tag{3.4}$$

The indicator has multiple ionization states and therefore several different chemical forms (denoted by Roman numeral subscripts):

$$In_I \rightleftharpoons In_{III} + H^+ \quad (3.5)$$

$$In_{III} \rightleftharpoons In_{IV} + H^+ \quad (3.6)$$

$$In_{III} \rightleftharpoons In_{VII} + 2H^+ \quad (3.7)$$

All the forms of the indicator above are colorless except for In_{IV} which exists in pink quinine phenolate form. As the pH of the mixture rises above 8 the equilibrium of the first two reactions moves to the right as per Le Chatelier's principle, and the colored form of the indicator is produced. However as the pH of the mixture increases beyond 11.5, the equilibrium of the last reaction moves to the right and less of indicator is available in the colored form.

The fraction of dissociation of the indictor in the colored form is another factor that is dependent on the pH of the local mixture. Phenolphthalein exhibits an abrupt and high dissociation value (α_{InIV}^{max}) of 0.96 (meaning 96% of the indicator exists in the) colored form at a pH of 11.3. The indicator reaction has been shown to be sufficiently fast to capture mixing dynamics in turbulent jets operating at Re~32,000[65]. For the current investigation a Damkohler number ((Da) which is the ratio of hydrodynamic to reaction time scales) of > 40 would suffice, while the indicator exhibits a Da ~O(10^5) and is therefore a suitable indicator to capture dynamics in the current investigation.

3.3. CALIBRATION PROCEDURE

In the present investigation the molar absorptivity coefficient of both Nigrosine and the colored form of Phenolphthalein were calibrated over the entire span of the test section. The calibration procedure involved the set of the experiment and the diagnostics as per the schematics given in the previous section for the respective indicator. The lower portion of the test section was then filled with distilled water and the pH was adjusted to a value of 11.5 in case of the calibration of the reactive scalar. The pH level was maintained so that most of the indicator in the test section was in its colored form. The sensitivity of the indicators dissociation coefficient to its colored form and the high absorptivity of green light are a very important factor that needs to be controlled so as to perform accurate calibration. To this effect a pH meter and a micropipette were used so as to ensure accurate pH control of the fluids in the top half and the bottom half of the test section. The amount of light absorbed by the indicator was recorded while varying

the concentration of the indicator from zero incrementally over a range of concentration values till saturation in the recorded intensity was observed. The slope from a plot of absorption versus the product of indicator concentration and the span of the test section yielded the molar absorptivity coefficient values. Figures 3.1 and 3.2 present the calibration curve obtained by the above procedure for Nigrosine and Phenolphthalein. A regression fit to the calibration values in the zone of linearity is also shown in the curves and the slope of this line is used as the ε in either case. As it can be seen from the plots, the set-up has a non-linear response for absorptions exceeding 1.3 with Nigrosine and 1.5 with phenolphthalein and so the concentration of the indicator was limited to exclude absorptions above 1.2 in both the cases.

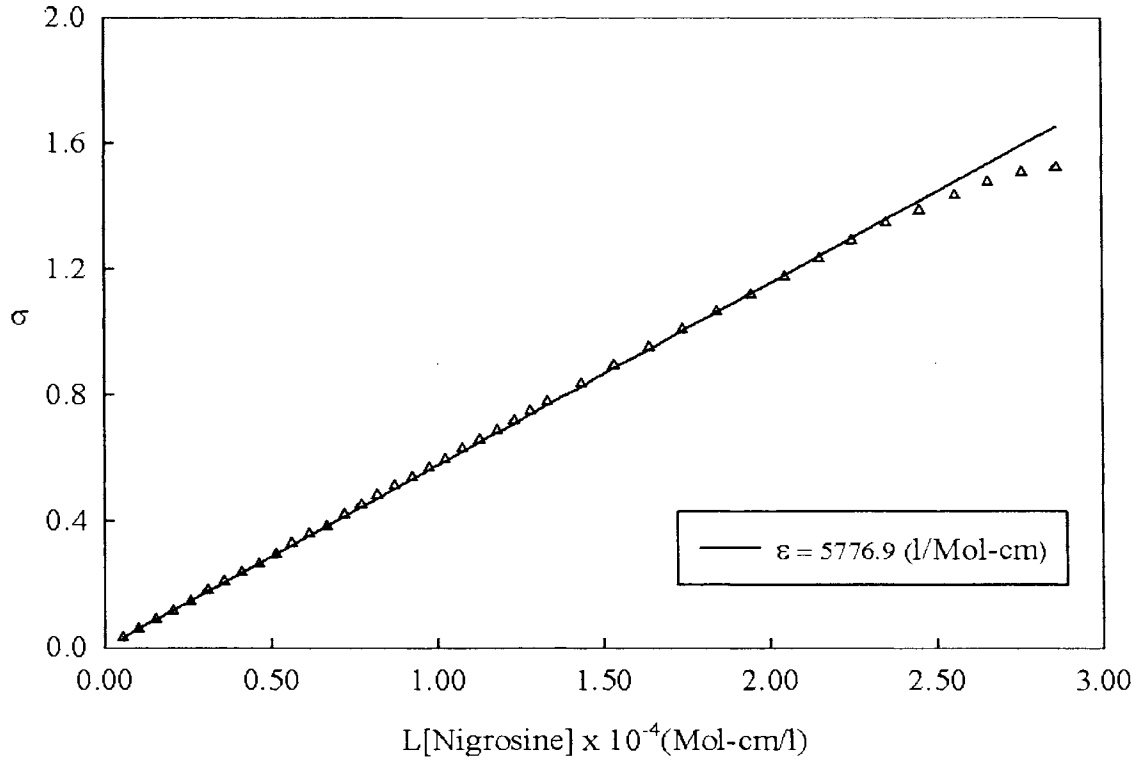

Figure 3.1 Nigrosine calibration curve (σ has uncertainty bounds of $\pm$ 1.5%).

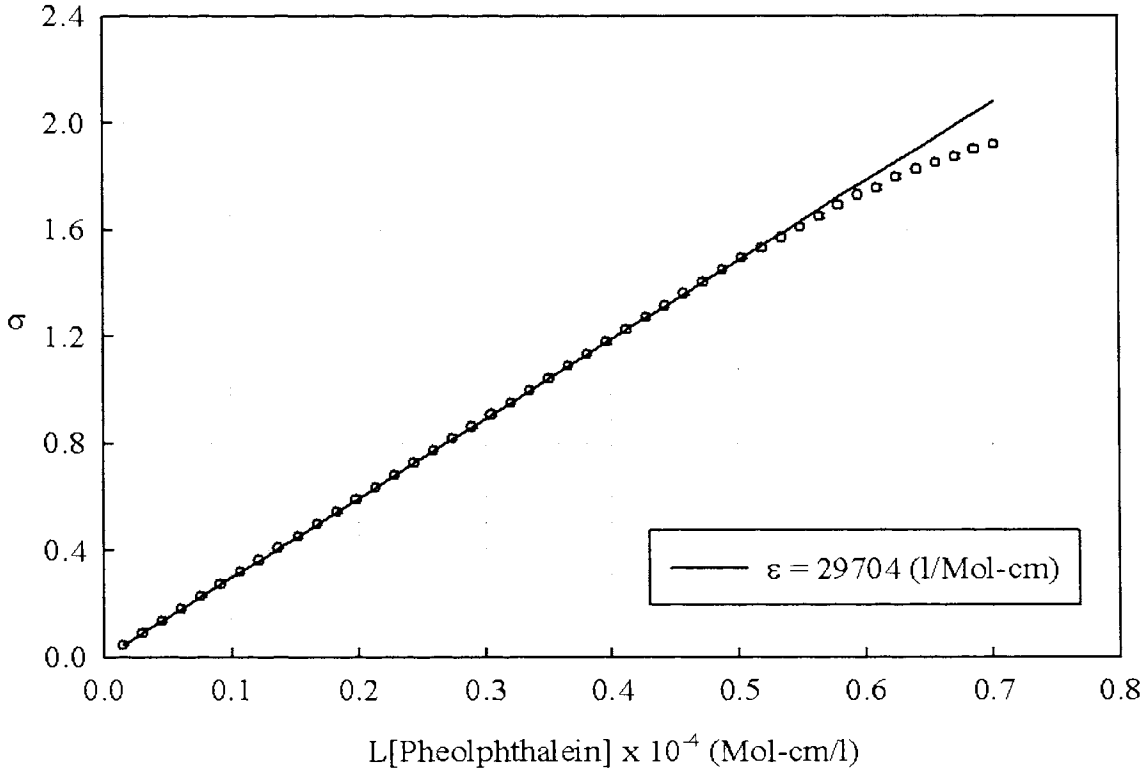

Figure 3.2 Phenolphthalein calibration curve (σ has uncertainty bounds of ± 1.23%).

3.4. UNCERTAINTY QUANTIFICATION

As a check on the accuracy of set-up, estimates of uncertainty in the measured quantities were calculated using Kline and McClintock uncertainty quantification methodology for single sample measurements. Table 3.1 summarizes uncertainties associated with certain salient physical quantities calculated using this methodology. A complete accounting of the uncertainty calculation involved with each quantity is given in Appendix C. The uncertainty in concentration measurements with phenolphthalein is driven by the uncertainty in the initial injected concentration while the uncertainty in volume fraction is driven by the back-ground intensity fluctuations during the course of the experiment. Even though ε of Nigrosine has the highest uncertainty in relating to concentration it does not percolate into the volume fraction estimates as the amount of Nigrosine mixed in the fluid can be estimated by measuring absorption in the top half of

the tank, this way the volume fraction estimates carry a smaller amount of uncertainty. The ε of Phenolphthalein on the other hand is instrumental in the determination of the normalized concentration due to two reasons, one being the nature of indicator to be unviable for priori optical measurement and the second being the incomplete dissociation of the indicator in its colored form even on complete reaction, as the amount of visible indicator formed is governed by the mixture ratio of the participating fluids.

Table 3.1. Summary of uncertainty bounds for measured quantities.

Physical Quantity	**Symbolic reference**	**Uncertainty**
Incident Intensity	I_0	± 0.78%
Absorption	$\sigma = -\ln\left(\frac{I}{I_0}\right)$	± 0.5%
Length	L	± 0.654%
Volume of water	V_0	± 0.315%
Volume of phenolphthalein injected	V_2	± 0.6%
Total Concentration of phenolphthalein Injected into the flow	$[In]_2$	± 0.67%
Molar absorptivity coefficient of phenolphthalein	ε	± 1.23%
Normalized Concentration of Phenolphthalein	$C = [\overline{In_{IV}}]/[In]_2$	± 1.75%
Volume of Nigrosine injected	V_1	± 0.6%
Total Concentration of Nigrosine Injected into the flow	$[Dye]_1$	± 1.07%
Molar absorptivity coefficient of Nigrosine	ε	± 1.5%
Span Average Volume fraction of heavy liquid	$f_1 = [\overline{Dye}]/[Dye]_1$	± 1.15%
Atwood number	A_t	± 4.67%
Alpha	α_b	± 4.18%

Molar absorptivity coefficient for phenolphthalein has been measured as 29704 ± 1.23%, including the uncertainty bounds the value stands in fair agreement with similar measurements by Mueschke (29350 ± 0.67%) [9]and Zhang (29340) [65]. The spike in the absorptivity coefficient may be attributed to the increased sensitivity resulting from the usage of a CMOS sensor in comparison with the CCD array employed by the other two investigations. The uncertainties in the rest of the physical quantities that are computed as part of the investigation are basically derived from these fundamental quantities.

4. RESULTS AND DISCUSSION

The results presented in the section are from an ensemble average of four runs for the passive scalar and from 4 for each pH combination in case of the reactive scalar. One Table 4.1 presents a summary of the experimental runs performed as part of the current investigation. As it can be seen, 1 successful run in about 4-5 trials (~20-25% success rate) could be achieved with the current set-up. The dominant factor contributing to the failure is the difficulty in ensuring uniform wrapping of the Nylon strips around the barrier ends as it is being pulled. Adhesion of top Nylon strip to the barrier due to presence of Vaseline, leaks from the side grooves prior to start of the experiment due to break in Vaseline seal at high hydrostatic head, stall due to nylon wrapping inside the barrier while being withdrawn, Nylon not wrapping due to insufficient push force compared to the pull in the manual operation, Vaseline blobs contaminating the flow are some of the major contributors to the failure of the experiments. Typical set-up time for the experiment for the passive scalar case took 4-5 hours while the set-up time for the experiment with reactive scalars took about 5-6 hours as it was more involved in terms of ensuring absence of indicator on the top of the barrier which required special cleaning procedures. All the experiment was conducted during night time as it was difficult to block out sunlight entering the test section during the daytime which measured up to 7-10 intensity units despite the best blocking efforts limiting experiments to 2 per day.

Table 4.1 Summary of experiments performed.

Run description	**Reported runs.**
With Nigrosine	4
With Phenolphthalein pH_1=11.5; pH_2=7.05	4
With Phenolphthalein pH_1=11.5; pH_2=3.04	4
With Phenolphthalein pH_1=11.5; pH_2=2.57	4
With Phenolphthalein pH_1=11.5; pH_2=2.03	2
Total	18

4.1. MIXING LAYER GROWTH FROM PASSIVE SCALAR RUNS

Experiments involving the usage of passive scalar have been conducted to as to ascertain volume fraction detail of the constituent fluids during the evolution of the mixing layer. The current diagnostic capabilities provide for span average measurements of volume fraction at each point on the focal plane. In this study, plane averaged measurements of the volume fraction are used to estimate the mixing layer growth. Nigrosine dye was added to the heavy fluid (top) in the tank and absorption of light was measured using techniques mentioned in the diagnostic section. The amount of dye to be added was estimated using the calibration procedures and the absorptions were related to the mean dye concentration (across the span).

4.1.1. Qualitative Results From Passive Scalar. Figure 4.1 shows a sequence of images at different times in the evolution of the mixing layer for a typical run with Nigrosine. Contrast enhanced images are presented here for better visualization. In order to exclude the effects of the walls, the central 80% of the domain dimensions were considered for quantitative analysis[56]. A 2.0 cm wide region towards the bubble side from the mid-plane and 1.0 cm towards the spike side were optically unviable for measurements due to the presence of groove holding the barrier and the Vaseline (used for preventing seepage of the top fluid into the bottom around the edges) smeared onto the edge during barrier operation. The barrier was manually withdrawn and usually takes 2-3 seconds for removal at an approximate velocity of 0.12 m/s. It has been reported that the spatial structure of the wake left on barrier removal remains the same with the variations in the time involved while the variations reflect in the strength of the perturbations that have been imparted at the interface[25]. The experiment ensues a transient turbulent mixing layer by design and would therefore require a very large number of realizations to attain statistical convergence on higher order flow metrics. This limits the facility to investigations that relate to quantitative explanations of a phenomenal order rather than to engineering precision.

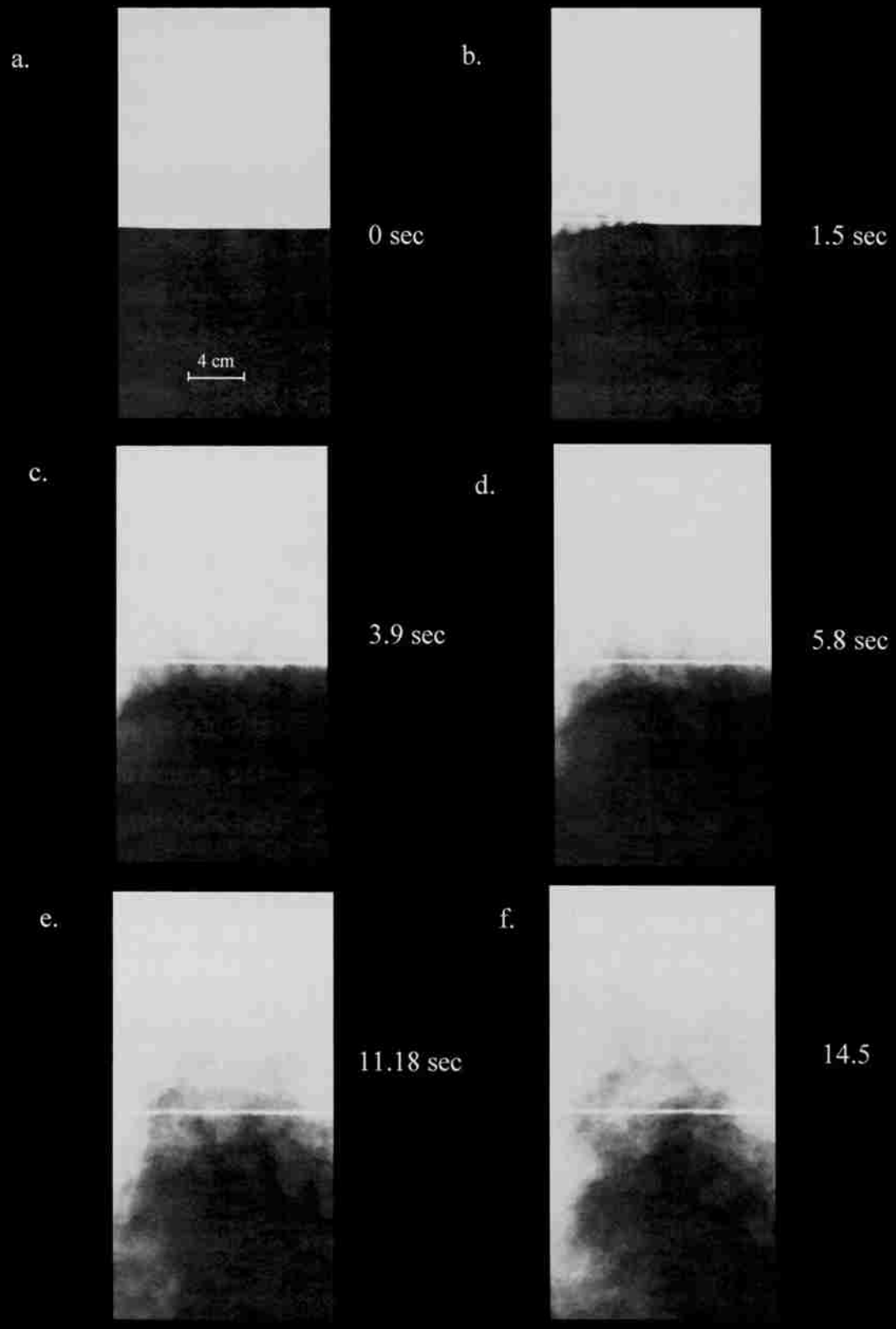

Figure 4.1 Evolution of the RTI driven mixing layer with passive scalar (A_t=7.5 $\times 10^{-4}$).

The formation of the fluid plume is an artifact of barrier removal and can be explained as follows. As the barrier is removed, the upper layer moves downward to replace the volume of the barrier no longer in the tank. The floating lid forces this motion to be essentially uniform along the length of the tank. While there is a potential energy change associated with the change in free-surface height, it is exactly balanced by the work done on the barrier by the hydrostatic component of the pressure acting on the end of the barrier, and may thus be ignored [25]. If the barrier is withdrawn at a constant velocity, then the upper layer adjusts downwards at a constant velocity. However, at the level of the barrier, the area over which this adjustment is made depends on how far the barrier has been withdrawn. At the initial instant this area is very small, inducing extremely large velocities towards the trailing edge of the barrier. With the barrier further out, the horizontal area over which the adjustment takes place is increased, reducing the magnitude of the velocities. This can be observed in the sequence of images shown in Figure 4.1 where the development of the interface shows a variation in the extent of the spatial structure formed by interpenetration of the fluid packets as a result of the increasing area for adjustment due to barrier removal. The resulting plume travels faster in reaching the bottom of the domain as the mixing layer takes to reach the top of the domain. The growth of the mixing layer on the spike side is therefore very complex as it is initiated and dominated by a turbulent plume and has the coupled dynamics of plumes and RTI while the bubble side evolution is initiated by a dominant spatial perturbation than velocity perturbation. To this effect, all further analysis will be confined to the bubble side.

4.1.2. Quantitative Results From Passive Scalar. The mean dye concentration was normalized by the dye concentration of the pure heavy fluid and this was related to the volume fraction of the heavy fluid by the relation:

$$\overline{f_1} = \frac{\overline{\rho} - \overline{\rho_2}}{\overline{\rho_1} - \overline{\rho_2}} = \frac{\overline{[Dye]}}{[Dye]_1} \tag{4.1}$$

where $\overline{f_1}$ is the dimensionless measure of the mean density field and the overbars denote planar averaged quantities. Figure 4.2 shows the evolution of $\overline{f_1}$ over the entire test

section at different times. In general, the growth of small-Atwood RTI mixing layers is supposed to be symmetric about the interface and linear on both the bubble side and the spike side[33, 56]. The mixing layer shows linear variations in the growth profile but the symmetry is skewed owing to an initial plume of fluid that enters the bottom half of the tank.

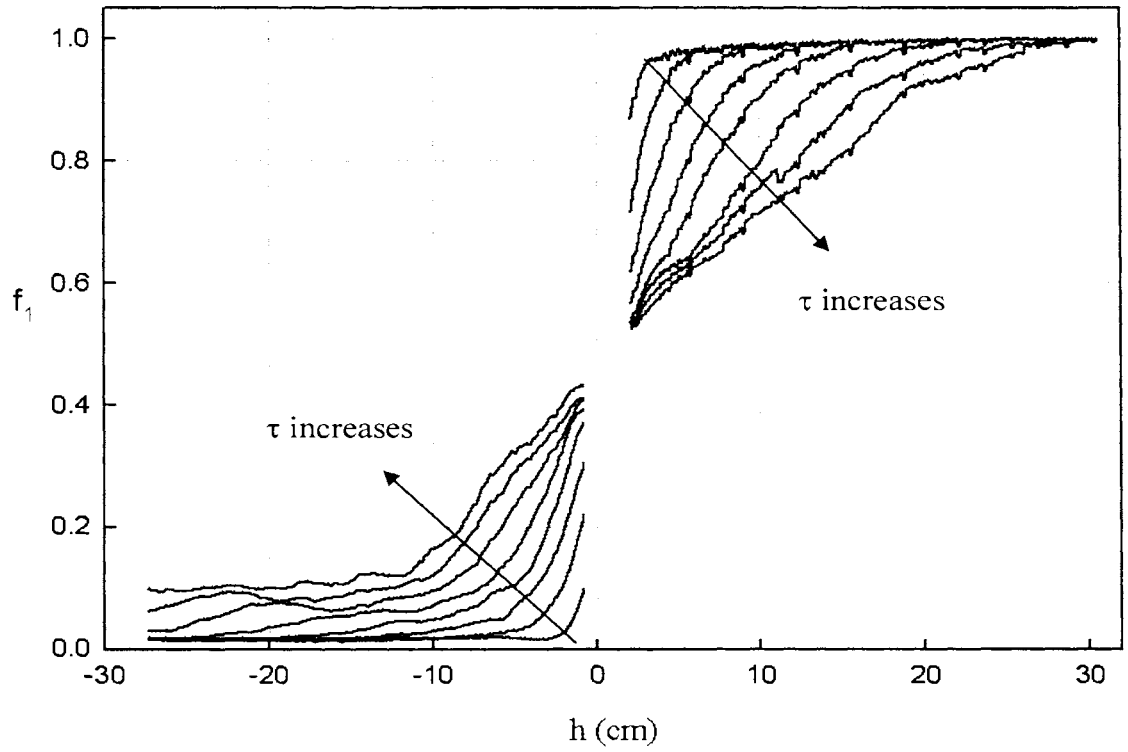

Figure 4.2 Evolution of the heavy fluid volume fraction at various non at τ ranging from 0.25 to 2 at an interval of 0.25.

The bubble height is measured by identifying the 5%-95% thresholds from the $\overline{f_1}$ data. Figure 4.3(a) and (b) shows growth of the mixing layer half-width on the bubble side (or bubble height) as a function of the $A_t g t^2$ and τ, respectively.

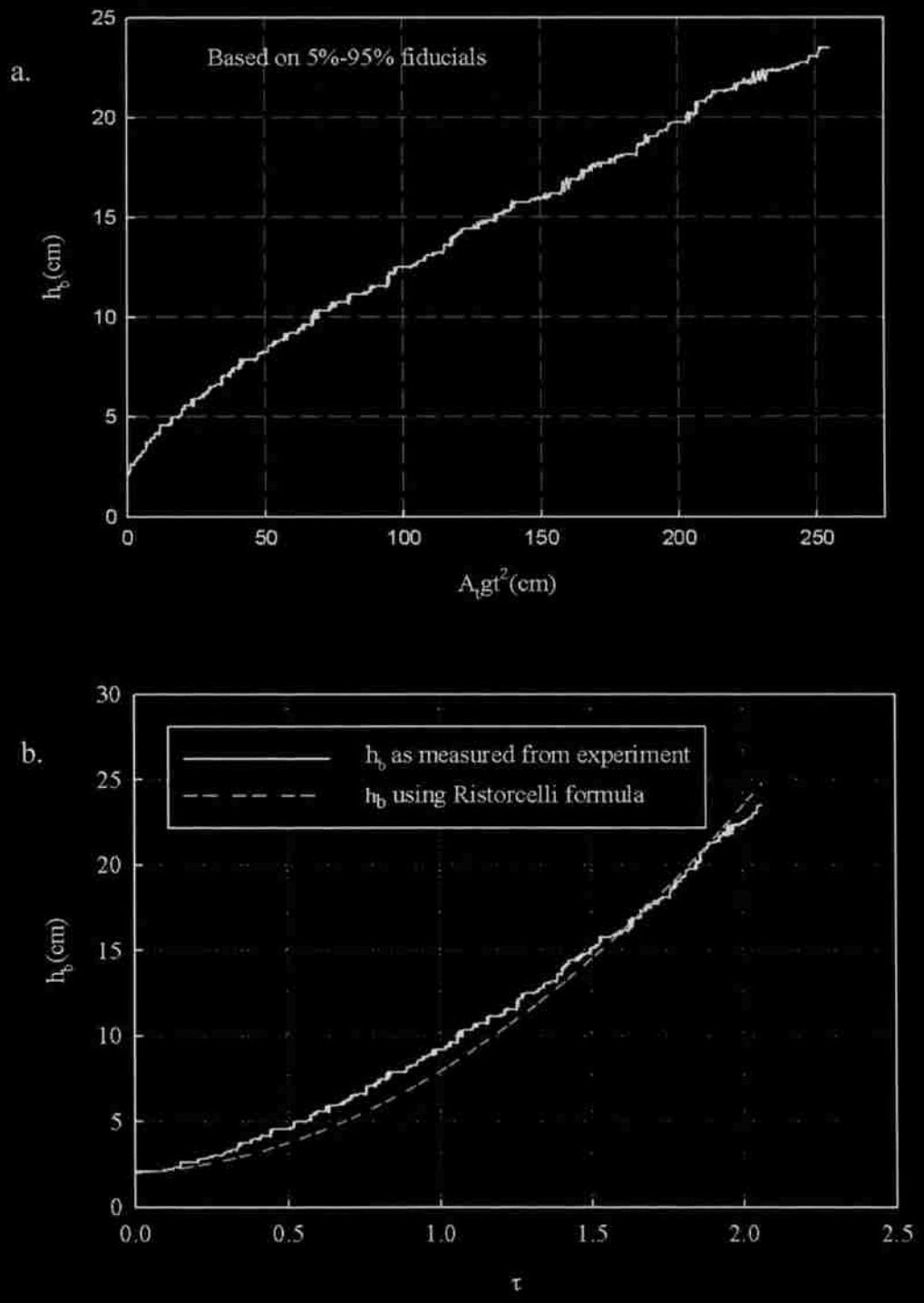

Figure 4.3 Growth of the bubble height based on 5%-95% fiducials as a function of (a)$A_t gt^2$- the most dominant length scaling and (b) τ.

Ristorcelli and Clark [29] showed that a measurement of α_b directly from the relation $h_b = \alpha_b A_t g t^2$ is not independent of additional terms that scale as t^1 and t^0 and so

proposed an ordinary differential equation based on self similar analysis for small-Atwood RT mixing layer half-width given by:

$$\alpha_{b,RC} = \frac{\dot{h}_b^{\,2}}{4 A_t g h_b} \tag{4.2}$$

Where all quantities with subscript "b" correspond to the bubble side and the sub script *RC* denotes the self-similarity constant arrive from Ristorcelli and Clark definition. For constant $\alpha_{b,RC}$, A_t and g, the solution to the above equation (taking only the positive root as physically realizable) can be written as:

$$h_b = h_0 + 2\sqrt{\alpha_{b,RC} A_t g h_0}\, t + \alpha_{b,RC} A g t^2 \tag{4.3}$$

where h_0 is a virtual starting thickness. The virtual thickness is a measure of the time taken for the flow to become self-similar and depends on the initial perturbation spectrum. The plot in Figure 4.3(b) also shows a fit (in blue) based on the above equation with a $h_0 = 2$ cm, $\alpha_{b,RC} = 0.085$. From the graph we can infer late time agreement between the experimentally observed values and a quadratic fit as per equation 4.3 using the constants mentioned above. Due to the transient nature of the experiment a lot of fluctuation can be observed in the resulting half-width evolution and so there is a lot of fluctuation observed in the value of α_b calculated based on the definition in equation 4.2. The fluctuations and the resulting discrepancies in the growth rate parameters due to lack of statistical convergence have been observed in other transient experiments and numerical investigations. To work around this problem Andrews & Spalding [39] defined an integral mix-width given by:

$$W_b = 6 \int_0^{H/2} \overline{f_1 f_2}\, dy = \alpha_{b,W} A_t g t^2 \tag{4.4}$$

The factor of 6 comes from assuming a linear profile of the volume fractions which is a valid approximation for the volume fraction profiles on the bubble side. Figure 4.4 shows the evolution of the integral mix-width as function of non-dimensional time. It can be seen that fluctuations originating from the nature of the experiment are mitigated using this approach. A corresponding definition of α based on the Ristorcelli & Clark[29] definitions on the integral mix-width is given by:

$$\alpha_{b,RC,W} = \frac{\dot{W}_b^{\,2}}{4A_t g h_b} \tag{4.5}$$

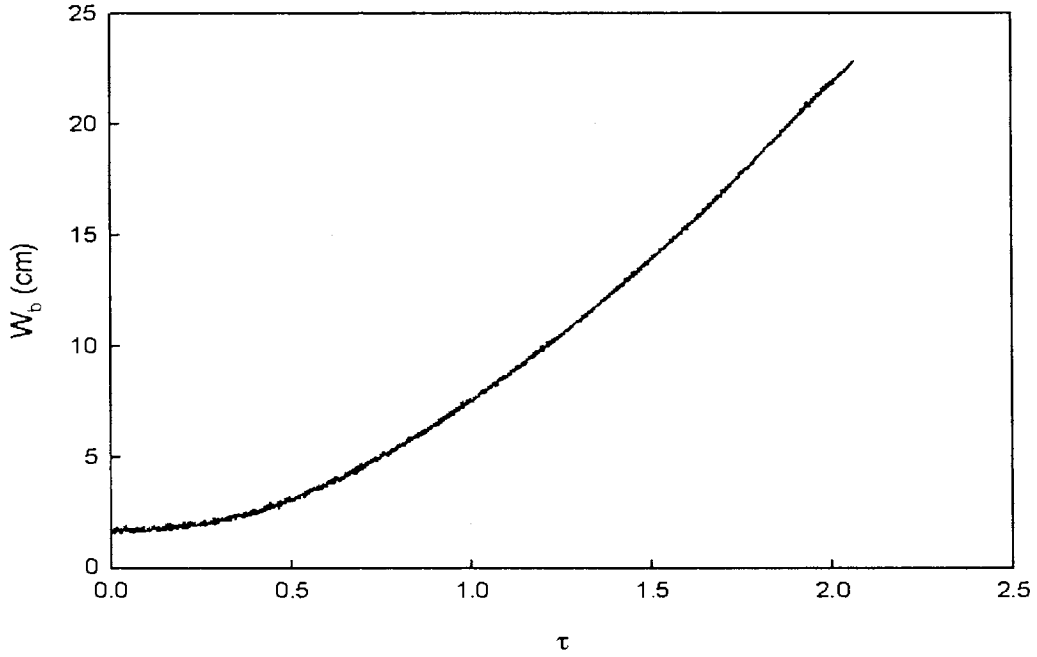

Figure 4.4 Evolution of integral mix width.

Figure 4.5 presents the evolution of α_b computed using the Ristorcelli and Clark definition on the mix width and the integral mix width. $\alpha_{b,RC}$ value of 0.085±0.0035 is reported from the current investigation.

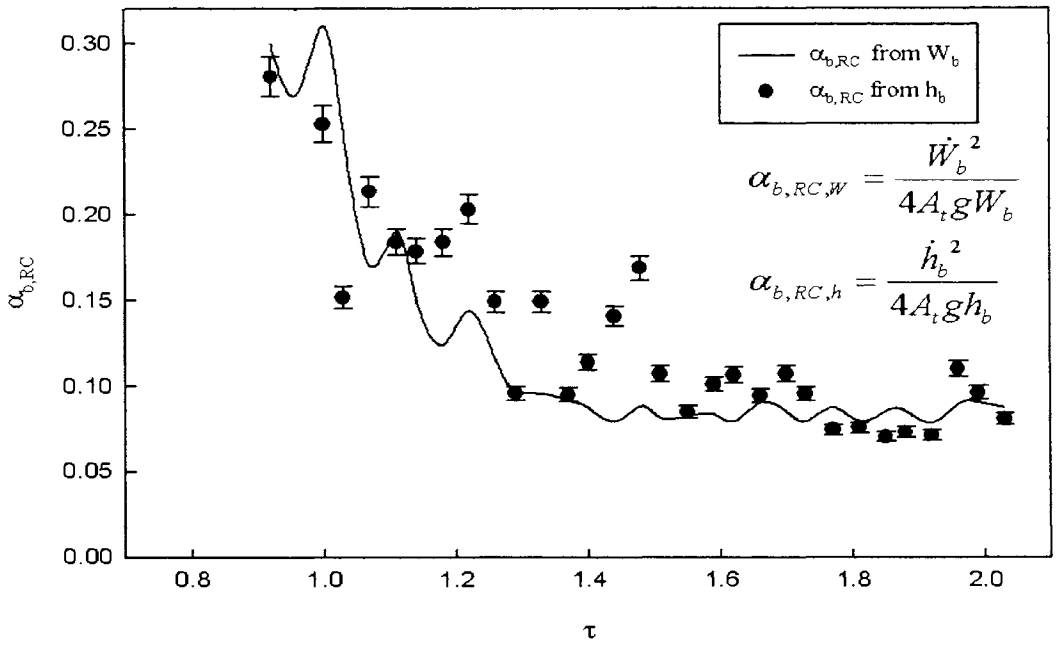

Figure 4.5 Evolution of self-similarity parameter calculated using Ristorcelli & Clark definitions based on bubble height and integral mix-width.

4.2. INITIAL CONDITION ESTIMATES FROM PASSIVE SCALAR RUNS

The results from the passive scalar and the imagery were used to estimate the initial conditions of the experiments. The initial conditions of the experiment were calculated based on a wave counting methodology that is described in the appendix. The method essentially estimates the most dominant wavelength and the connected amplitude that described the wake upon removal of the barrier. The nature of the initial perturbation for the modeling methodology was assumed to be two dimensional as was observed in the wake. The estimates were then validated by simulations using an Implicit Large Eddy Simulation (ILES) using an in house code – RTI3D[72]. The validation exercise was performed on the self-similarity growth rate parameter α_b, representative of growth of the flow on the largest scales and is resolved by the computations. Estimates of molecular mixing were not compared as the code operates at a *Sc* of 1 with numerical diffusion while the experiment operates at a *Sc* of ~1000. The observations asserted by works of Mueschke et al.[9], wherein the effect of *Sc* on α were found to be marginal form the basis for such a comparison.

4.2.1. Governing Equations. The ILES code resolves the mixing layer in 3 dimensions (Cartesian) by solving the Eulerian equations given by:

$$\nabla . \underline{u} = 0 \tag{4.6}$$

$$\frac{Df}{Dt} = 0 \tag{4.7}$$

$$\frac{D(\rho \underline{u})}{Dt} = -\nabla p + \rho \underline{g} \tag{4.8}$$

where the equations represent the governing equations for volume conservation, scalar transport and momentum conservation. In the equations, the representative velocity components in 3 dimensions are given by $\underline{u} = (u,v,w)$, density by ρ, pressure by p, gravity by $\underline{g} = (0,0,g_z)$ and the scalar by f. The system of equations has 6 variables and 5 unknowns and the closure is obtained by a linear equation of state connecting the scalar and the density such that $\rho = L(f)$. The present work defines the non-dimensional density given by $f = (\rho - \rho_2)/(\rho_1 - \rho_2)$ to be representative of the scalar. The code solves the above set of governing equations and employs numerical diffusion to model turbulent diffusion. This methodology of arriving at solutions has been found to be fruitful in modeling the flow accurately at a Schmidt number of 1[33]. The details of the solution procedure employed for solving the coupled set of partial differential equations can be found in the works of Andrews[72, 76]. While the solver does not employ explicit viscosity, numerical diffusion serves to dissipate small scales in a manner similar to physical viscosity and therefore provides us the leverage to observe aggregate behavior without loss of accuracy on not modeling the small scales. This is also the reason for the restriction in the Schmidt number of the flow that can be resolved by the solver. The code has been extensively used to compute single-mode and multimode RTI driven flows [30-31, 70, 77] and the results have compared well with other bench mark codes that have been used for numerical evaluation of RTI.

4.2.2. Simulation Setup. The size of the domain chosen here is representative of the test section and measure 0.3m x 0.3m x 0.6m in the x, y and z directions, respectively. The boundary conditions are periodic in the x and y directions and zero flux boundary conditions are enforced in the z –direction along which gravity acts. As the boundary conditions are periodic it is important to choose wavelengths that have an integral number of occurrence over the domain which is given by the mode number defined as N = λ/L where λ is the wavelength of the perturbation and L is the span of the domain. The wavelengths that were used to seed the initial perturbation were from the observed modes over an ensemble of 4 experiments. A mode number corresponding to 5.5 was observed on averaging with the distribution varying from 4-6 and so a spectrum of wavelengths ranging from 4-6 were chosen to initialize the density perturbation at the interface. The root mean square (rms) value of the density perturbations which is representative of the energy carrier by the modes calculated using the amplitudes of the perturbations was adjusted till there was an approximate match with the amplitude of the perturbation observed in the wake of barrier removal. This resulted in a rms amplitude of 0.007 to be distributed with equal energy among modes 4-6. The Cartesian translation of equal energy distribution between the wave numbers is done by assigning initial (t = 0) amplitude (h) on the nodes of the x,y plane at z = 0:

$$h(x,y) = \sum_{k_x,k_y} (a\cos(k_x x)\cos(k_y y) + b\cos(k_x x)\sin(k_y y) + c\sin(k_x x)\cos(k_y y) + d\sin(k_x x)\sin(k_y y)) \tag{4.9}$$

where a,b,c,d are random numbers and k_x and k_y represent the 2-D wave-number space which is related to the mode number (k) by $k = \sqrt{k_x^2 + k_y^2}$. The resulting $h(x,y)$ field is rescaled so as to provide the necessary rms density perturbation. The effect of higher mode numbers with a tenth of the energy of the dominant modes was studied by seeding the interface with mode number 10-32 and the results only varied marginally as there was an order of magnitude difference in the amplitudes causing the lower modes to dominate the flow. Furthermore as a validation exercise the rms value of the amplitudes measured from the experiment was distributed in the spectrum modeled to represent the density perturbation spectrum of the water channel[77]. With the mode numbers used to seed the initial perturbations limited to 32, a grid resolution of 128x128x256 was chosen over the

domain. Figure 4.6 presents a schematic of the computational domain and a pictorial view of the initial density perturbation used in the two cases.

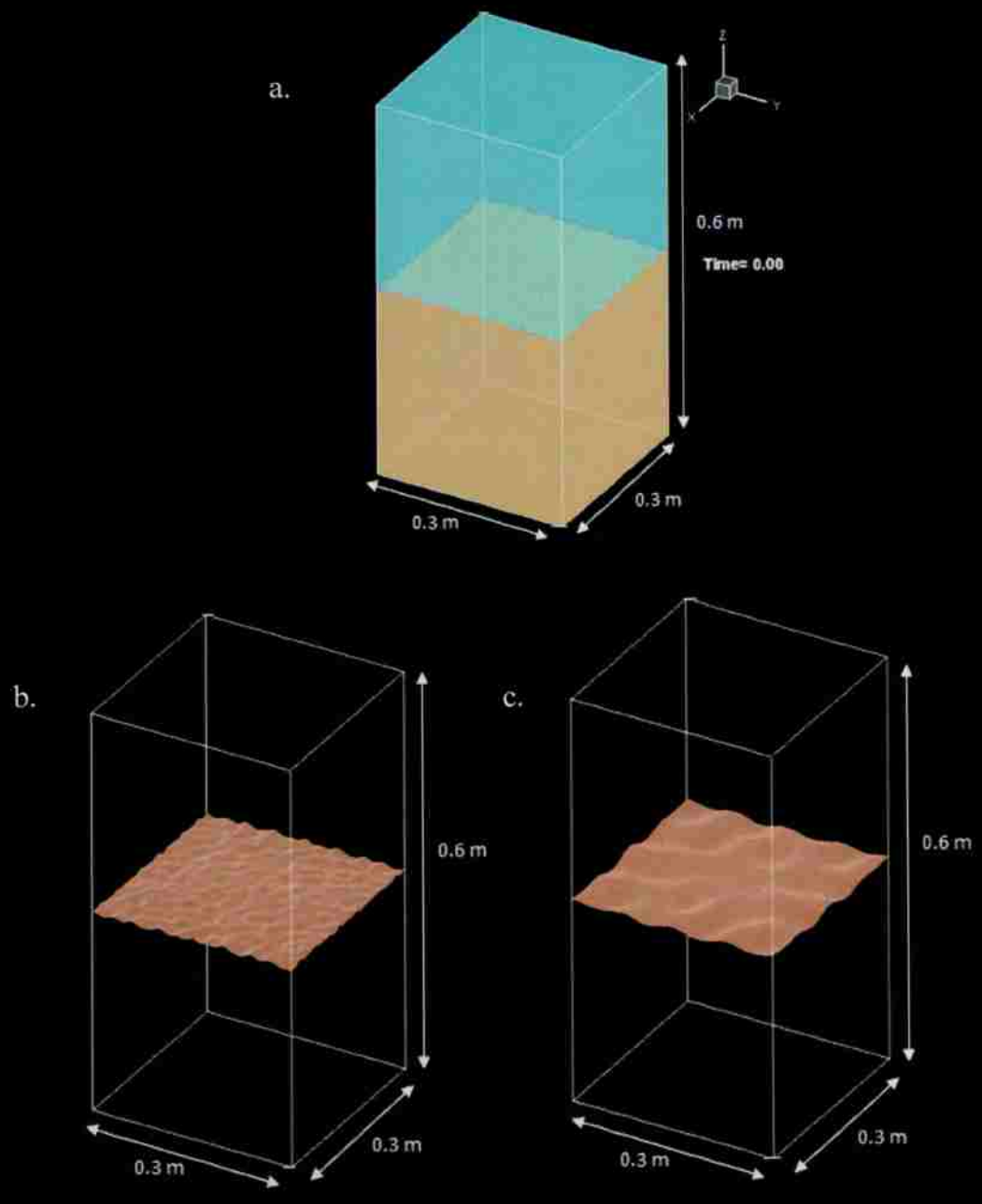

Figure 4.6 (a) Schematic of the computational domain showing with the heavy fluid on the top(red) the light fluid at the bottom (blue) and a perturbed interface; (b) and (c) show initial perturbations for simulating water channel and the current experiment, respectively.

Figure 4.7 gives the spectrum of the modes seeded in the initial perturbation for the two cases considered here.

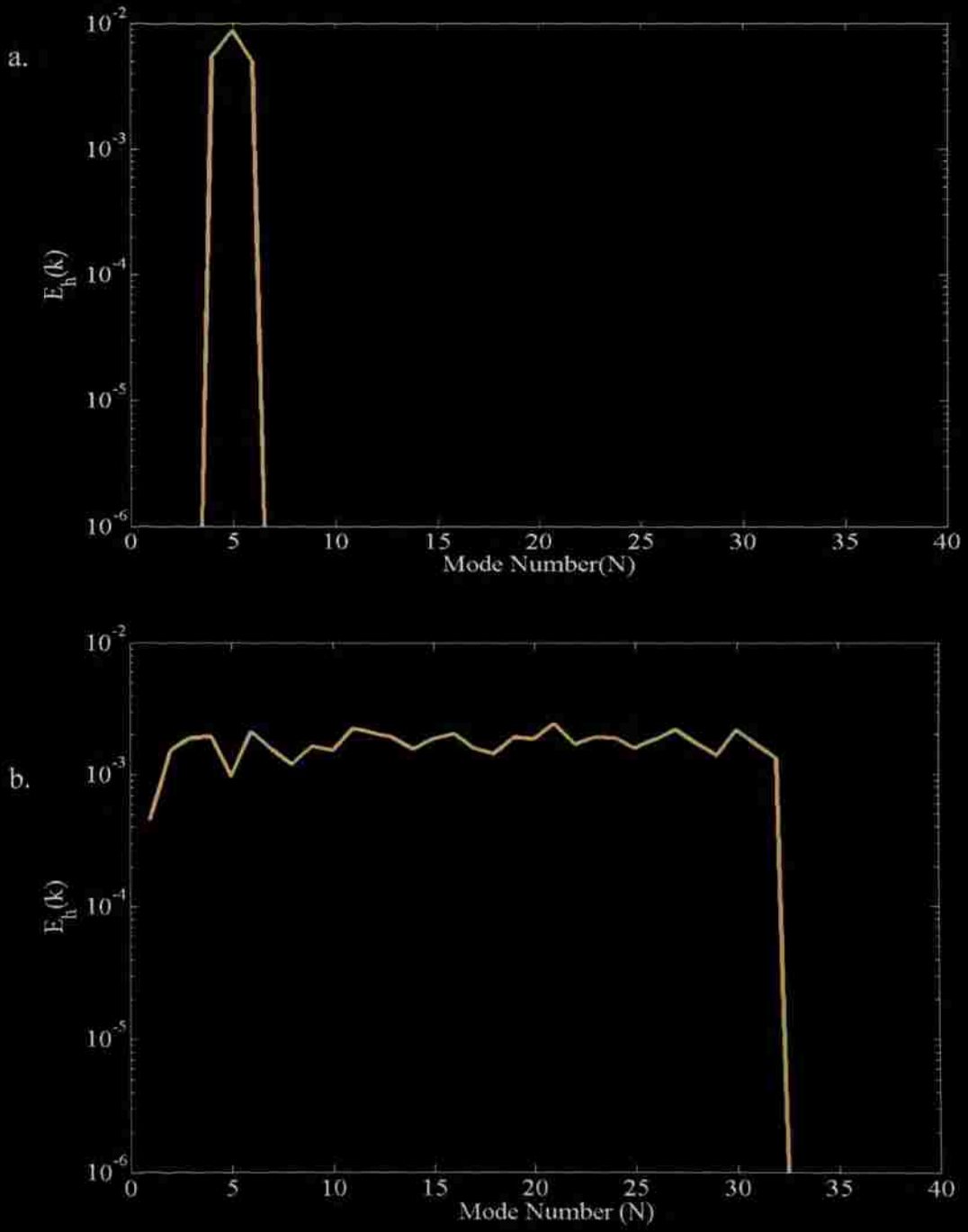

Figure 4.7 (a) and (b) depict the spectrum of initial conditions that were modeled from the current experiment and the water-channel[77], respectively.

Figure 4.8 presents contours of the density perturbation at the plane $z = 0$ for the different cases considered here. The code in its current form runs as a single thread and took an execution time of 4 hours on a Dual Quad core machine with a processor speed of 2.4 GHz and a RAM space of 24 GB.

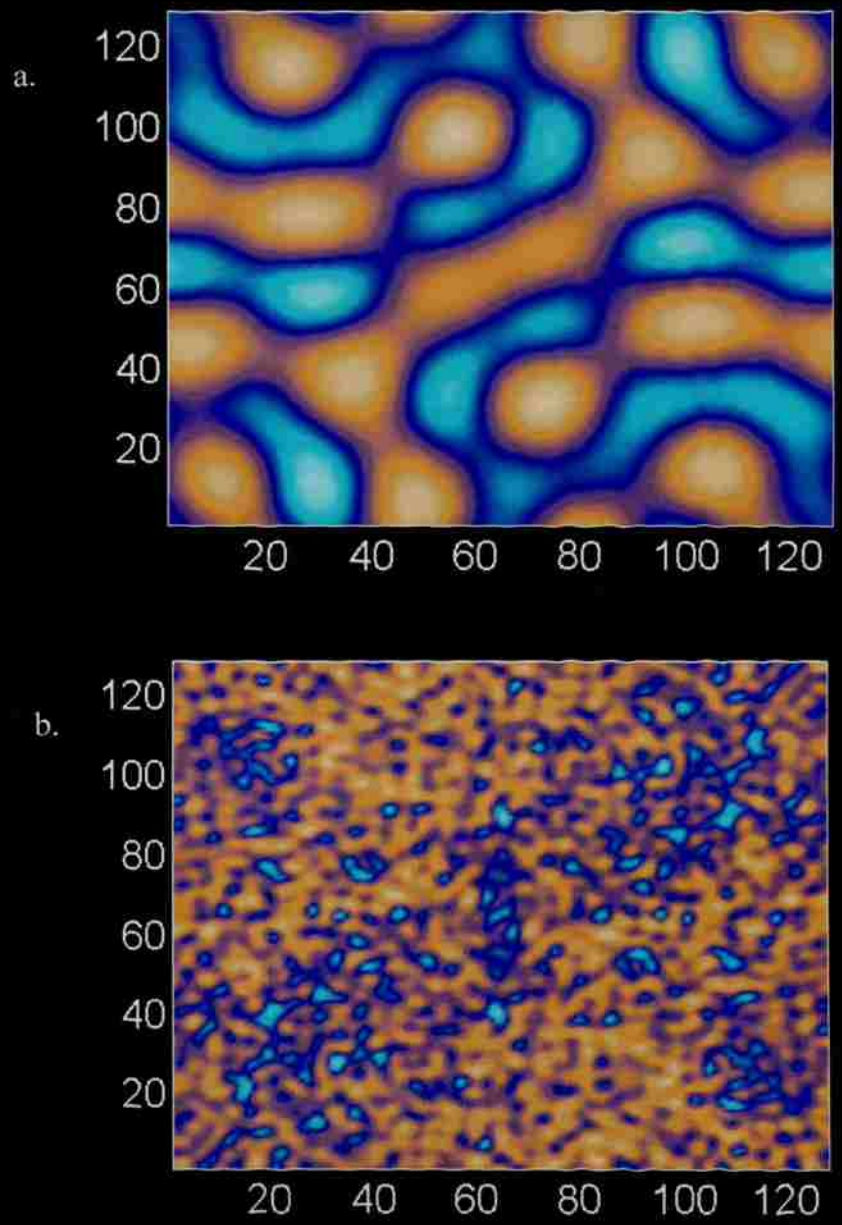

Figure 4.8 (a) and (b) depict the contours of density perturbations at z = 0 plane that were modeled from the current experiment and the water-channel[77], respectively.

4.2.3. Simulation Results. The modeled initial conditions were then validated from the simulation data. As mentioned earlier, the self-similarity growth constant which is representative of growth on the largest scales was used to validate the modeled initial conditions through the simulations. αb values corresponding to 0.0835 and 0.0675 were observed from the simulations corresponding to initial conditions modeled from the current investigation and the water-channel, respectively. The value of αb obtained from simulations seeded with initial conditions from the current investigation is in close agreement with the experimentally observed value of 0.085 and is within the uncertainty of the value. αb values of 0.0675 and 0.07 correspond to the values observed in the water channel from modeled initial condition simulations and experiments, respectively. Figure 4.9 shows a comparison of αb obtained from the experiment and the simulations. The slight deviation in the self-similarity constant arrived from the simulation in both the cases can be attributed to the low Schmidt number of the code.

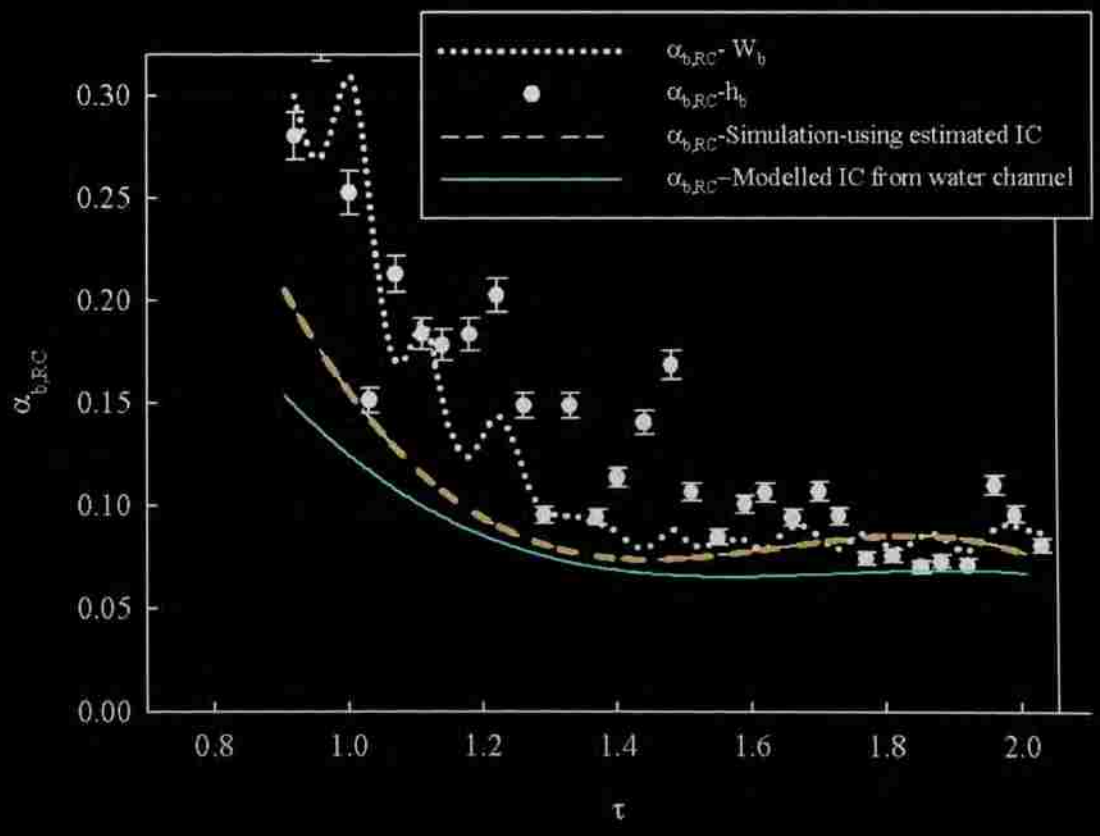

Figure 4.9 Comparison of α_b values obtained from simulations and experiment.

Based on these results, we can see that the simulations are in fair agreement with the values obtained from the experiments with the modeled initial conditions. It can be observed that the most dominant modes in the initial conditions for the current investigations are essentially 2 dimensional and carry most of the energy. Having captured the most dominant modes in the initial perturbations we proceed to pose further comparisons and arguments of variations in the physical quantities based on the modeled initial conditions.

4.3. CONCENTRATION MEASUREMENTS FROM REACTIVE SCALAR RUNS

Experiments using a reactive scalar – Phenolphthalein, which tracks the interface of a diffusion limited chemical reaction indicating the presence of a specific mixture fraction in the turbulent RTI driven mixing layer were conducted. By varying the pH of the two fluids it was possible to track the presence of specific mixture fractions in the mixing layer. The current facility allows to measure span averaged values of chemical product concentrations which are then related to the mixture fraction of the fluids in a given plane. The amount of colored chemical product formed was measured using the backlit imaging techniques described in section 3.

4.3.1. Qualitative Results From Reactive Scalar. Figure 4.10 shows images in sequence of the mixing layer evolution. The pink chemical indicator represents the presence of mixed fluid at a given mixture fraction. For the images shown in Figure 4.10 the colored regions represent a mixture fraction of 99 to 1 of the light and heavy fluids, respectively. The pH combination used for this run is pH1 = 11.5 and pH2 = 7.05. A 99 to 1 mixture fraction thresh hold can be interpreted qualitatively as the threshold marking the interface between the two pure fluids in the mixing layer. It can be observed qualitatively that the amount of colored product formed at early times is low due to the entrainment of pure fluid blobs as marked by the resulting product formation only at the interface between the structures even though the interpenetration (volume fraction change) is significant at the corresponding time as noted from the passive scalar measurements. At late times, increased product formation

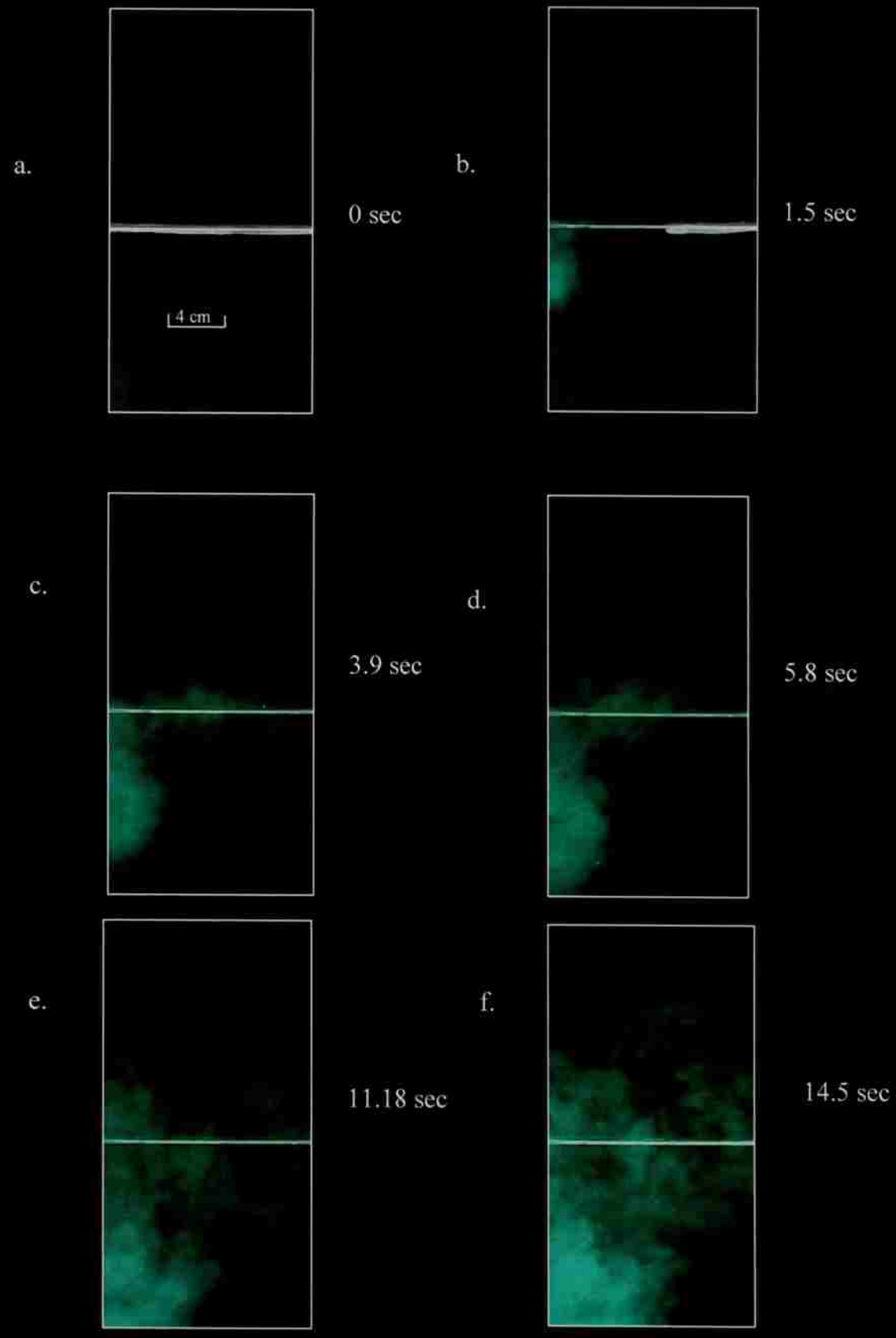

Figure 4.10 Evolution of RTI driven mixing layer with reactive scalar (A_t=7.5 $\times 10^{-4}$).

in the mixing layer can be observed as secondary instabilities at the pure fluid interface and turbulent fluctuations at result in increased segregation and mixing which translates to an increased surface area between the two fluids. Also can observe the bias in the colored product formation in the spike side due to the initial plume of heavy fluid and so we confine our subsequent analysis to the bubble side.

4.3.2. Quantitative Results From Reactive Scalar. Figure 4.11 shows the normalized concentration profiles defined by:

$$C = \frac{\left[\overline{In_{IV}}\right]}{\left[In\right]_2} \tag{4.10}$$

where the numerator represents the measured concentration and the denominator is representative of the total indicator concentration in the lighter fluid, for pH_2=7.05(99 to 1 of light to heavy fluid in the mixture), pH_2=2.57(3 to 1 of light to heavy fluid in the mixture) and pH_2= 3.04(1 to 1 of light to heavy fluid in the mixture). The pH of the heavier fluid (pH_1) was maintained at 11.5 for all the three cases. It can be seen that there is a decrease in the amount of indicator formed as the pH of the light fluid decreases. This is expected as with higher acidity a higher amount of fluid from the heavy fluid section is required to neutralize the acid bring about the necessary change in the pH of the mixture for the indicator to change its color. In all the cases the amount of chemical indicator formed increases as the mixing layer evolves showing that there is increased mixing as the instability progresses. This is expected, as the intensity of turbulence increases and the internal structure of the mixing layer becomes more complex with increasing Reynolds numbers. Turbulent fluctuations continuously stretch the interface between pockets of fresh water and salt water, which increases the reaction surface area and brings fresh reactants into contact. A fourth set of experiments with pH_2 = 2.03 (1 to 3 of light to heavy fluid in the mixture) were run but there was no observable chemical indicator formation and so subsequent calculations of molecular mixing were based on the concentration data arrived from the three pH combinations mentioned above.

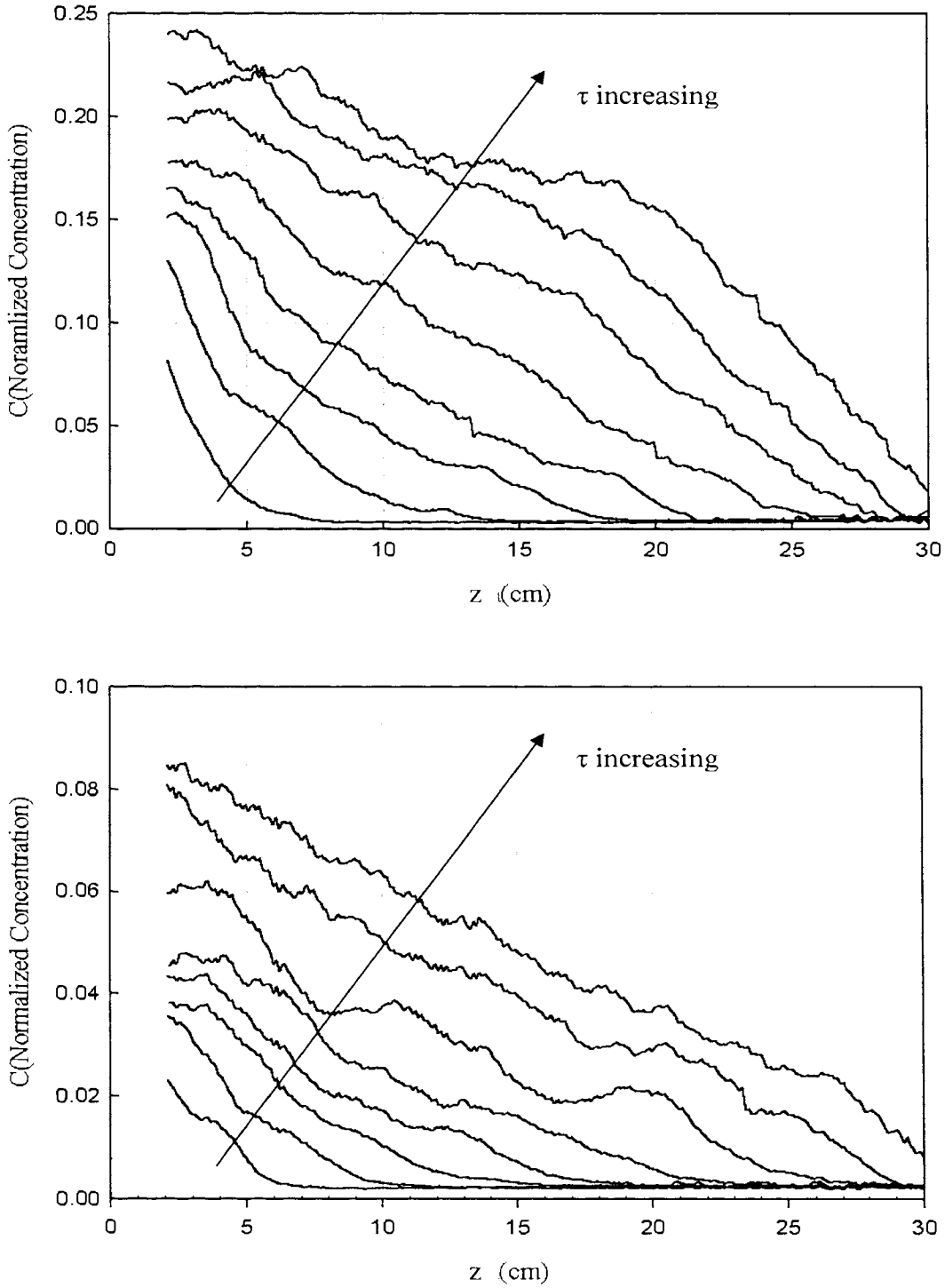

Figure 4.11 Evolution of planar averaged concentration profiles for τ ranging from 0.25 to 2 at an interval of 0.25 for different pH combinations (pH_I=11.5 in all the cases).

c.

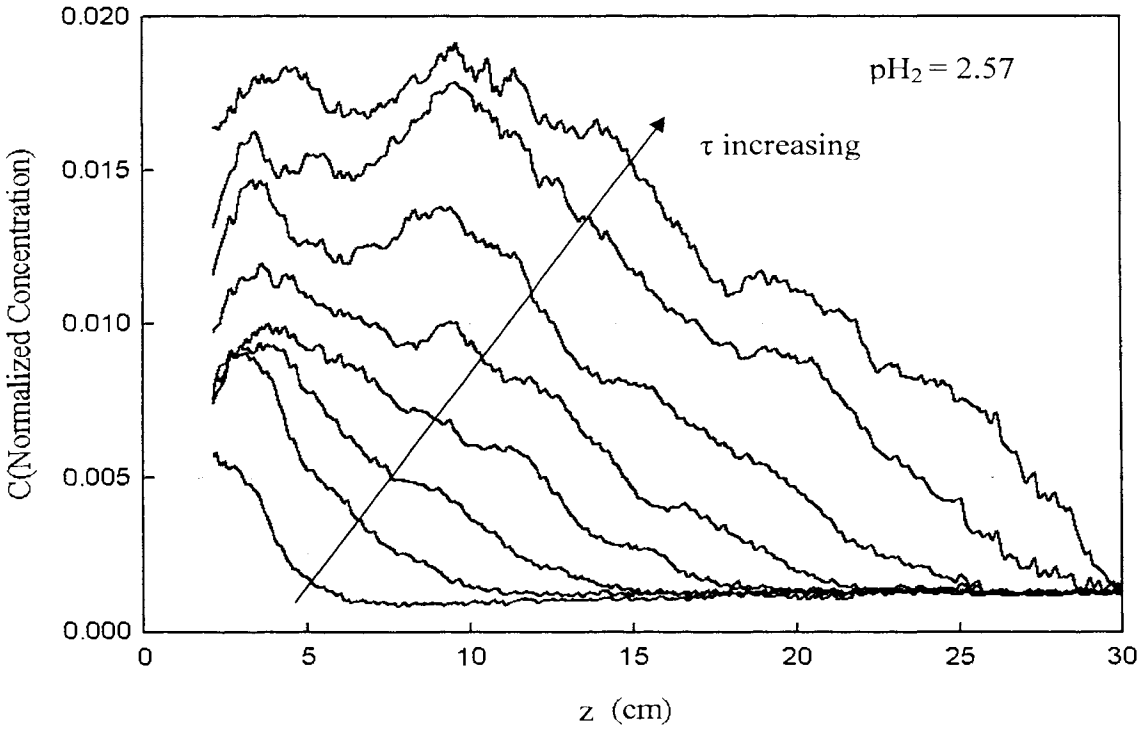

Figure 4.11 Evolution of planar averaged concentration profiles for τ ranging from 0.25 to 2 at an interval of 0.25 for different pH combinations (pH_1=11.5 in all the cases) (cont.).

Previous researchers have found that the amount of indicator produced is a function of the equivalence ratio φ, which is a measure of balance or excess of reactants. The canonical definition of φ formulated for the cases of shear and jet flows for the reaction involving phenolphthalein as the chemical indicator is given such that:

$$\varphi_{In} = \frac{[In]/[OH^-]}{([In]/[OH^-])_{st}} \tag{4.11}$$

Where the subscript –'st' denotes the stoichiometric ratio (0.5) of reactants (refer Section 3). In the limit φ_{In} approaches 0, the quantity of indicator reaches an asymptotic value and is a function of the degree of molecular mixing between the two fluids[62, 64-65]. The above definition however neglects the neutralization reaction as the two streams mix and is accurate only for the limiting case when φ_{In} approaches 0. It fails to explain the

reduced quantity of indicator formed in the cases when the acidity of the lighter stream of fluid is increased. To account for this we adopt the definition of equivalence ratio given by Mueschke et al.*[9]* for the current work given by:

$$\varphi_n = \frac{\left[H^+\right]/\left[OH^-\right]}{\left(\left[H^+\right]/\left[OH^-\right]\right)_{st}} \tag{4.12}$$

where the stoichiometric ratio of the reactants (denominator) for neutralization is 1. The neutralization equivalence ratio, φ_n controls the volume fractions of the reactants that must mix in order to achieve the pH necessary for the indicator to change color. As φ_n approaches zero an excess of OH^- ions exist in the top stream and only a small fraction of the heavy fluid must mix with the lighter fluid in order to produce the necessary color change. On the other hand when φ_n approaches a large values, there is an excess of H^+ ions and so a large quantity of the heavy fluid must mix with the lighter fluid to bring about the necessary change in the pH of the mixture for a color change in the indicator. For pH combinations of pH_2=7 and pH_1=11.5, the resulting φ_n value is $3.2 \times 10^{-5} << 1$ and with an indicator concentration of the order of 10^{-6}, the combination should be insensitive to the equivalence ratio and therefore representative of degree of molecular mixing.

Figure 4.12 presents a comparison of the concentration profiles as observed in the water channel facility at a pH combination of 11.5,7 and 11.5, 2.5. As it can be seen observed the current experiment measures higher concentration values at the lower mixture fraction thresholds indicating an increase amount of entrainment while the concentration measured at higher mixture fraction thresholds, requiring greater mixing have resulted in lower concentration values. Furthermore the water channel experiments have shown a presence of mixture fraction as concentration measurement were recorded for pH combination of 11.5 and 2.03 while there was no indicator detected for this pH combination in the current facility which is consistent in terms of the trend observed from the other pH combinations. Similar to the water channel observations a slight bias in the measurement of the concentration was observed due to the absorption of the light by NaCl that is present on the bubble side. At higher equivalence ratios the flattening of the concentration profiles at the center of the mixing layer is also observed in both the experiments. Also we can see that as the flow attains higher Re_h it can be observed that

the concentration profiles tend to become linear in contrast to an initial parabolic behavior. The most significant difference being the reduced concentration at higher equivalence ratios marking a pronounced decrease in molecular mixing is attributed the change in initial conditions.

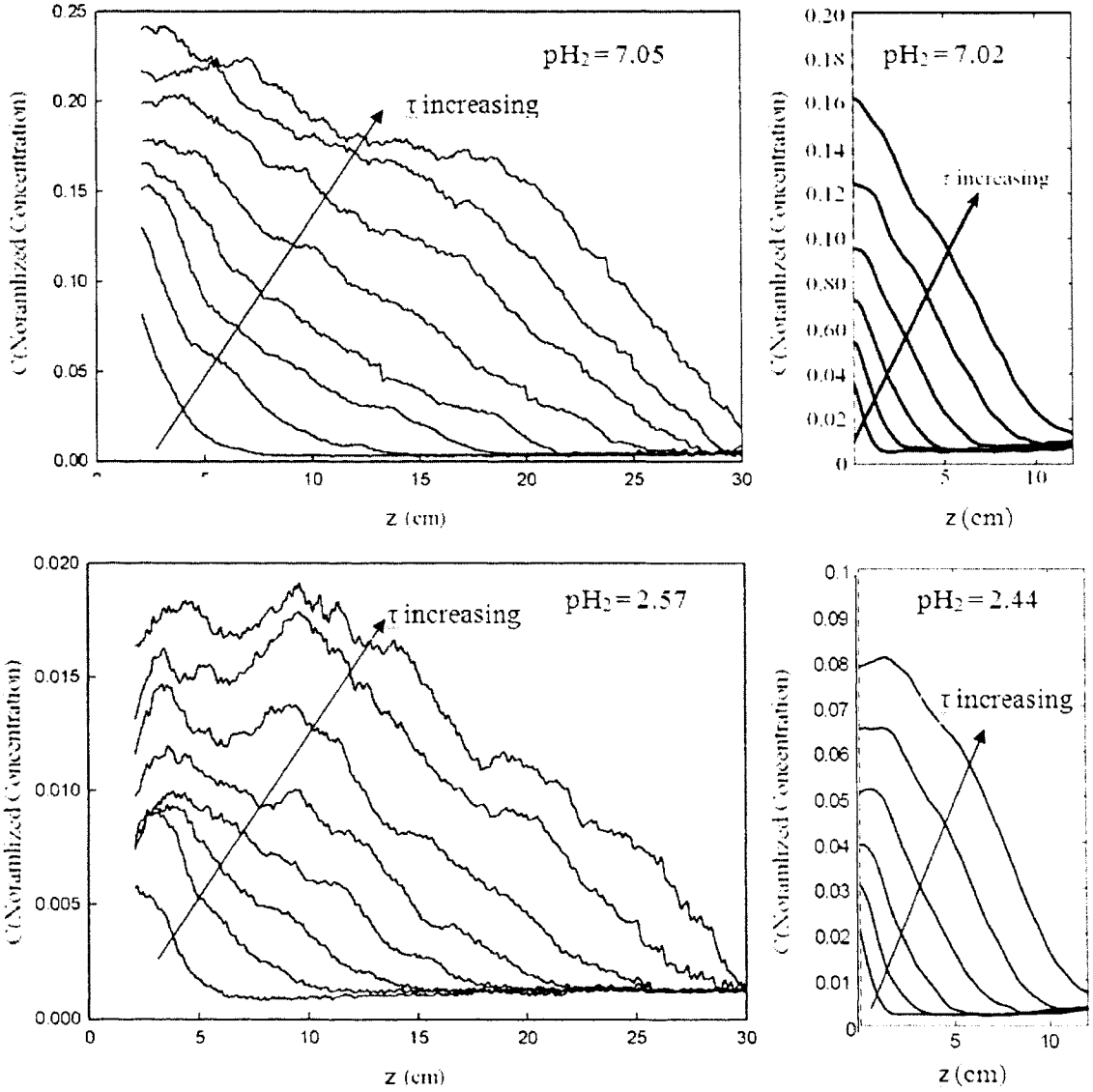

Figure 4.12 Comparison of planar averaged concentration profiles for τ ranging from 0.25 to 2 at an interval of 0.25 for different pH combinations (pH_1=11.5 in all the cases) between the current experiment and the water channel facility[9].

One of the important differences to note between the two experiments is the range of Re to which the mixing layer spawns to in each of the experiments. The non-dimensional time scale does not put this difference in perspective. While in the current experiment the mixing layer attains a Re_h number of ~ 10000, the maximum attainable Re in the water channel is limited to a maximum of ~3000. To put this variation in perspective, the experiments are compared on the Equivalent product thickness which is representative of the fraction of chemical formed in the mixing layer. The equivalent product thickness is defined for an RTI driven mixing layer as [9]:

$$\frac{P}{h} = \frac{1}{h}\int_{h_s}^{h_b} \frac{\left[\overline{In_{IV}}\right]}{[In]_2} dz \tag{4.13}$$

For our investigation in the low A_t, $h_s = h_b = h/2$. The parameter is analogous to P/δ observed in shear layers[62, 65] . To account for the bias induced by salt a correction was applied to account for the absorption by the salt and therefore equation 4.13 becomes:

$$\frac{P}{h} = \frac{1}{h}\left[\int_{h_s}^{h_b} \frac{\left[\overline{In_{IV}}\right]}{[In]_2} dz - \frac{h}{2}\xi\right] \tag{4.14}$$

Where ξ~0.00087 is the span integrated measure of C due to salt that was measured before the experiment started. Figure 4.13 shows the evolution of P/h as a function of the Re_h in the current experiment and the water channel facility. The bubble height was computed using 5%-95% limits on the passive scalar runs and the concentration were taken from the reactive scalar runs and the physical quantities correlated at similar times to compute this integral parameter. It can be observed that the ratio reaches the asymptotic limit of equivalent product thickness observed in shear layers at higher Re. Asymptotic P/h behavior has been observed with shear layers at a Re ~ 8000-10000, however the current investigation does not show such behavior at similar Re even though it attains such a value at corresponding Re_h. A facility with an extended domain would be needed to observe such asymptotic behavior. This trend is also an indicator of RTI driven mixing to be a more effective mixing mechanism in terms of stretching the interfacial contact area between the two fluids. Similar trends in P/h variation at Re_h > 1000 between the two experiments can be observed from the plot adding to the validation of the diagnostic. Though it has been established in shear flows that the amount of colored product formation at high Re is independent of initial conditions[62], the sensitivity of

equivalent product thickness to initial conditions in RTI driven flows is a question yet to be answered. The variation in this parameter observed at early time between the two facilities can be attributed to the effect of initial condition as is true with shear layer and jets.

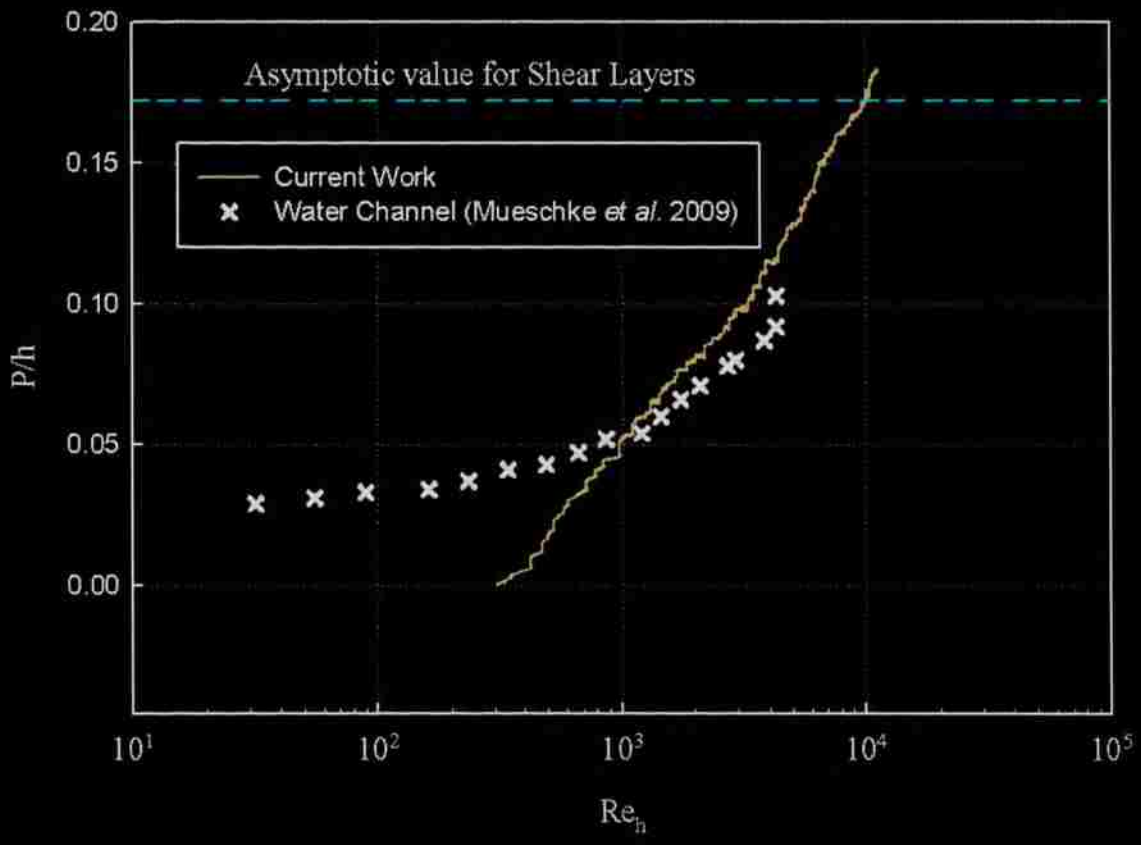

Figure 4.13 Comparison of equivalent product thickness evolution between current investigation and the water channel (pH_1= 11.5 and pH_2= 7).

4.4. MIXING ESTIMATES

The current investigation adopts the technique developed at the water channel facility for relating passive scalar and reactive scalar measurements to fluctuating density statistics and quantifying the molecular mixing parameter at local and global scales[9].

4.4.1. Local Mixing. The definition of local molecular mixing adopted in this case is derived from Danckwerts [78] which is based on the intensity of the segregation parameter. According to this definition molecular mixing is defined by the parameter (θ) is defined by:

$$\theta = \frac{\overline{f_1 f_2}}{\overline{f_1}\,\overline{f_2}} = 1 - \frac{\overline{f_1'^2}}{\overline{f_1}\,\overline{f_2}} \tag{4.15}$$

where $\overline{f_1'^2}$ denotes the Reynolds averaged fluctuation of the heavy fluid volume fraction from the mean which translates to $\overline{f_1'^2} = \overline{\rho'^2}/(\Delta\rho)^2$, and $\Delta\rho = \rho_1 - \rho_2$ [33]. θ is therefore a measure of homogeneity of a mixture such that θ=1 when the two fluids are completely mixed at the molecular level and θ=0 if the mixture is stirred but no diffusive mixing has occurred. Indicator formation can be directly related to the volume fraction variance. A detailed description of the derivation relating the volume fraction variance to the measured concentration profiles is given by Mueschke et al.[9]. The relation is given by:

$$\overline{f_1'^2} = \overline{f}_1\,\overline{f}_2 - \frac{1}{\alpha_{InH}^{\max}} \int_0^1 C(f_2^{50\%})\, df_2^{50\%} \tag{4.16}$$

where the quantity $\alpha_{InH}^{\max}$ is the fraction of maximum dissociation of the indicator and is 0.96 for the current indicator. The quantity $f_2^{50\%}$ is volume fraction of the light fluid in the mixture at a given equivalence ratio at which half the indicator dissociates to its colored form. The quantity $C(f_2^{50\%})$ is concentration of the indicator as measured at the corresponding volume fraction. The integral represented in the right hand side of equation 4.15 may be interpreted as the sum of the chemical product produced at all possible equivalence ratios. Using 4.15 the equation 4.14 can be rewritten as:

$$\theta = \frac{\int_0^1 C(f_2^{50\%})\, df_2^{50\%}}{\alpha_{InH}^{\max}\,\overline{f_1}\,\overline{f_2}} \tag{4.17}$$

The terms on the right hand side of the above equations (4.13 and 4.14) include the mean volume fraction vales which are obtained from the volume fraction profiles that have been estimated using the passive scalar and the mean chemical indicator profiles which have been estimated using the reactive scalars as presented in the previous sections.

Before the estimation of the integral the bounding values of $C(f_2^{50\%})$ at $f_2^{50\%} = 0$ and $f_2^{50\%} = 1$ are important to be considered. If the light fluid carrying the indicator was highly acidic with an infinite H^+ concentration then $f_2^{50\%} = 0$ as there will be no indicator in the dissociated form and consequently $C(f_2^{50\%}) = 0$. If the light fluid was basic all the indicator would exist in the colored form acting as a passive scalar and $C(f_2^{50\%}) = \alpha_{InlV}^{\max} \overline{f_2}$. Thus, these two bounding values are known priori. The intermediate concentration values at the three other equivalence ratios are used from the reactive scalar runs and a quadratic fit[9] to the resulting five data points is used as the concentration variation profile at different equivalent ratios to resolve the integral. We adopt this simplifying assumption as it is impossible to run experiments corresponding to each and every equivalence ratio. 90%-10% volume fraction bounds are adopted as measurements at the mixing layer edges show increased intermittency at lower thresholds.

Figure 4.14(a) and 4.15(a) shows the evolution of the molecular mixing parameter and volume fraction variance based on equations 4.17 and 4.16, respectively. For comparison purposes the corresponding parameters measured from the water channel facility are plotted along side (4.14(b) and 4.15(b)). As obvious from the plots, a decreased value of molecular mixing parameter is observed from the investigation in the current facility. This can be attributed to the difference in the spectral signature of the initial conditions as every other parameter remains the same between the two facilities in terms of the parameters describing the binary fluid combination that quantify the nature if the instability. It is interesting to observe the value of molecular mixing at the tails shows an increased behavior. This may in part be attributed to the vorticity in the initial velocity perturbations posed on removal of the barrier (from the uncovered edges of the barrier) which propagate and strengthen as the mixing front advances. The nature of variation in the molecular mixing parameter at the core of the mixing layer remains between the two investigations and tends to flatten out as the flow evolves.

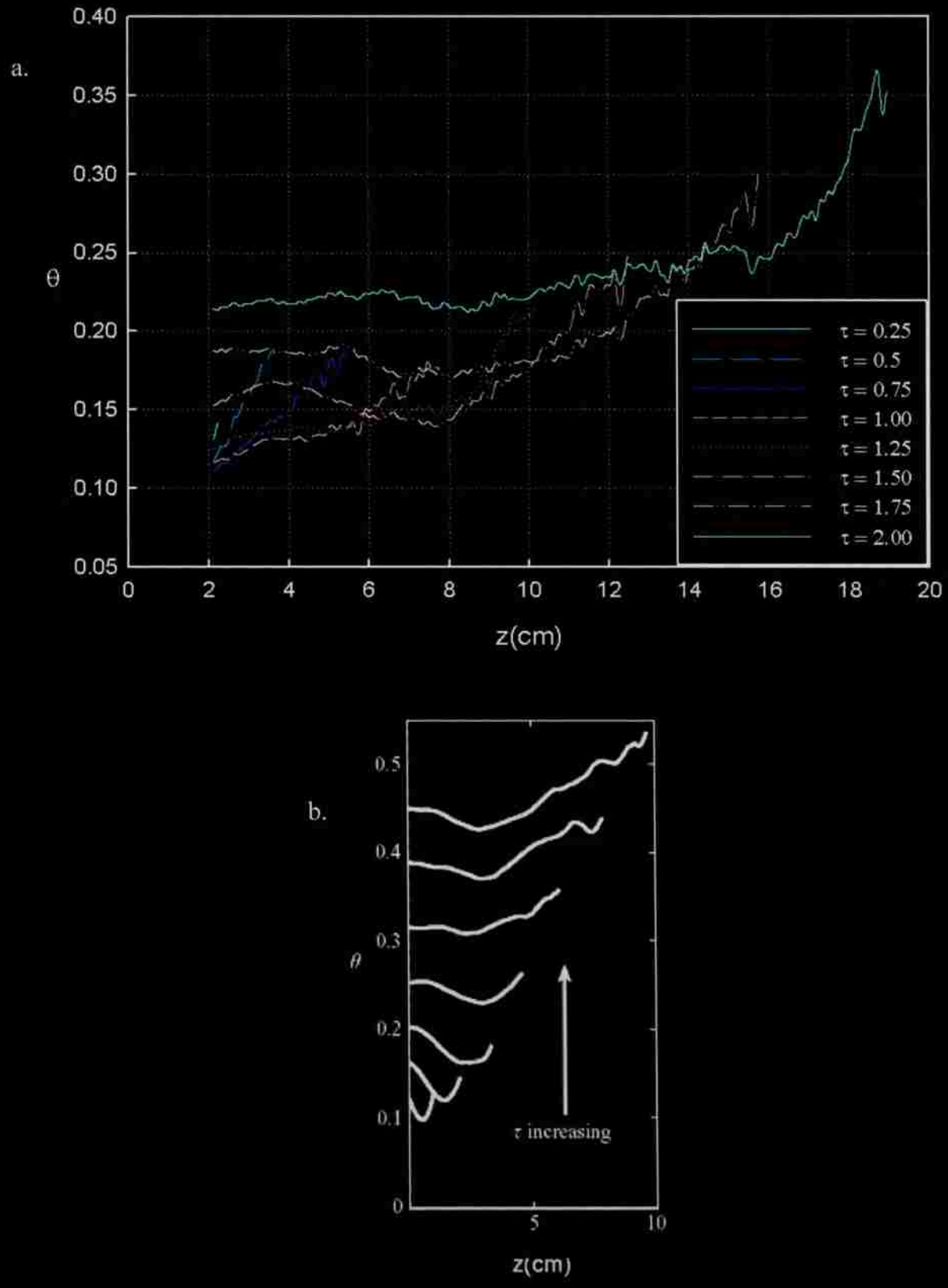

Figure 4.14 Comparison of evolution of molecular mixing parameter from the current investigation (a) and the water channel (b).

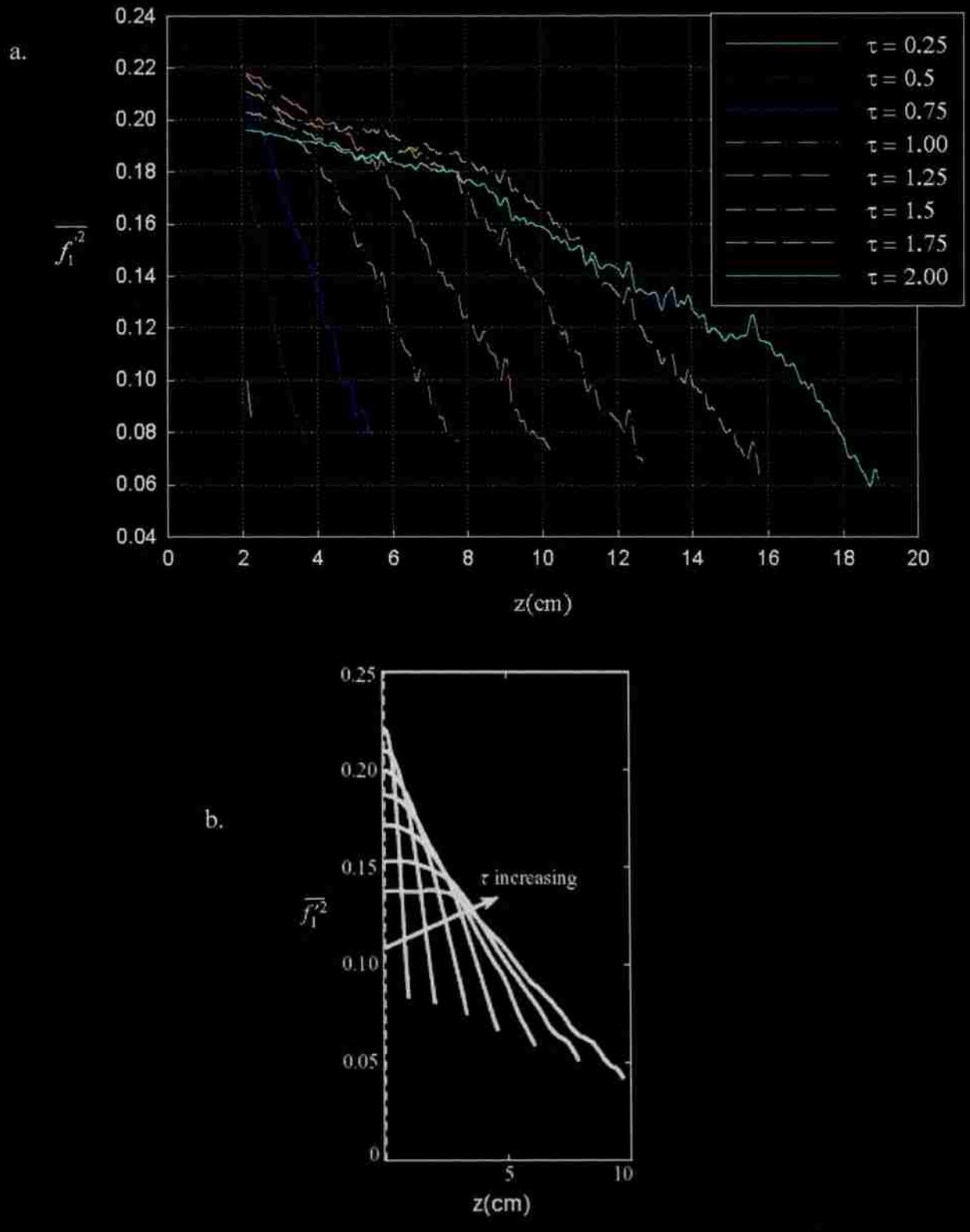

Figure 4.15 Comparison of evolution of volume fraction variance from the current investigation (a) and the water channel (b).

As it can be noticed from the volume fraction estimates that the strength of the volume fraction variance remains comparable to that observed in the water channel while the molecular mixing is significantly low. This may be explained by the following, the entrainment dynamics associated with the dominant large modes on the initial interfacial perturbation continuously feed the mixing layer with the pure fluids and advance the fronts, while segregation (break up) of the entrained fluid occurs as marked the variance in the volume fraction, the flow is dominated by momentum due to the entrainment occurring on the large scales that pushes the fluids before subsequent breakup of the fluid takes place to result in enhanced molecular mixing. Though the exact influence of any single mode cannot be isolated or tracked at present, the corresponding Fermi transitions of the dominant modes would explain the exact reasons for the dynamics observed in the mixing layer. Quantitative assessments of such transitions can be arrived at by performing PLIF measurements across the mixing layer along with selective seeding of initial perturbations.

4.4.2. Global Mixing. Mixing on a global scale is quantified by the global mixing parameter introduced by Youngs[33]. The parameter is given by:

$$\Theta = \int_{h_s}^{h_b} \overline{f_1 f_2} dz \Big/ \int_{h_s}^{h_b} \overline{f_1}\,\overline{f_2} dz \quad = 1 - \left(\int_{h_s}^{h_b} \overline{f_1'^2} dz \Big/ \int_{h_s}^{h_b} \overline{f_1}\,\overline{f_2}\, dz \right) \tag{4.18}$$

At low A_t, $h_s = h_b$ and so the above relation reduces to

$$\Theta = 1 - \int_{0}^{h_b} \overline{f_1'^2} dz \Big/ \int_{0}^{h_b} \overline{f_1}\,\overline{f_2}\, dz \tag{4.19}$$

This parameter operates analogous to the molecular mixing parameter given by θ, a value of 1 indicates perfect mixing and 0 indicates complete segregation. The global mixing parameter was deduced using the above estimated value of volume fraction variance and so was calculated based on 10%-90% volume fraction fiducials. The evolution of the global mixing parameter over the entire mixing layer is presented as a function of τ Figures 4.16 along with values reported from previous investigations.

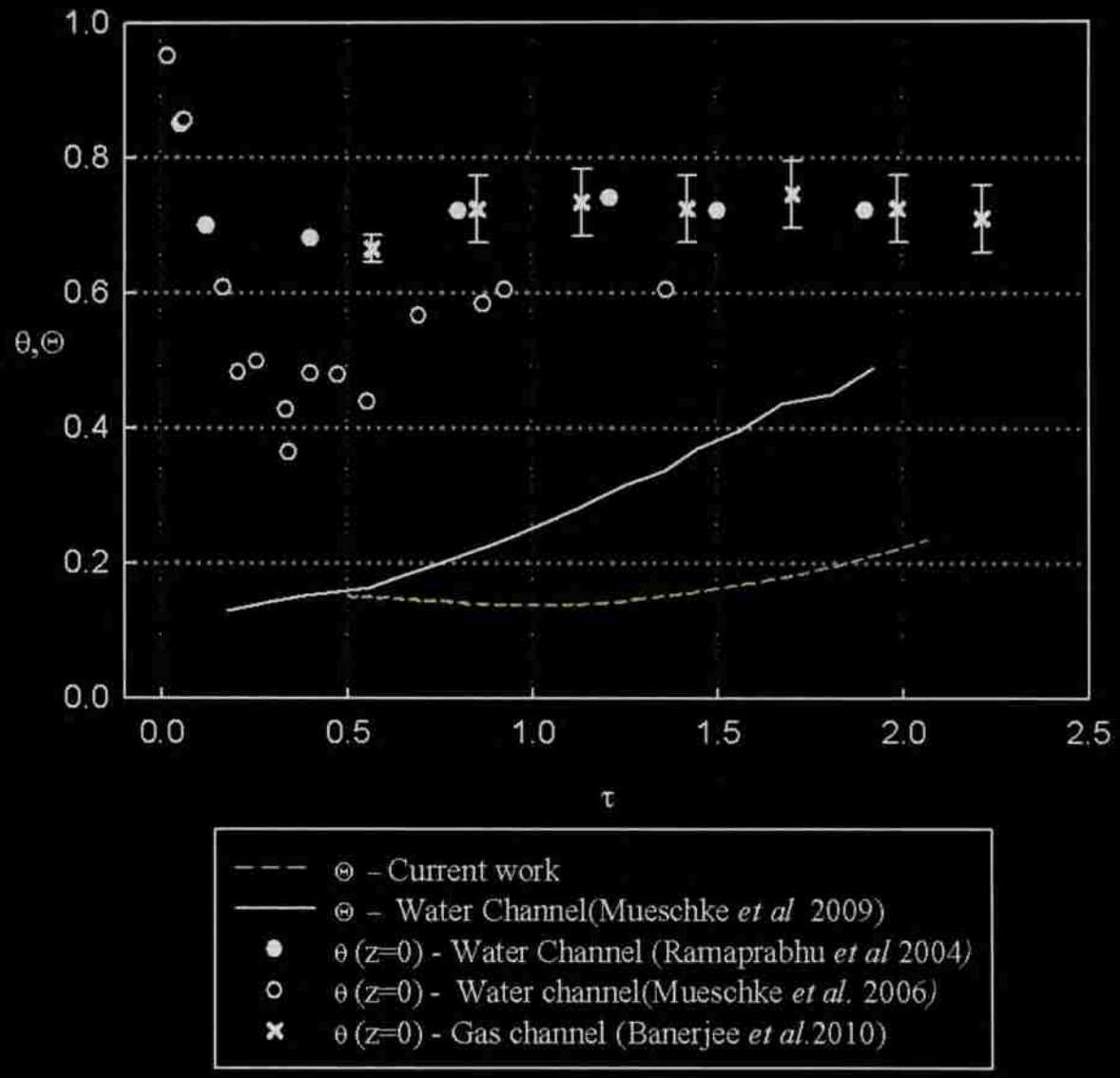

Figure 4.16 Evolution of global mixing parameter as a function of τ along with values reported by previous investigations.

All the values reported here correspond to low-A_t experiment and so form the basis for comparison. In case of point wise measurements made at the center line of the mixing layer of the gas-channel and water channel facilities operating at *Sc* of 1 and 7, respectively it can be seen that the there are two marked stages at times before $\tau \leq 0.4$ and $\tau > 0.4$. As to the behavior of the parameter, it has been attributed [66] that for $\tau \leq 0.4$, the two pure fluids are "stirred" with little molecular mixing and the flow pertains to regimes

of initial exponential growth and onset of the non-linear stabilities where in there is entrainment of the pure fluids without molecular mixing and a lowering of the values is observed. For $\tau > 0.4$, the flow is characterized by the onset of secondary instabilities, Kelvin-Helmholtz in particular, leading to increases interfacial surface area between the fluids and consequently enhanced mixing as marked by the subsequent raise in Θ. As to the values themselves, it has been reported that the values are over estimated due to probe size limitations[9, 66]. The evolution of Θ in the water channel investigation shows a significant lowering of the value in comparison with the value measured from point wise measurements made at the center plane using thermo couples. The trend has been attributed to the difference in the *Sc* at which the two measurements were operating, the nature of the measurement (one being local and the other global) and the over estimation due to resolution limitation of the probe[9]. The trend of increased mixing has been observed about $\tau \approx 0.5$ without the initial decrease in the water channel facility using the reactive flow technique and span wise measurements. In the current experiment we see an increase in Θ at $\tau \approx 1.25$. The value of the parameter decreases slightly till this time and increases subsequently. Significantly reduced values as compared with the previous investigations support the fact that there is a strong segregation(stirring)(as observed from the volume fraction variance) with little molecular mixing (as observed from the local values of mixing) suggesting that a change in the molecular mixing dynamics with the nature of the initial perturbation spectrum.

To better understand the transition in mixing, Figure 4.17 presents a plot of the mixing parameters observed previously as a function of the Re_h of the mixing layer. It can be observed from the plot that the flow becomes self-similar with a constant value of θ for the point wise measurements made in the water channel and the gas channel facilities at a Re_h~2000 and so the non-linear mixing transition was attributed to $100 < Re_h < 2000$ regime. However the water channel investigation using the reacting flows technique has not seen a asymptotic value for a flow $Re_h \sim 3000$ and so could not ascribe the range for the mixing transition but however pointed out that such an asymptotic value maybe arrived at a Re_h~8000-10000 if the mixing mechanism is similar to that of shear layers at the limit. The current investigation reports values which are much lesser than the values of the Θ observed in the water channel by the same diagnostic and at the same A_t even

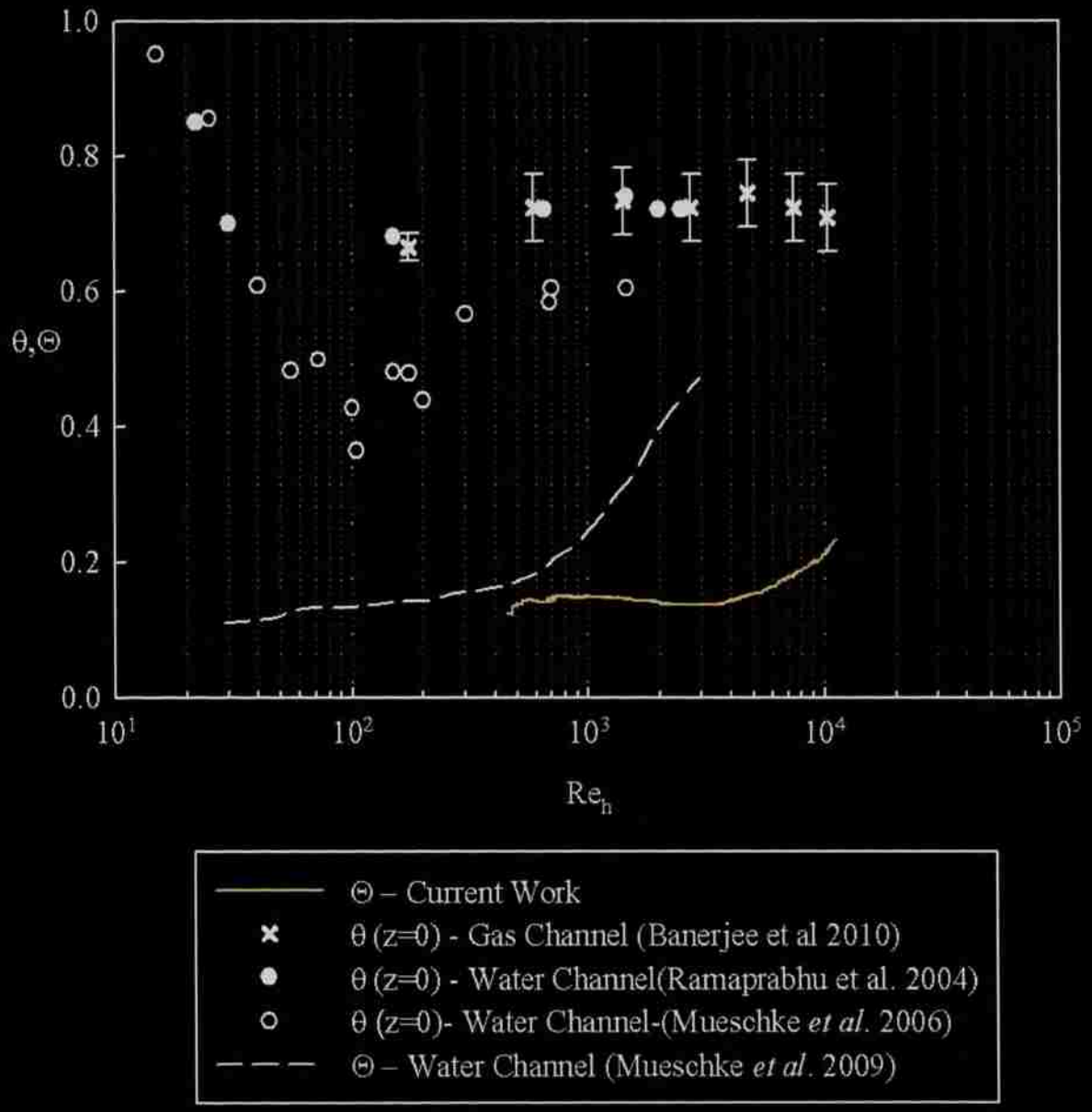

Figure 4.17 Evolution of global mixing parameter as a function of Re_h along with values reported by previous investigations.

though the flow has spawned to a $Re_h \sim 10000$, moreover the trend in the mixing as similar to that observed by other investigations where in there is a slight increase in the mixing metric has shifted to $Re_h \sim 3000$. It is difficult to conclude as to whether the trend of increased Θ is monotonic while there are no pointers towards asymptotic behavior of

Θ even at the high Re_h. In comparison to shear layers, which asymptote on their mixing characteristics at Re_h~8000-10000 irrespective of their initial conditions, a pronounced sensitivity to the initial conditions can be observed in case of mixing by RTI.

The plots a slight increase in the global mixing parameter can be observed at higher Re_h and τ suggesting enhanced mixing observed across the mixing layer. The implications of such an increase can be attributed to transition in the flow dynamics shifting towards molecular mixing over the dominance of segregation. Little can be inferred about the mixing transition as the global mixing parameter does not show any asymptotic behavior as is observed in Gas-channel and water-channel point wise measurements at the center plane. This is in conformance with the P/h measurements which do not show asymptotic behavior at high Re_h. The results point at a qualitative inference that the low wave number loading of energy in the initial density perturbation spectrum as a possible mechanism in delaying the mixing transition.

5. CONCLUSIONS AND FUTURE WORK

5.1. SUMMARY

The primary objective of the current investigation was to study the effect of initial conditions on molecular mixing in a high Schmidt number RTI driven flow in the interests of developing predictive models that characterize the flow accurately. Due to limitations in the current computational capabilities in resolving the Batchelor scales, which is necessary to estimate molecular mixing, the current investigation has adopted an experimental approach to attain the objective. Non-intrusive optical diagnostic techniques involving back-lit imaging were established to observe the growth of flow. The imaging was calibrated against a passive and a reactive scalar to quantify volume fraction and mixture fraction evolution as the flow proceeds. A detailed standard operating procedure to run the experiment with acceptable repeatability was developed to ensure an RTI driven mixing layer in the test section. MATLAB scripts necessary for translating the information in the imagery into flow defining metrics were developed. Macroscopic parameters characterizing growth on the large scales were ascertained from the passive scalar runs and reported. The initial conditions of the flow were modeled from the passive scalar runs and verified using large eddy simulation by comparison on the macroscopic metrics. The reactive scalar runs and the passive scalar runs were coupled to quantify molecular mixing detail in the flow. The molecular mixing detail was then compared with respect to similar measurements made in the water channel facility at Texan A&M and the effect of initial conditions is discussed.

Details of the current investigation are summarized as below:

- An experimental facility, measuring 30.5cm × 30.5cm × 63.5cm in x,y and z dimensions, enabling the study of evolution of high Sc RTI driven mixing layer to a $Re_h \sim 10000$ and a late time of $\tau = 2$ is designed and established.
- Non-intrusive, backlit imaging techniques using a Metal halide Arc lamp and a CMOS based high speed camera with a temporal resolution of (1/60 sec) and a spatial resolution of ~0.9 mm for obtaining span averaged measurements of tracers over the entire test section have been established.

- Diagnostics developed have been calibrated for the measurement of span integrated concentrations of a passive scalar (Nigrosine) and a reactive scalar (Phenolphthalein). The range of linearity in the correlation between the amount of light absorbed as recorded by the CMOS and the indicator concentration has been isolated and the molar absorptivity coefficients for the passive and reactive scalars were established as 5776.9(l/Mol-cm) and 29704 (l/Mol-cm).
- The uncertainty associated with the flow metrics were quantified using Kline and McClintock and tabulated.
- Experiments were conducted with the passive scalar to and volume fraction evolution of the heavy fluid related by the Nigrosine concentration was used to quantify mixing layer growth metrics. α_b of 0.085 is reported from the current investigations using the Ristorcelli and Clark approach.
- Quantitative and qualitative measurements on the wake observed with the passive scalar suggested a dominant 2-D perturbation at the interface. Based on a wave counting methodology The passive scalar runs were used to quantify the most dominant modes and their amplitudes in the ensemble of experiments. The dominant modes were modeled around modes 4-6 with a perturbation rms of 0.007.
- The accuracy of the modeled initial conditions was verified using LES simulations on the value of α_b. The consistency was also cross verified with the modeled perturbation in the water channel facility and the difference in the initial condition signature was established.
- Reactive scalar experiments were conducted and a comparison of the concentration profiles exhibited at the two facilities is compared on the magnitude and behavior. A decrease indicator concentration is observed with the reactive scalar at higher equivalence ratios suggesting decreased molecular mixing.
- The equivalent product thickness evolution is studied and similar scaling at $Re_h > 1000$ is observed. The equivalent product thickness grows beyond the asymptotic value attained by shear jets at $Re \sim 8000\text{-}10000$ and is continues to show growing trends.

- The passive scalar and reactive scalar runs are used to quantify the evolution of molecular mixing and volume fraction variance in the mixing layer. A decreased molecular mixing is exhibited in the current investigation while the variance remains at a similar strength as in the water channel facility. This suggests strong segregation but decreased molecular mixing attributed to the entrainment dynamics resulting from the initial conditions.
- Estimates of global mixing parameter evolution are quantified. A decreased mixing is observed in the current investigation in comparison with measurements made at the water channel and gas-channel investigations. The behavior of the global mixing parameter has been analyzed and hints at a possible delay in mixing transitions as a result of the initial conditions.

5.2. FUTURE WORK

The current experimental investigation was performed using a manually operated flat plate. The diagnostics developed were based leveraging on span integrated measurements over the test section. However, a detailed investigation of the effect of initial conditions with implications towards development of turbulent models that capture the influence of initial condition signature accurately would require that the Fermi transition of specific modes be studied in detail. In this direction the following course for future work is suggested.

- In order to ensure a greater degree of repeatability and to eliminate the uncertainty associated with manual operation of the barrier an automated withdrawal mechanism is suggested.
- To study mode transition of specific wave numbers it is required that controlled initial conditions be imparted at the interface. This can be achieved by imposing a 2D perturbation of the requisite wavelength on top of the perturbation that is imparted by pulling the barrier. This can be brought about by imposing the additional perturbation though the physical shape of the barrier. Figure 5.1 depicts a pictorial representation of the above concept.

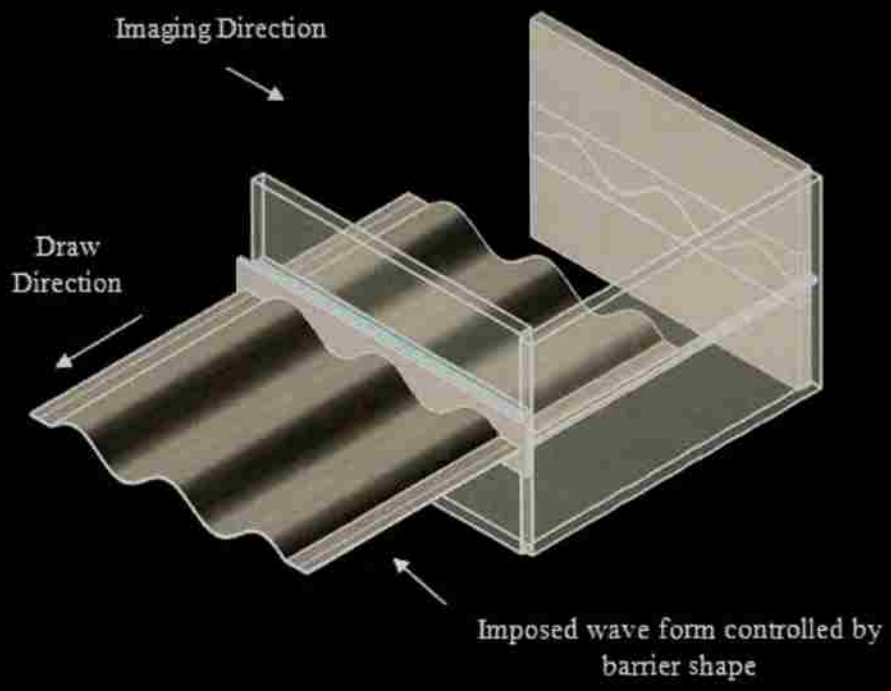

Figure 5.1 Pictorial representation of the methodology for controlled variations.

- In the interests of completely characterizing the initial conditions it is important to quantify the initial velocity perturbations. A particle image velocimetry study of the initial perturbations is suggested.
- In-order to accurately quantify the effect of particular modes on subsequent evolution of the density field, planar images quantifying the evolution of the density field are required to study Fermi-transitions. PLIF or LIF techniques are suggested for the same.
- To explicitly study the effect of initial conditions at low Schmidt numbers, the current facility can be modified to study gas phase flows.

APPENDIX A.
WAVELENGTH ESTIMATION FROM PASSIVE SCALAR RUNS

Withdrawing the barrier separating heavy and light fluids imposes a perturbation at the interface of the two fluids. The spatial structure of the perturbation is a result of anisotropic fluid adjustment in the void (due to finite volume removal) as the barrier is withdrawn, viscous boundary layers emanating from the tip and exposed strips of the barrier (where there is relative motion) and a Bickley jet (due to flexibility in the barrier). During the initial phase of removal, (till about a third of the domain length) the spatial structure of the perturbation is dominated by in surge of the heavy fluid (due to liquid at pressure being forced through a small area to fill the void) into the light and consequent movement of blobs of pure lighter fluid moving into the heavier (to satisfy mass conservation). During this phase of withdrawal, large and distinct blobs of the heavy fluid and light fluid can be observed moving across the interface.

The next phase of barrier removal (the next third of the domain length) where the effect of adjustment of fluid does not result in an insurge of heavy fluid (due to presence of sizeable area for fluid adjustment in the void), the effect of Bickley Jet and the viscous layers dictate the spatial structure of the perturbation. Numerous small, interpenetrating fingers of heavy and light fluid can be observed in the wake of the barrier.

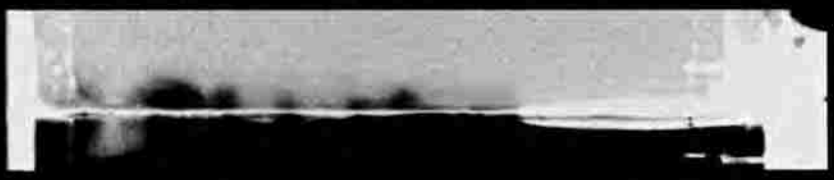

The final phase of removal of the barrier is when the Bickley jet is weak, the effect of fluid down draft is small and viscous boundary layers dominate the spatial structure. Since the effect of the viscous boundary is same on both the top and bottom layers of the liquid no distinct, sizeable structures can be observed at the tail of the barrier.

Counting Principle:

The counting principle adopted for the first phase is straight forward as each pocket of pure fluid continues to grow into a structure; each pair of adjacent pure fluid blobs is treated as a wave and counted.

During the second phase the interleaving finger like structures do not continue to grow with the momentum they were formed but instead slow down after the barrier leaves rearrange and then evolve. During the period of slow down and before subsequent evolution, there is a merger of structures resulting from diffusion of very thin pockets of either fluid due to strong gradients between the pure fluids. Consequent well formed structures continue to evolve and so at this juncture the resulting pair of adjacent pure fluid fingers are treated as a wave and counted.

The third phase of withdrawal leaves no visible, distinct structure that can be marked to be dominating subsequent growth in that region and so this region is divided on the basis of the total number of dominant bubble and spike pairs emanating from this region at a later time. Each bubble-spike pair is counted as a wave

The length of the domain is then divided by the total count obtained by the procedure above.

Example Calculation:

Consider the data from the run on June 03 2010, we shall proceed with our analysis as prescribed in the preceding paragraph.

Phase -1:

From the snap shot below we can see that there are 3 dominant spikes and two bubbles that can be seen. So the total number of waves is counted as 2.5

Phase -2

Below is a snap shot of the fluid interface at the instant the barrier has moved past it. It can be seen that there are a large number of interleaving pure fluid "fingers ". Below the figure is the same snap shot with the alternating structures marked.

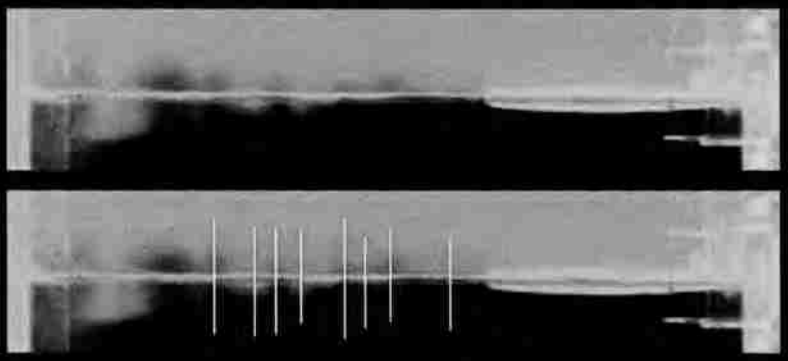

It can be seen that there are eight pockets of pure fluid as marked. Now if we look at the same region at a later time (At the instant the barrier is completely removed) as shown in the snap shot below, we can see that some of the structures have disappeared and in the region is dominated by stronger structures (greater width at the structure base) as marked and so the total number of "fingers" has now reduced to five.

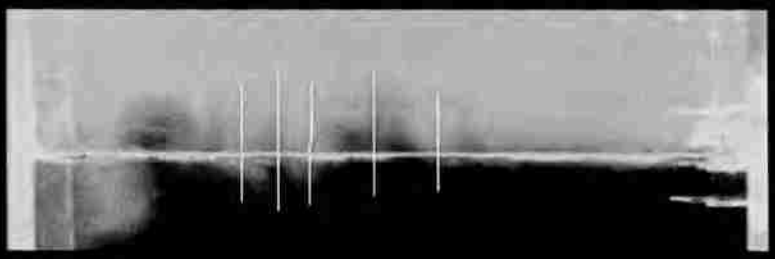

In conjunction to the question that might arise as to how a particular structure was eliminated, the rationale used here was the intensity levels at the base of the structure. For example, if the intensity at the base of the light fluid (white) has darkened, it implies that diffusion from the surrounding heavy fluid has changed the density in comparison to the mass efflux pumped into that structure from its base and so it is unlikely that the structure would rise up than be further contaminated by the heavy fluid and coalesce with the surrounding heavy fluid. This can be observed with regard to the first structure and the vice-versa (whitening of the dark fluid) with the fifth structure of the earlier snap shot(counting starts from left to right).

From the figure the total number of pure fluid structures pertaining to the phase-2 region is 5 and so the number waves is 2.5.

Phase-3:

The figure below relates to initial configuration of phase-3 region. As it can be seen there are no distinguishable structures.

Below is a snap shot from a later time. Alternating, dominant structures of pure fluid have been marked using the same logic as used for determination incase of phase 2. As it can be observed there are two structures and so counted as one wave.

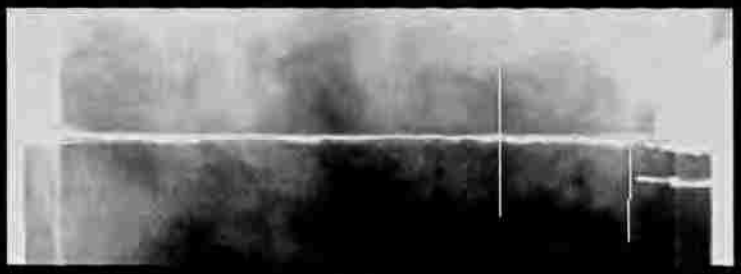

The total number of waves is 6 (summing up regions from phase 1 ,2 and 3).
The length of the domain is 30.5 cm and so the wave length of the perturbation by this methodology (from this run) is 5.08 cm.

Caution:-

Care should be taken that the same structure is not counted twice .The first structure counted for each phase of withdrawal is supposed to be the counterpart of the structure counted at the end of the previous phase.

Need for averaging across multiple runs:

As it can be observed that the wavelength of the waves counted across the domain length is not the same but are treated as a unit of the count. Secondly, one of the factors that determine the strength of the Bickley Jet and that of the viscous boundary layer is the rate at which the barrier is withdrawn. Variations in the rate at which the barrier is withdrawn (typically 2.5 – 3.5 seconds) might result in a change in the way these two mechanisms operate resulting in a change in the nature of the initial perturbation. An averaging principle is necessary to mitigate the bias induced into the calculation by the above mentioned effects.

The averaging principle adopted in this body of work averages the wavelength calculated by the above procedure across several runs.

APPENDIX B.
SCRIPTS FOR IMAGE ANALYSIS

FUNCTION: IMPR_VOLFRAC – Image processing routine for converting data from Nigrosine runs to volume fraction data.

```
function
impr_volfrac(fname,stseq,enseq,num,st1,st2,wid,hit,e1,f1,g1,h1,...
e2,f2,g2,h2,frame_rate,uid,mac)
format long;
%%%%%%%%%%%%%%%%%%%%%%%%%%%%%%%%%%%%%%%%%%%%%%%%%%%%%%%%%%%%
%fname ->Name of the first file in the sequence
%stseq -> Start position of the sequence number
%enseq -> End position of the sequence number
%num -> Number of files to process
%st1,2 --> Starting point co-ordinates of the focus plane
%wid -> width of the focus plane in pixels
%hit -> Height of the focus plane in pixels
%e,f,g,h -> Handles for the crop function suff 1 for top half, suff -2
for
%bottom
%uid -> Unique Id for mat file generation
%mac -> Molar absorptivity coefficent
%%%%%%%%%%%%%%%%%%%%%%%%%%%%%%%%%%%%%%%%%%%%%%%%%%%%%%%%%%%%
base = 'base001.png'; % Hard-Coded base file name
L_dom = 30.5; %Hard coded width of domain in cm
H_dom = 63.5; %Hard coded the height of the domain in cm
prefix1 = 'top'; %Hardcoded prefix for top images
prefix2 = 'bot'; % Hardcoded prefix for bottom images
A = 7.5e-4; %Atwood number
g = 9.81; % Acceleration due to gravity
%Generate result directory
Cur_Dir = pwd;
delim  = getenv('os');
temp = size(delim);
if temp(2)>6
    if (lower(delim(1:7)) == 'windows')
        delim = '\';
    end
else
    delim = '/';
end
temp = size(Cur_Dir);
for (i=temp(2):-1:1)
    if (Cur_Dir(i) == delim)
        Cur_Dir = cat(2,Cur_Dir(1:i),'result ',uid);
        j = cat(2,'mkdir ',Cur_Dir);
        op_code = system(j);
        break;
    end
end
%%%%%%%%%%%%%%%%%%%%%%%%%%%%%%%%%%%%%%%%%%%%%%%%%%%%%%%%%%%%
%Crop Images as per the specified bounds
crop_images1(fname,stseq,enseq,num,e1,f1,g1,h1,prefix1);
crop_images1(fname,stseq,enseq,num,e2,f2,g2,h2,prefix2);
%Crop Base images as per the specified bounds
crop_images1(base,5,8,1,e1,f1,g1,h1,prefix1);
crop_images1(base,5,8,1,e2,f2,g2,h2,prefix2);
%Scaling the pixel range to actual dimensions
```

```
dh = H_dom/hit; %Vertical resolution
dw = L_dom/wid; %Horizontal resolution
 % Determine the Origin co-ordinates of the domain on the barrier plane
 Orx = st1;
 Ory = st2 + (hit*33/63.5); % Ratio denotes the actual location of
origin inrelation to he height of the domain from top
 %Determine the Initial ht from which subsequnt growth is being
calculated
 in_ht_top = (Ory -(f1+h1))*dh;
 in_ht_bot = -((f2 - Ory)*dh);
 %Generation of z matrix i.e, z for each pixel
 z_top(h1+1) = 0;
 z_bot(h2+1) = 0;
  for (i=h1+1:-1:1)
     z_top(i) = in_ht_top+(i-1)*dh;
 end
 for (i=1:h2+1)
     z_bot(i) = in_ht_bot + -((i-1)*dh);
 end
 hold on;
%Caluclation of Volume fraction for the top half
fname_top = cat(2,prefix1,fname);
fname_base = cat(2,prefix1,base);
b = imread(fname_base);
a = imread(fname_top);
% Get the Max Concentration Value Assuming the die is mixed in the top
    sz = size(b);
%  Convert the matrix to double
    a = cast(a,'double');
%Apply Image correction
  for (p=1:sz(1))
      for (q=1:sz(2))
          a(p,q) = a(p,q)*I_0/b(p,q);
      end
  end
  %

    b = cast(b,'double');
%
    Base_Rat = 0.0;
    for (i = 1:sz(1))
        for (j = 1:sz(2))
        Base_Rat = Base_Rat + (-log(a(i,j)/b(i,j)));
        end
    end
    Base_Rat = Base_Rat/(sz(1)*sz(2));
%
    f(sz(1),sz(2)) = 0;  %Initalize the volume fraction matrix
    f_avg(num,sz(1)) = 0;  %Initialize the Average volume fraction
matrix
    posit_mat_top(num,sz(2))=0; %Initalize the position recorder matrix
for 95% bounds
for (i=1:num-1)
%Change file name to point to the next file
   l = fname_top(stseq+length(prefix1):enseq+length(prefix1));
   l1 = str2num(l) + 1;
   l = num2str(l1);
```

```
   sz1 = size(l);
   fname_top(enseq-sz1(2)+1+length(prefix1):enseq+length(prefix1)) =
l(1:sz1(2));
  %
  a = imread(fname_top);
  a = cast(a,'double');
  %
  for (j = 1:sz(2))
      flag = 0;
     for (k = 1:(sz(1)))
 %Generate the Volume fraction Matrix
   f(k,j) = -log(a(k,j)/b(k,j))/Base_Rat;
 %Adjustment for back ground intensity fluctuations
  if ((f(k,j)>1) ||(f(k,j)<0))
      if (f(k,j)>1)
          f(k,j) = 1;
      else
          f(k,j) = 0;
      end
  end
  %
   %Marker Logic on the image
%     if ((flag<5)&&(f(k,j)<0.95))
%         flag = flag + 1;
%         if flag > 4
%          posit_mat_top(i,j) = k-4;
%          a(k-2,j) = 255;
%         end
%     end
      end
  end
%Populate Average Volume fraction matrix
 for(count=1:sz(1))
     f_avg(i,count)= mean(f(sz(1)-count+1,:),2);
 end
end
hold on;
%%%For Integral Mix width
for (i=1:num-1)
    IMW = 0;
     for (j=1:sz(1))
        %if (f_avg <= 1)
         IMW = IMW + (f_avg(i,j)*(1-f_avg(i,j))*dh);
        %end
     end
     IMW_MAT1(i) = 6*IMW;
     TAU1(i) = (i/frame_rate)*(A*g*100/H_dom)^0.5;
end
%%%%For h vs Aqtsq
for (i=1:num-1)
    for (count=1:sz(1))
        if (f_avg(i,count) < 0.95)
            control_mat_bub(i) = count;
        end

    end
end
```

```
% for (i=1:num-1)
%     if (control_mat_bub(i)>1)
%         XX(i) = A*g*(i/frame_rate)^2;
%         YY(i)= z_top(control_mat_bub(i));
%     end
% end
% plot(XX,YY)
%save buuble data variables
f_avg_bub = f_avg;
mfname = ' ';
mfname = cat(2,Cur_Dir(1,:),delim,'Data_bubble.mat');
save(mfname,'f_avg_bub','IMW_MAT1','TAU1','control_mat_bub','z_top');
%Calculation of volume fraction for the bottom half
fname_bot = cat(2,prefix2,fname);
fname_base = cat(2,prefix2,base);
b = imread(fname_base);
sz = size(b);
%
f(sz(1),sz(2)) = 0;  %Initalize the volume fraction matrix
f_avg(num,sz(1)) = 0;  %Initialize the Average volume fraction matrix
posit_mat_bot(num,sz(2))=0; %Initalize the position recorder matrix for
5% bounds
%Convert base image to double
b = cast(b,'double');
%
for (i=1:num)
  %
  a = imread(fname_bot);
  a = cast(a,'double');
  %
  for (j = 1:sz(2))
      flag = 0;
     for (k = 1:(sz(1)))
 %Generate the Volume fraction Matrix
   f(k,j) = -log(a(k,j)/b(k,j))/Base_Rat;
   %Adjustment for back ground intensity fluctuations
  if ((f(k,j)>1) ||(f(k,j)<0))
      if (f(k,j)>1)
          f(k,j) = 1;
      else
          f(k,j) = 0;
      end
  end
  %
   %Marker Logic
%     if ((flag<5)&&(f(k,j)<0.05))
%         flag = flag + 1;
%         if flag > 4
%          posit_mat_bot(i,j) = k-4;
%          a(k-2,j) = 0;
%         end
%     end
     end
  end
%Populate Average Volume fraction matrix
 for(count=1:sz(1))
     f_avg(i,count)= mean(f(count,:),2);
```

```
 end
 %Change file name to point to the next file
   l = fname_bot(stseq+length(prefix2):enseq+length(prefix2));
   l1 = str2num(l) + 1;
   l = num2str(l1);
   sz1 = size(l);
   fname_bot(enseq-sz1(2)+1+length(prefix2):enseq+length(prefix2)) =
l(1:sz1(2));
 %
end
%Integral mix width of the spike
for (i=2:num)
    IMW = 0;
     for (j=1:sz(1))
        %if (f_avg <= 1)
         IMW = IMW + (f_avg(i,j)*(1-f_avg(i,j))*dh);
        %end
     end
     IMW_MAT2(i) = 6*IMW;
     TAU2(i) = (i/frame_rate)*(A*g*100/H_dom)^0.5;
end
plot(TAU2,IMW_MAT2)
%%%%For h vs agt^2
for (i=2:num)
    for (count=1:sz(1))
        if (f_avg(i,count) < 0.05)
            control_mat_spike(i) = count;
        end
    end
end
%
%save spike data variables
f_avg_spike = f_avg;
mfname = ' ';
mfname = cat(2,Cur_Dir(1,:),delim,'Data_spike.mat');
save(mfname,'f_avg_spike','IMW_MAT2','TAU2','control_mat_spike','z_bot'
);
%
End
```

FUNCTION: BASEGEN – To generate the time averaged - base image.

```
function basegen(fname,stseq,enseq,num)
a = imread(fname);
sz = size(a);
base(sz(1),sz(2)) = 0;
for (i=1:num)
    a = imread(fname);
    a = cast(a,'double');
    base = base + a;
     % Set variable to read the next file
    l = fname(stseq:enseq);
    l1 = str2num(l) + 1;
```

```
    l = num2str(l1);
    sz1 = size(l);
    fname(enseq-sz1(2)+1:enseq) = l(1:sz1(2));
   %
end
%Average
base  = base/num;
base = cast(base,'uint8');
imwrite(base,'base.png');
end
```

FUNCTION: CROP_IMAGES – To crop a given batch of images as per specified handles

```
function crop_images1( fname,stseq,enseq,num,e,f,g,h,prefix)
%Function to process set of images to crop them as per crop handles
%provided and save them back
%fname - Starting filename, num- Number of files(To average on)
%num - Number of files
%e,f,g,h - Cropping handles
%stseq,enseq - Start and end of the sequece number in the filename
string
 for (j=1:num)
    a = imread(fname);
    a = imcrop(a,[e,f,g,h]); %Crop image as per the handles
    s1 = size(fname);
    s2 = size(prefix);
    fbuff(1:s2(2)) = prefix;
    fbuff(s2(2)+ 1:s2(2)+s1(2)) = fname;
    imwrite(a,fbuff);
 % Set variable to read the next file
    l = fname(stseq:enseq);
    l1 = str2num(l) + 1;
    l = num2str(l1);
    sz1 = size(l);
    fname(enseq-sz1(2)+1:enseq) = l(1:sz1(2));
   %
 end
end
```

FUNCTION – IMPR_CONC - Image processing routine for converting data from Phenol,phthalein runs to volume fraction data.

```
function
impr_conc(fname,stseq,enseq,num,st1,st2,wid,hit,e1,f1,g1,h1,...
e2,f2,g2,h2,frame_rate,uid,mac,C0,fsc)
format long;
%%%%%%%%%%%%%%%%%%%%%%%%%%%%%%%%%%%%%%%%%%%%%%%%%%%%%%%%%%%%
%Subroutine to estimate integrated concentration values
%fname ->Name of the first file in the sequence
%stseq -> Start position of the sequence number
%enseq -> End position of the sequence number
```

```
%num -> Number of files to process
%st1,2 --> Starting point co-ordinates of the focus plane
%wid -> width of the focus plane in pixels
%hit -> Height of the focus plane in pixels
%e,f,g,h -> Handles for the crop function suff 1 for top half, suff -2
for
%bottom
%uid -> Unique Id for mat file generation
%mac -> Molar absorptivity coefficent
%C0 -> Constant on concentration
%fsc -> Free stream concentration
%%%%%%%%%%%%%%%%%%%%%%%%%%%%%%%%%%%%%%%%%%%%%%%%%%%%%%%%
base = 'base001.png'; % Hard-Coded base file name
L_dom = 30.5; %Hard coded width of domain in cm
H_dom = 63.5; %Hard coded the height of the domain in cm
prefix1 = 'top'; %Hardcoded prefix for top images
prefix2 = 'bot'; % Hardcoded prefix for bottom images
A = 7.5e-4; %Atwood number
g = 9.81; % Acceleration due to gravity
%Generate result directory
Cur_Dir = pwd;
delim  = getenv('os');
temp = size(delim);
if temp(2)>6
    if (lower(delim(1:7)) == 'windows')
        delim = '\';
    end
else
    delim = '/';
end
temp = size(Cur_Dir);
for (i=temp(2):-1:1)
    if (Cur_Dir(i) == delim)
        Cur_Dir = cat(2,Cur_Dir(1:i),'result_',uid);
        j = cat(2,'mkdir ',Cur_Dir);
        op_code = system(j);
        break;
    end
end
%%%%%%%%%%%%%%%%%%%%%%%%%%%%%%%%%%%%%%%%%%%%%%%%%%%%%%%%
%Crop Images as per the specified bounds
crop_images1(fname,stseq,enseq,num,e1,f1,g1,h1,prefix1);
crop_images1(fname,stseq,enseq,num,e2,f2,g2,h2,prefix2);
%Crop Base images as per the specified bounds
crop_images1(base,5,8,1,e1,f1,g1,h1,prefix1);
crop_images1(base,5,8,1,e2,f2,g2,h2,prefix2);
%Scaling the pixel range to actual dimensions
dh = H_dom/hit; %Vertical resolution
dw = L_dom/wid; %Horizontal resolution
 % Determine the Origin co-ordinates of the domain on the barrier plane
 Orx = st1;
 Ory = st2 + (hit*33/63.5); % Ratio denotes the actual location of
origin inrelation to he height of the domain from top
 %Determine the Initial ht from which subsequnt growth is being
calculated
 in_ht_top = (Ory -(f1+h1))*dh;
 in_ht_bot = -((f2 - Ory)*dh);
```

```
 %Generation of z matrix i.e, z for each pixel
 z_top(h1+1) = 0;
 z_bot(h2+1) = 0;
  for (i=h1+1:-1:1)
     z_top(i) = in_ht_top+(i-1)*dh;
 end
 for (i=1:h2+1)
     z_bot(i) = in_ht_bot + -((i-1)*dh);
 end
 %hold on;
%Caluclation of Concentration for the top half
fname_top = cat(2,prefix1,fname);
fname_base = cat(2,prefix1,base);
b = imread(fname_base);
% Obtain base intensity for image correction
    sz = size(b);
    Y = imhist(b);
    I_0 = 0;
    temp = 0;
     for Y1 = 130:1:256
         if (Y(Y1)>temp);
             temp = Y(Y1);
             I_0 = Y1-1; %Actual intensity
         end
     end
 %
  b = cast(b,'double'); % Cast base into a double
  conc(sz(1),sz(2)) = 0;  %Initalize the volume fraction matrix
  conc_avg(num,sz(1)) = 0;  %Initialize the Average volume fraction
matrix
  posit_mat_top(num,sz(2))=0; %Initalize the position recorder matrix
for 95% bounds
for (i=1:num)
  a = imread(fname_top);
  a = cast(a,'double');
  %Apply Image correction
  for (p=1:sz(1))
      for (q=1:sz(2))
          a(p,q) = a(p,q)*I_0/b(p,q);
      end
  end
  %
  for (j = 1:sz(2))
      flag = 0;
     for (k = 1:(sz(1)))
 %Generate the Concentration Matrix
   conc(k,j) = ((-log(a(k,j)/I_0)/(mac*30.5*0.96*fsc)));
 %Adjustment for back ground intensity fluctuations
  if ((conc(k,j)>1) ||(conc(k,j)<0))
      if (conc(k,j)>1)
          conc(k,j) = 1;
      else
          conc(k,j) = 0;
      end
  end
  %
   %Marker Logic on the image
```

```
%     if ((flag<5)&&(f(k,j)<0.95))
%         flag = flag + 1;
%         if flag > 4
%          posit_mat_top(i,j) = k-4;
%          a(k-2,j) = 255;
%         end
%     end
      end
  end
%Populate Average Volume fraction matrix
 for(count=1:sz(1))
     conc_avg(i,count)= mean(conc(sz(1)-count+1,:),2);
 end
%Change file name to point to the next file
   l = fname_top(stseq+length(prefix1):enseq+length(prefix1));
   l1 = str2num(l) + 1;
   l = num2str(l1);
   sz1 = size(l);
   fname_top(enseq-sz1(2)+1+length(prefix1):enseq+length(prefix1)) =
l(1:sz1(2));
 %
end
%hold on;
%%%For Integral Mix width
for (i=1:num-1)
    IMW = 0;
     for (j=1:sz(1))
        %if (f_avg <= 1)
         IMW = IMW + (conc_avg(i,j)*dh);
        %end
     end
     IMW_MAT1(i) = IMW;
     TAU1(i) = (i/frame_rate)*(A*g*100/H_dom)^0.5;
end
%%%%For h vs Agtsq
% for (i=1:num-1)
%     for (count=1:sz(1))
%         if (conc_avg(i,count) > 0.05)
%             control_mat_bub(i) = count;
%         end
%
%     end
% end
% for (i=1:num-1)
%     if (control_mat_bub(i)>1)
%         XX(i) = A*g*(i/frame_rate)^2;
%         YY(i)= z_top(control_mat_bub(i));
%     end
% end
% plot(XX,YY)
%save buuble data variables
%hold on;
%plot(z_top,conc_avg);
conc_avg_bub = conc_avg;
mfname = ' ';
mfname = cat(2,Cur_Dir(1,:),delim,'Data_bubble.mat');
save(mfname,'conc_avg_bub','IMW_MAT1','TAU1','z_top');
```

```
%Calculation of concentration for the bottom half
fname_bot = cat(2,prefix2,fname);
fname_base = cat(2,prefix2,base);
b = imread(fname_base);
sz = size(b);
% Obtain base intensity for image correction
    sz = size(b);
    Y = imhist(b);
    I_0 = 0;
    temp = 0;
     for Y1 = 130:1:256
         if (Y(Y1)>temp);
             temp = Y(Y1);
             I_0 = Y1-1; %Actual intensity
         end
     end
%
conc_s(sz(1),sz(2)) = 0;  %Initalize the volume fraction matrix
conc_avg_s(num,sz(1)) = 0;  %Initialize the Average volume fraction
matrix
posit_mat_bot(num,sz(2))=0; %Initalize the position recorder matrix for
5% bounds
%Convert base image to double
b = cast(b,'double');
%
for (i=1:num)
  %
  a = imread(fname_bot);
  a = cast(a,'double');
  %
  %Apply Image correction
  for (p=1:sz(1))
      for (q=1:sz(2))
          a(p,q) = a(p,q)*I_0/b(p,q);
      end
  end
  %
  for (j = 1:sz(2))
     flag = 0;
     for (k = 1:(sz(1)))
 %Generate the Volume fraction Matrix
   conc_s(k,j) = -log(a(k,j)/I_0)/(fsc*mac*0.96*30.5);
   %Adjustment for back ground intensity fluctuations
  if ((conc_s(k,j)>1) ||(conc_s(k,j)<0))
      if (conc_s(k,j)>1)
          conc_s(k,j) = 1;
      else
          conc_s(k,j) = 0;
      end
  end
  %
   %Marker Logic
%     if ((flag<5)&&(f(k,j)<0.05))
%         flag = flag + 1;
%         if flag > 4
%          posit_mat_bot(i,j) = k-4;
%          a(k-2,j) = 0;
```

```
%         end
%     end
      end
  end
%Populate Average Volume fraction matrix
 for(count=1:sz(1))
     conc_avg_s(i,count)= mean(conc_s(count,:),2);
 end
 %Change file name to point to the next file
   l = fname_bot(stseq+length(prefix2):enseq+length(prefix2));
   l1 = str2num(l) + 1;
   l = num2str(l1);
   sz1 = size(l);
   fname_bot(enseq-sz1(2)+1+length(prefix2):enseq+length(prefix2)) =
l(1:sz1(2));
 %
end
%Integral mix width of the spike
for (i=2:num)
    IMW = 0;
     for (j=1:sz(1))
        %if (f_avg <= 1)
         IMW = IMW + (conc_avg_s(i,j)*dh);
        %end
     end
     IMW_MAT2(i) = IMW;
     TAU2(i) = (i/frame_rate)*(A*g*100/H_dom)^0.5;
end
% plot(TAU2,IMW_MAT2)
% %%%For h vs agt^2
% for (i=2:num)
%     for (count=1:sz(1))
%         if (f_avg(i,count) < 0.05)
%             control_mat_spike(i) = count;
%         end
%     end
% end
%
%save spike data variables
conc_avg_spike = conc_avg_s;
mfname = ' ';
mfname = cat(2,Cur_Dir(1,:),delim,'Data_spike.mat');
save(mfname,'conc_avg_spike','IMW_MAT2','TAU2','z_bot');
%
End
```

FUNCTION – TESTINTENSITY - Image processing routine for verifying the uniformity of the background.

```
function testintensity(fname,stseq,enseq,num,e,f,g,h,m,n,y1,y2,x1,x2)
%Function to process set of images to generate intensity plots on
% a m*n grid of lines spaced in the domain.m and n should be > 2
%fname - Starting filename, num- Number of files(To average on)
%e,f,g,h - Cropping handles
%stseq,enseq - Start and end of the sequece number in the filename
string
```

```
%y1,y2,x1,x2 - Extents of the domain along each axis
 for (j=1:num) % parse for all the images
    a = imread(fname);
    a = a(:,:,1);            %Since image is B/W needs only one of
R,B,G
    a = imcrop(a,[e,f,g,h]); %Crop image as per the handles
    sz = size(a);
 % Intensity calcualtion in the Horizontal
    if (j ==1) %Initialization
        hor(m,sz(2)) = 0;
        ver(n,sz(1)) = 0;
        k(2,sz(2)) = 0;
        q(2,sz(1))=0;
    end
    temp = 3;
    for (i=1:m)
        k(1,:) = a(temp,:);
        hor(m-i+1,:) = hor(m-i+1,:) + k(1,:);
        temp =  temp + fix((sz(1)-10)/(m-1));
    end
 % Intensity calculation in the vertical
     temp = 3;
     for (i=1:n)
        q(1,:) = a(:,temp);
        ver(i,:) = ver(i,:) + q(1,:);
        temp =  temp + fix((sz(2)-10)/(n-1));
     end
 % Set variable to read next file
    l = fname(stseq:enseq);
    l1 = str2num(l) + 1;
    l = num2str(l1);
    sz1 = size(l);
    fname(enseq-sz1(2)+1:enseq) = l(1:sz1(2));
 %
 end
 % Take the average over all the photos as input
 hor = hor/num;
 ver = ver/num;
 %
 hold on;
 figure(1);
 set(1,'name','Intensity Along Vertical lines');
 if (fix(sqrt(n))<sqrt(n))
    vnum  = fix(sqrt(n))+1;
 else
    vnum = sqrt(n);
 end
 %Plotting the values
 u = 'Intensity Variation at';
 for i=1:n
    subplot(vnum,vnum,i), plot(ver(i,:));
    %axis([y1,y2,50,250]);
    xlabel('Vertical Length','Fontsize',12);
    ylabel('Intensity Value','Fontsize',12);
    %Title generation
    u(23:26)= ' x =';
    dns1 = num2str((y1+(y2-y1)*(i-1)/(n-1)),'%22.2f');
```

```
    u(27:(26 +length(dns1))) = dns1(1:length(dns1));
    u(27+length(dns1):27+length(dns1)+3) = ' in.';
    title(u,'FontSize',12)
    %
 end
 figure(2);
 set(2,'name','Intensity Along Horizontal lines');
 if (fix(sqrt(m))<sqrt(m))
     vnum  = fix(sqrt(m))+1;
 else
     vnum = sqrt(m);
 end
  for i=1:m
    subplot(vnum,vnum,i), plot(hor(i,:));
    %axis([x1,x2,175,225]);
    xlabel('Horizontal Length','Fontsize',12);
    ylabel('Intensity Value','Fontsize',12);
    %Title generation
%     u(23:26)= ' y =';
%     dns1 = num2str((x1+(x2-x1)*(i-1)/(m-1)),'%22.2f');
%     u(27:(26+length(dns1))) = dns1(1:length(dns1));
%     u(27+length(dns1):27+length(dns1)+3) = ' in.';
%     title(u,'FontSize',12)
    %
 end
end
```

FUNCTION – GETMAX - Image processing routine for obtaining background fluctuation data

```
function getmax(fname,stseq,enseq,num,xmin,ymin,wid,ht)
M = 0;
a = imread(fname);
a = imcrop(a,[xmin ymin wid ht]);
sz = size(a);
tot = sz(1) * sz(2);
Rej=0;
fname1=fname;
for (j=1:num) % parse for all the images
 % Set variable to read next file
    l = fname(stseq:enseq);
    l1 = str2num(l) + 1;
    l = num2str(l1);
    sz1 = size(l);
    fname(enseq-sz1(2)+1:enseq) = l(1:sz1(2));
 % Read Next file
    b = imread(fname);
    b = imcrop(b,[xmin ymin wid ht]);
 %
    c= b-a;
    %Calculate Mean and standard deviation
    mn = mean(mean(c));
    snd = 0.000;
     for i = 1:sz(1)
```

```
        for j = 1:sz(2)
              snd = snd+(mn - c(i,j))^2;
        end
    end
%

    d = max(max(c));
    e = min(min(c));
    if abs(e) > abs(d)
        d = abs(e);
    end
    if d > M
        M = d;
    end
    [counts,x] = imhist(c);
    cnt = 0;
    for z=1:6
        cnt = cnt + counts(z);
    end
    cnt ;
    perc = (cnt/tot)*100;
   if (perc <= 99)
       Rej = Rej + 1;
   end
end
 M
 mn
 Rej
% stdev
End
```

Script for generating derived quantities from Nigrosine runs :

```
%%%Generate time step and frame info
format long;
for (i=1:1400)
    t(i) = (i-1)/60;
end
tau = t*(7.5e-4*9.81/0.6)^0.5;
%
tau_req = [0.25,0.5,0.75,1,1.25,1.5,1.75,2];
sz = size(tau_req);
t_corresp =  tau_req/((7.5e-4*9.81/0.6)^0.5);
frame_corresp = uint16(t_corresp * 60);
%%%%%%%%%%%%%%%%%%%%
%h vs agtsq
format long;
for (j=1:1400)
for (i=1:278)
    if (f_avg_bub_fin(j,i) > 0.95)
        h(j) = z_top(i);
        break;
    end
end
agtsq(j) =  7.5e-4 * 9.81 * (((j-1)/60)^2);
```

```
end
%%%% Get h at 24 cm
format long;
sz = size(h);
for (i=1:sz(2))
    if (h(i)>24)
        cutoff = i-1;
        h_bkp = h;
        h = h_bkp(1:cutoff);
        agtsq_bkp = agtsq;
        agtsq = agtsq_bkp(1:cutoff)*100;%100 for conversion of g
        break
    end
end
%%%%%%
%Ristocelli - Alpha
format long;
sz = size(h);
for (i=1:(sz(2)-1))
    Alpha(i)  = abs((h(i+1)-h(i))/(1/60))/(4*(7.5e-4)*981*h(i+1));
end
Tau_current = tau(1:sz(2)-1);
%
 for(i=1:sz(2)-1)
     if (Tau_current(i)> 1.67)
         start = i;
         break;
     end
 end
 avg_arr = Alpha(i:(sz(2)-1));
 alp = mean(avg_arr);
%%%%%%%%%%Integral mix width
format long;
dz = z_top(3) - z_top(2);
sz = size(f_avg_bub_fin);
for(i=1:sz(1))
        IMW(i) = 0;
    for (j=1:sz(2))
        IMW(i) = IMW(i) + (f_avg_bub_fin(i,j)*(1-
f_avg_bub_fin(i,j))*dz);
    end
end
IMW = 6*IMW;
%
sz = size(h);
IMW_bkp = IMW;
IMW = IMW_bkp(1:sz(2));
Tau_IMW = tau(1:sz(2));
%Alpha Rist from IMW
format long;
sz = size(IMW);
for (i=1:(sz(2)-1))
    Alpha_IMW(i)  = abs((IMW(i+1)-IMW(i))/(1/60))/(4*(7.5e-
4)*981*IMW(i+1));
end
%
 for(i=1:sz(2)-1)
```

```
    if (Tau_IMW(i)> 1.6)
        start = i;
        break;
    end
end
avg_arr_IMW = Alpha_IMW(i:(sz(2)-1));
alp_IMW = mean(avg_arr_IMW);
```

Script for generating theta using volume fraction and concentration profile data:

```
%For generation of theta and volufraction variance profiles
sz = size(Eq1_avg_res);
x = [0,0.471,0.748,0.986];
x1 = [0,0.2411,0.471,0.758,0.986];
for (i=1:sz(1))
    for (j=1:sz(2))
        %
        y(1) = 0;
        y(2) = Eq3_avg_res(i,j);
        y(3) = Eq2_avg_res(i,j);
        y(4) = Eq1_avg_res(i,j);
        %
%         y1(1) = 0;
%         y1(2) = Eq4_avg_res(i,j);
%         y1(3) = Eq3_avg_res(i,j);
%         y1(4) = Eq2_avg_res(i,j);
%         y1(5) = Eq1_avg_res(i,j);
        %
        coeff = polyfit(x,y,3);
        %coeff1 = polyfit(x1,y1,3);
        coeff2 = polyfit(x,y,2);
       % coeff3 = polyfit(x1,y1,2);

        %
        Intconc(i,j) =
(coeff(1)/4)+(coeff(2)/3)+(coeff(3)/2)+(coeff(4)/1);
       % Intconc1(i,j) =
(coeff1(1)/4)+(coeff1(2)/3)+(coeff1(3)/2)+(coeff1(4)/1);
        Intconc2(i,j) = (coeff2(1)/3)+(coeff2(2)/2)+(coeff2(3)/1);
        %Intconc3(i,j)    (coeff3(1)/3)+(coeff3(2)/2)+(coeff3(3)/1);
        %
        if (nigr_avg_vfrac(i,j)> 0.9 ||nigr_avg_vfrac(i,j)< 0.1)
            Theta(i,j)=0;
         %     Theta1(i,j)=0;
             Theta2(i,j)=0;
           %   Theta3(i,j)=0;
        else
            Theta(i,j) = Intconc(i,j)/(0.96*nigr_avg_vfrac(i,j)*(1-
nigr_avg_vfrac(i,j)));
           % Theta1(i,j) = Intconc1(i,j)/(0.96*nigr_avg_vfrac(i,j)*(1-
nigr_avg_vfrac(i,j)));
            Theta2(i,j) = Intconc2(i,j)/(0.96*nigr_avg_vfrac(i,j)*(1-
nigr_avg_vfrac(i,j)));
```

```
            %Theta3(i,j) = Intconc3(i,j)/(0.96*nigr_avg_vfrac(i,j)*(1-
nigr_avg_vfrac(i,j)));
        end
         if (nigr_avg_vfrac(i,j)> 0.9 ||nigr_avg_vfrac(i,j)< 0.1)
            vfrac_var(i,j)=0;
             %vfrac_var1(i,j)=0;
             vfrac_var2(i,j)=0;
             %vfrac_var3(i,j)=0;
        else
            vfrac_var(i,j) = (1-Theta(i,j))*nigr_avg_vfrac(i,j)*(1-
nigr_avg_vfrac(i,j));
            %vfrac_var1(i,j) =
Intconc1(i,j)/(0.96*nigr_avg_vfrac(i,j)*(1-nigr_avg_vfrac(i,j)));
            vfrac_var2(i,j) = (1-Theta2(i,j))*nigr_avg_vfrac(i,j)*(1-
nigr_avg_vfrac(i,j));
            %vfrac_var3(i,j) =
Intconc3(i,j)/(0.96*nigr_avg_vfrac(i,j)*(1-nigr_avg_vfrac(i,j)));
        end
%         vfrac_var(i,j) =
%         vfrac_var1(i,j) = (1-Theta1(i,j))*nigr_avg_vfrac(i,j)*(1-
nigr_avg_vfrac(i,j));
%         vfrac_var2(i,j) =
%
%         vfrac_var3(i,j) = (1-Theta3(i,j))*nigr_avg_vfrac(i,j)*(1-
nigr_avg_vfrac(i,j));
    end
end
%%%%%%%%%%%%%%%%%%%%%%%%%%%%%%%%
for (i = 1:sz(1))
    for (j=1:sz(2))
    if Theta(i,j) ==0;
        ind_theta(i) = j-1;
        break;
    end
    end
%     for (j=1:sz(2))
%     if Theta1(i,j) ==0;
%         ind_theta1(i) = j-1;
%         break;
%     end
%     end
    for (j=1:sz(2))
    if Theta2(i,j) ==0;
        ind_theta2(i) = j-1;
        break;
    end
    end
%     for (j=1:sz(2))
%     if Theta3(i,j) ==0;
%         ind_theta3(i) = j-1;
%         break;
%     end
%     end
end
%%%%%%%%%%%%%%%%%%%%%%%%%%%%%%%%%%%%%%%%%%%%%%%%
for (i = 1:sz(1))
    for (j=1:sz(2))
```

```
    if vfrac_var(i,j) ==0;
        ind_vfrac_var(i) = j-1;
        break;
    end
    end
%     for (j=1:sz(2))
%     if vfrac_var1(i,j) ==0;
%         ind_vfrac_var1(i) = j-1;
%         break;
%     end
%     end
    for (j=1:sz(2))
    if vfrac_var2(i,j) ==0;
        ind_vfrac_var2(i) = j-1;
        break;
    end
    end
%     for (j=1:sz(2))
%     if vfrac_var3(i,j) ==0;
%         ind_vfrac_var3(i) = j-1;
%         break;
%     end
%     end
end
```

FUNCTION – CALWEDGE_WITHCORR - Image processing routine for dye calibration usogm the wedge.

```
function calwedge_withcorr(fname,stseq,enseq,num,e,f,g,h,conc)
%Function to process set of images to generate Calibration plots
%fname - Starting filename, num- Number of files(To average on)
%e,f,g,h - Cropping handles for the region of interest
%stseq,enseq - Start and end of the sequece number in the filename
string
%num - Number of files
%ht - height of the wedge in cm(end to end)
ht = 58.5;
%tol_top,tol_bot - tolerace to be subtracted from ht to get actual
height
tol_top = 1.5;
tol_bot = 0.5;
%Length of domain
L_dom = 32.7;
%Conc - Concentration of Indicator
% take base mid coumn
 base1 = imread('base.png');  %Enforced
 dom_ext=size(base1); % Domain Extents
 base1 = imcrop(base1,[e f g h]);
 %Logic to pick max values of the base image histogram
 Y = imhist(base1);
 I_0 = 0;
 temp = 0;
 for Y1 = 130:1:256
     if (Y(Y1)>temp);
         temp = Y(Y1);
```

```
          I_0 = Y1-1; %Actual intensity
      end
 end
%Initialization
 sz = size(base1);
 colno  =  fix((sz(2))/2);
 baseV(1,sz(1))=0;  % matrix to record base intensities
 ratV(1,sz(1))=0;   % matrix to record ratios
 vert(1,sz(1)) = 0; %matrix to record intensity from wedge image
 temp(1,sz(1))=0;
 baseV(1,:) = base1(:,colno);
 %
 for (j=1:num) % parse for all the images
    a = imread(fname);
    a = imcrop(a,[e f g h]); %Crop image as per the handles
    sz = size(a);
 %Correct intensity of the image
  for (xa = 1:sz(1))
      for (xb = 1:sz(2))
          I_corr(xa,xb) = (I_0/base1(xa,xb))*a(xa,xb);
      end
  end
  a = I_corr;
  a = cast(a,'double'); %Case unsigned integer to double
 %Note: Only one of the two averaging schemes below should be active

%%%%%%%%%%%%%%%%%%%%%%%%%%%%%%%%%%%%%%%%%%%%%%%%%%%%%%%%%%%%%%%%%%%%%%%%%%%%%%%
 %Averaging Scheme - 1 - Average of Log(I/I_0)
 %Intensity calculation in the vertical
   vert(1,:) = a(:,colno);
 %
 for i=1:sz(1)
 %ratV(1,i) = ratV(1,i) -log(vert(1,i)/baseV(1,i)); %-without
correction
 ratV(1,i) =ratV(1,i) -log(vert(1,i)/I_0); %With correction
 end
 %
 % Set variable to read next file
    l = fname(stseq:enseq);
    l1 = str2num(l) + 1;
    l = num2str(l1);
    sz1 = size(l);
    fname(enseq-sz1(2)+1:enseq) = l(1:sz1(2));
 %
 end
% Take the average over all the photos as input
ratV = ratV/num;
%%%%%%%%%%%%%%%%%%%%%%%%%%%%%%%%%%%%%%%%%%%%%%%%%%%%%%%%%%%%%%%%%%%%%%%%%%%%%%%
%%
% %Averaging Scheme -2 - Avergage of intensity then take the ratio
%   % Intensity calculation in the vertical
%     temp(1,:)=a(:,colno);
%     vert(1,:) = vert(1,:) + temp(1,:);
%      % Set variable to read next file
%      l = fname(stseq:enseq);
%      l1 = str2num(l) + 1;
%      l = num2str(l1);
```

```
%      sz1 = size(1);
%      fname(enseq-sz1(2)+1:enseq) = 1(1:sz1(2));
%   %
%   end
%   vert = vert/num; %Average vertical intensity
%   for i=1:sz(1)
%   %ratV(1,i) =  -log(ver(1,i)/baseV(1,i)); %-without correction
%   ratV(1,i) = -log(vert(1,i)/I_0); %With correction
 %end
%%%%%%%%%%%%%%%%%%%%%%%%%%%%%%%%%%%%%%%%%%%%%%%%%%%%%%%%%%%%%%%%%%%%%%%%%%%%%%%
%PLot
 hold on;
%For x-axis calibration
 % Calibration of the x-axis
 ht_dom_pix = dom_ext(1); % height of the domain in pixels
 strt_pt = f;  %Start point of solution
 for q1 = 1:sz(1)
 ht_dom_act = (strt_pt*ht/ht_dom_pix) -  tol_top;
 %len_act(1,q1)=(ht_dom_act * 103/179)* conc*10e-6/13;-for Nigrosine
 len_act(1,q1)=(ht_dom_act * L_dom/(ht-tol_top-tol_bot)) * conc*1e-6;
 strt_pt = strt_pt + 1;
 end
 %
 plot(len_act,ratV);
end
```

APPENDIX C.
UNCERTAINTY QUANTIFICATION

The uncertainty associated with the experimental measurements was calculated using Kline and McClintock analysis methodology. The method essentially describes the uncertainty in the measurement of a physical quantity R, which is a function of the independent variables (x_1, x_2, x_3, ...x_n), then R = R(x_1, x_2, x_3, ...x_n). Let the uncertainties in each of the independent variables be (w_1, w_2, w_3, ...w_n). Then the uncertainty in the measurement of R, w_R is given by:

$$w_R = \sqrt{\left(\frac{\partial R}{\partial x_1} w_1\right)^2 + \left(\frac{\partial R}{\partial x_2} w_2\right)^2 + \left(\frac{\partial R}{\partial x_3} w_3\right)^2 + \ldots\ldots + \left(\frac{\partial R}{\partial x_n} w_n\right)^2} \qquad \text{(A.1)}$$

This quantification methodology determines the uncertainty associated with single sample measurements. The table below gives a listing of the physical quantities associated with the measurement and their relation to the derived quantities.
The most important primary metrics that are measured directly from the experiment are the concentration values of the fluid in the mixing layer. The value of the normalized, span-integrated concentration is related to the intensity readings from the camera by the Beer-Lambert law (refer section 3 for detailed discussion) as per the relation:

$$C = \frac{\sigma}{\varepsilon L[In]_2} = \frac{\ln(I_0 / I)}{\varepsilon L[In]_2} \qquad \text{(A.2)}$$

The above relation is used for the determination of the normalized concentration in case of the reactive scalar runs and therefore its necessary to evaluate the uncertainty associated with each term in the reactive scalar case. In case of the passive scalar runs the volume fraction, which is normalized by the heavy fluid is directly obtained from the relation:

$$f_1 = [\overline{Dye}]/[Dye]_1 = \ln(I / I_0)/\ln(I_{heavyfluid} / I_0) \qquad \text{(A.3)}$$

Where $I_{heavyfluid}$ is the intensity in the top half of the test section before the start of the experiment and therefore does not involve quantities derived directly from the calibration as they cancel out. The nature of the indicator in this case enables us to evaluate the concentration of the dye heavy fluid from direct intensity measurement which cannot be done in case of the reactive scalar. Therefore the two cases will be dealt separately.

UNCERTAINTIY IN THE REACTIVE SCALAR CONCENTRATION

The uncertainty in the normalized concentration (w_c) is given by:

$$w_c = \sqrt{\left(\frac{\partial C}{\partial I_0} w_{I_0}\right)^2 + \left(\frac{\partial C}{\partial I} w_I\right)^2 + \left(\frac{\partial C}{\partial \varepsilon} w_\varepsilon\right)^2 + \left(\frac{\partial C}{\partial L} w_L\right)^2 + \left(\frac{\partial C}{\partial [In]_2} w_{[In]_2}\right)^2} \qquad (A.4)$$

Uncertainty in the background intensity (w_{I_0}):

The uncertainty in the background intensity is taken by measuring the standard deviation of 500 images. The value has been ascertained to be 1.56 intensity units on a scale of 0-255, with the mean background intensity maintained at a value of 200 units. The uncertainty in the background intensity is therefore ±0.78%.

Uncertainty in the measured intensity (w_I) :

We assume no uncertainty in the measured intensity and that the CMOS sensor scaling of the photons is absolute with repeatable sensitivity to the incident photons for a given scaling range, so $w_I = 0$.

Uncertainty in the Molar absorptivity coefficient (w_L) :

The uncertainty in the width of the test section is ±1 mm and for test section width of 305 mm, , the uncertainty assumes a value of ±0.327%.

Uncertainty in the Indicator concentration ($w_{[In]_2}$) :

The concentration of the chemical indicator is given by the formula:

$$[\mathrm{In}]_2 = NV_2 / V_0 \qquad (A.5)$$

Where N is the normality of the indicator solution which is added to the lower half of the tank, V_2 is the volume of the indicator added and V_0 is the volume of the fluid in the lower half of the tank. The uncertainty in the concentration of phenolphthalein is derived by applying the Kline-McClintock formula as follows:

$$w_{[In]_2} = \sqrt{\left(\frac{\partial [In]_2}{\partial N} w_N\right)^2 + \left(\frac{\partial [In]_2}{\partial V_0} w_{V_0}\right)^2 + \left(\frac{\partial [In]_2}{\partial V_2} w_{V_2}\right)^2} \qquad (A.6)$$

The uncertainty in the normality of the solution as provided by the manufacturer is considered to be 0. The uncertainty in the measurement of V_2 is ± 0.6% as provided by

the manufacturer of the micropipette (Fischer). The uncertainty in the volume of the water in the lower tank is 93 ml and so from the above formula the uncertainty in the concentration of phenolphthalein translates to ±0.67%.

Uncertainty in the Molar absorptivity coefficient (w_ε) :

The molar absorptivity coefficient is ascertained from the absorptivity calibration performed in the tank (refer section 3 for the specifics). The molar absorptivity is estimated in the calibration using the relation:

$$\varepsilon = \frac{\ln(I_0 / I)}{L[In]} \tag{A.7}$$

where *[In]* is the concentration of the solution as measured. The uncertainty in the molar absorptivity coefficient w_ε is given by applying Kline-McClintock to equation A.7 we have

$$w_\varepsilon = \sqrt{\left(\frac{\partial \varepsilon}{\partial I_0} w_{I_0}\right)^2 + \left(\frac{\partial \varepsilon}{\partial I} w_I\right)^2 + \left(\frac{\partial \varepsilon}{\partial L} w_L\right)^2 + \left(\frac{\partial \varepsilon}{\partial [In]} w[In]\right)^2} \tag{A.8}$$

The uncertainties in all the constituent quantities of the above equation have been mentioned earlier. The resulting uncertainty in ε is found to be ±1.23% for phenolphthalein and ±1.5% for Nigrosine.

UNCERTAINTIY IN THE PASSIVE SCALAR CONCENTRATION

The uncertainty in the span averaged volume fraction (w_{f_1}) measured from the passive scalar absorptions is given by :

$$w_{f_1} = \sqrt{\left(\frac{\partial f_1}{\partial I_0} w_{I_0}\right)^2 + \left(\frac{\partial f_1}{\partial I} w_I\right)^2 + \left(\frac{\partial f_1}{\partial I_{heavyfluid}} w_{I_{heavyfluid}}\right)^2} \tag{A.9}$$

Here the uncertainties of the measured intensities are assumed to be zero and so the only standing term driving the uncertainty corresponds to the uncertainty in the background intensity. The resulting uncertainty corresponding to volume fraction is 1.15%.

UNCERTAINTIY IN THE ATWOOD NUMBER

Uncertainty in the Atwood number(A_t) which is a very important flow defining property becomes a very important measurement at low Atwood number due limitations in the precision of the instruments associated with gravimetric measurements of the salt needed to produce the desired density difference. A_t is given by equation 1.3. The corresponding uncertainty is given by:

$$w_{A_t} = \sqrt{\left(\frac{\partial A_t}{\partial \rho_1} w_{\rho_1}\right) + \left(\frac{\partial A_t}{\partial \rho_2} w_{\rho_2}\right)} \qquad \text{(A.10)}$$

The measurement of density was performed using electronic balance corrected with a chrome calibration weight. The uncertainty associated with the balance reading is ±0.005 grams. The density difference is attained by adding the weight of salt required to produce the necessary difference for the entire volume of water in the tank and corrected to the required Atwood number by iterating with the mass of salt added. The density is ascertained from measuring 100ml samples of the liquid from the tanks. The uncertainty in the density of both the fluids is ±0.005%. The uncertainty in the A_t measured is ±0.35 $\times 10^{-4}$ which translates to 4.67% for an operating A_t of 7.5×10^{-4}.

UNCERTAINTIY IN THE SELF-SIMILAR GROWTH CONSTANT (α_b)

The self-similar growth constant reported in the current investigation is calculated using the Ristorcelli and Clark definition given by equation 4.2. The uncertainty (w_{α_b}) is given by:

$$w_{\alpha_b} = \sqrt{\left(\frac{\partial \alpha_b}{\partial \dot{h}_b} w_{\dot{h}_b}\right) + \left(\frac{\partial \alpha_b}{\partial h_b} w_{h_b}\right) + \left(\frac{\partial \alpha_b}{\partial g} w_g\right) + \left(\frac{\partial \alpha_b}{\partial A_t} w_{A_t}\right)} \qquad \text{(A.11)}$$

The value of g is assumed to be 9.81 without any uncertainty. The uncertainty associated with the calculation of h is the same as that associate with the calculation of volume fraction as it is ascertained from fiducial limits on the volume fraction and so is the uncertainty associated with the velocity of the rising bubble. The uncertainty associated with each is therefore ±1.15%. The uncertainty associated with α_b is computed to be ±0.0035 at an A_t of 0.085 which translates to 4.18%.

BIBLIOGRAPHY

1. Kelvin, L., *Hydrokinetic solutions and observations.* Philosophical magazine, 1871. **42**: p. 362.

2. Helmholtz, H.L.F., *Über discontinuierliche Flüssigkeits-Bewegungen.* Monatsberichte der Königlichen Preussiche Akademie der Wissenschaften zu Berlin, 1868. **23**: p. 215.

3. Rayleigh, L., *Investigation of the equilibrium of an incompressible heavy fluid of variable density.* Proceedings of Royal Society of London, 1884. **14**: p. 170-177.

4. Taylor, G.I., *The instability of liquid surfaces when accelerated in a direction perpendicular to their planes I.* . Proceedings of Royal Society of London Series A, 1950. **201**: p. 192-196.

5. Warhaft, Z., *Passive scalars in turbulent flows.* Annual Review of Fluid Mechanics, 2000. **32**: p. 203-240.

6. Dimotakis, P., *Turbulent Mixing.* Annual Review of Fluid Mechanics, 2005. **37**: p. 329-356.

7. Kolmogorov, A., *Local structure of turbulence in an incompressible viscous fluid at very high reynolds numbers.* Dokl. Akad. Nauk SSSR, 1941. **30**: p. 301.

8. Batchelor, G.K., *Small-scale variation of convected quantities like temperature in turbulent fluid Part 1. General discussion and the case of small conductivity.* Journal of Fluid Mechanics, 1959. **5**(01): p. 113-133.

9. Mueschke, N.J., Schilling, Oleg, Youngs, D.L. and Andrews, M.J., *Measurements of Molecular Mixing in a high-Schmidt-number Rayleigh–Taylor Mixing Layer.* Journal of Fluid Mechanics, 2009. **632**: p. 17-48.

10. Cook, A.W., W. Cabot, and P.L. Miller, *The mixing-transition in Rayleigh-Taylor instability.* Journal of Fluid Mechanics, 2004. **511**: p. 333-362.

11. Youngs, D.L., *Application of monotone integrated large eddy simulation to Rayleigh–Taylor mixing.* Philosophical Transactions of the Royal Society A: Mathematical, Physical and Engineering Sciences, 2009. **367**(1899): p. 2971-2983.

12. Lawrie, A.G.W., *On Rayleigh-Taylor mixing:confinement by stratificationand geometry*, in *Department of Applied Mathematics and Theoretical Physics.* 2009, University of Cambridge.

13. Banerjee, A., R.A. Gore, and M.J. Andrews, *Development and validation of a turbulent-mix model for variable-density and compressible flows.* Physical Review E, 2010. **82**: p. 1.

14. Dannevik, W.P., A.C. Buckingham, and C.E. Leith, *Advances in compressible turbulent mixing*. 1992. Medium: ED; Size: 634 p.

15. Smarr, L., Wilson, J.R., Barton, R.T. and Bowers, R.L., *Rayleigh-Taylor overturns in super-nova core collapse.* Astrophysical Journal, 1981. **246**: p. 515-525.

16. Cabot, W.H. and A.W. Cook, *Reynolds number effects on Rayleigh-Taylor instability with possible implications for type-Ia supernovae.* Nature Physics, 2006. **2**: p. 562-568.

17. Cui, A.Q. and R.L. Street, *Large-eddy simulation of coastal upwelling flow.* Environmental Fluid Mechanics, 2004. **4**: p. 197-223.

18. Molchanov, O.A., *On the origin of low- and middler-latitude ionospheric turbulence.* Physics and Chemistry of the Earth, Parts A/B/C, 2004. **29**(4-9): p. 559-567.

19. Marmottant, P. and E. Villermaux, *On spray formation.* Journal of Fluid Mechanics, 2004. **498**: p. 73-111.

20. Lindl, J.D., *Inertial confinement fusion: the quest for ignition and energy gain using indirect drive*. 1998, Berlin: Springer.

21. Betti, R., Umansky, M., Lobatchev, V., Goncharov, V. N. and McCrory, R. L, *Hot-spot dynamics and deceleration-phase Rayleigh-Taylor instability of imploding inertial confinement fusion capsules.* Physics of Plasmas, 2001. **8**: p. 5257-5267.

22. Atzeni, S. and J. Meyer-ter-Vehn, *The physics of inertial fusion : beam plasma interaction, hydrodynamics, hot dense matter*. Oxford science publications. 2004: Clarendon Press

23. Chandrasekhar, S., *Hydrodynamic and hydromagnetic stability*. 2nd ed. 1981, New York: Dover Publications.

24. Linden, P.F., J.M. Redondo, and D.L. Youngs, *Molecular mixing in Rayleigh Taylor instability.* Journal of Fluid Mechanics, 1994. **265**: p. 97-124.

25. Dalziel, S.B., P.F. Linden, and D.L. Youngs, *Self-similarity and internal structure of turbulence induced by Rayleigh-Taylor instability.* Journal of Fluid Mechanics, 1999. **399**: p. 1-48.

26. Cook, A.W. and P.E. Dimotakis, *Transition stages of Rayleigh-Taylor instability between miscible fluids.* Journal of Fluid Mechanics, 2001. **443**: p. 69-99.

27. Youngs, D.L., *Application of MILES to Rayleigh-Taylor and Richtmyer-Meshkov mixing,*, in *16th AIAA Computational Fluid Dynamics Conference, .* 2003: Paper No. AIAA 2003-4102.

28. Dimonte, G., *Dependence of turbulent Rayleigh-Taylor instability on initial perturbations.* Physical Review E, 2004. **69**(5): p. 056305.

29. Ristorcelli, J.R. and T.T. Clark, *Rayleigh-Taylor turbulence: self-similar analysis and direct numerical simulations. .* Journal of Fluid Mechanics, 2004. **507**: p. 213-253.

30. Ramaprabhu, P., G. Dimonte, and M.J. Andrews, *A numerical study of the influence of initial perturbations on the turbulent Rayleigh-Taylor instability.* Journal of Fluid Mechanics, 2005. **536**: p. 285-319.

31. Banerjee, A. and M.J. Andrews, *3-D Simulations to investigate initial condition effects on the growth of Rayleigh-Taylor mixing.* International Journal of Heat and Mass Transfer, 2009. **52**: p. 3906-3927.

32. Drazin, P.G. and W.H. Reid, *Hydrodynamic stability.* 2nd ed. 2004, Cambridge ; New York: Cambridge University Press. xx, 605 p.

33. Youngs, D.L., *Numerical simulation of turbulent mixing by Rayleigh-Taylor instability.* Physica D, 1984. **12**: p. 32-44.

34. Haan, S.W., *Onset of nonlinear saturation for Rayleigh-Taylor growth in the presence of a full spectrum of modes.* Physical Review A, 1989. **39**: p. 5812-5825.

35. Goncharov, V.N., *Analytical Model of Nonlinear, Single-Mode, Classical Rayleigh-Taylor Instability at Arbitrary Atwood Numbers.* Physical Review Letters, 2002. **88**(13): p. 134502.

36. Anuchina, N.N., Kucherenko, Y. A., Neuvazhaev, V. E., Ogibina, V. N., Shibarshov, L. I. and Yakovlev, V. G., *Turbulent mixing at an accelerating interface between liquids of different densities.* Fluid Dynamics, 1978. **13**(6): p. 916-920.

37. Shvarts, D., Alon, U., Ofer, D., McCrory, R. L. and Verdon, C. P., *Nonlinear evolution of multimode Rayleigh-Taylor instability in two and three dimensions.* Physics of Plasmas, 1995. **2**: p. 2465-2472.

38. Rikanati, A., Oron, D., Alon, U. and Shvarts, D., *Statistical mechanics merger model for hydrodynamic instabilities.* Astrophysical Journal Supplement Series, 2000. **127**: p. 451-457.

39. Andrews, M.J. and D.B. Spalding, *A simple experiment to investigate two-dimensional mixing by Rayleigh-Taylor instability.* Physics of Fluids A, 1990. **2**: p. 922-927.

40. Snider, D.M. and M.J. Andrews, *The simulation of mixing layers driven by compound buoyancy and shear.* Journal of Fluids Engineering, 1996. **118**: p. 370-376.

41. Dimonte, G. and M. Schneider, *Density ratio dependence of Rayleigh-Taylor mixing for sustained and impulsive acceleration histories.* Physics of Fluids, 2000. **12**: p. 304-321.

42. Banerjee, A., *Statistically steady measurements of Rayleigh-Taylor mixing in a gas channel*, in *Mechanical Engineering*. 2006, Texas A&M University: College Station, TX.

43. Youngs, D.L., *Three dimensional numerical simulation of turbulent mixing by Rayleigh-Taylor instabilities.* Laser and Particle Beams, 1994. **12**: p. 725-750.

44. Mueschke, N.J., *Experimental and Numerical Study of Molecular Mixing Dynamics in Rayleigh-Taylor Unstable Flows*, in *Mechanical Engineering*. 2008, Texas A&M University: College Station, TX.

45. Mueschke, N.J., M.J. Andrews, and O. Schilling, *Experimental characterization of initial conditions and spatio-temporal evolution of a small Atwood Rayleigh-Taylor mixing layer.* Journal of Fluid Mechanics, 2006. **567**: p. 27-63.

46. Glimm, J. and X.L. Li, *Validation of the Sharp--Wheeler bubble merger model from experimental and computational data.* Physics of Fluids, 1988. **31**(8): p. 2077-2085.

47. Alon, U., Hecht, J., Ofer, D. and Shvarts, D., *Power laws and similarity of Rayleigh- Taylor and Richtmyer-Meshkov mixing fronts at all density ratios.* Physical Review Letters, 1995. **74**: p. 534-538.

48. Young, Y.N., Tufo, H., Dubey, A. and Rosner, R., *On the miscible Rayleigh-Taylor instability: two and three dimensions.* Journal of Fluid Mechanics, 2001. **447**: p. 377-408.

49. SCHMITT, #160, and R. W., *The salt finger experiments of Jevons (1857) and Rayleigh (1880).* Vol. 25. 1995, Boston, MA, ETATS-UNIS: American Meteorological Society.

50. Lewis, D.J., *The instability of liquid surfaces when accelerated in a direction perpendicular to their planes II.* . Proceedings of Royal Society of London Series A, 1950. **202**: p. 81-96.
51. Emmons, H.W., C.T. Chang, and B.C. Watson, *Taylor instability of finite surface waves.* Journal of Fluid Mechanics, 1960. **7**: p. 177-193.

52. Read, K.I., *Experimental investigation of turbulent mixing by Rayleigh-Taylor instability.* Physica D, 1984. **12**: p. 45-58.

53. Kucherenko, Y.A., Shibarshov, L.I., Chitaikin, V.I., Balabin, S.I. and Pylaev, A.P, *Experimental study of the gravitational turbulent mixing self-similar mode.* in *3rd International work-shop on the Physics of Compressible Turbulent Mixing.* 1991. Cambridge University.

54. Dimonte, G. and M. Schneider, *Turbulent Rayleigh-Taylor instability experiments with variable acceleration.* Physical Review E, 1996. **54**: p. 3740-3743.

55. Linden, P.F. and J.M. Redondo, *Molecular mixing in Rayleigh.Taylor instability. Part I: Global mixing.* . Physics of Fluids A, 1991. **3**: p. 1269-1277.

56. Snider, D.M. and M.J. Andrews, *Rayleigh-Taylor and shear driven mixing with an unstable thermal stratification.* Physics of Fluids, 1994. **6**: p. 3324-3334.

57. Banerjee, A. and M.J. Andrews, *Statistically steady measurements of Rayleigh-Taylor mixing in a gas channel.* Physics of Fluids, 2006. **18**: p. 035107.

58. Mueschke, N.J. and O. Schilling, *Investigation of Rayleigh–Taylor turbulence and mixing using direct numerical simulation with experimentally measured initial conditions. I. Comparison to experimental data.* Physics of Fluids, 2009. **21**: p. 014106.

59. Chertkov, M., *Phenomenology of Rayleigh-Taylor Turbulence.* Physical Review Letters, 2003. **91**(11): p. 115001.

60. Vladimirova, N. and M. Chertkov, *Self-similarity and universality in Rayleigh--Taylor, Boussinesq turbulence.* Physics of Fluids, 2009. **21**(1): p. 015102-9.

61. Konrad, J.H., *An experimental investigation of mixing in two-dimensional turbulent shear flows with applications to diffusion-limited chemical reactions.* 1977, CalTech.

62. Breidenthal, R., *Structure in turbulent mixing layers and wakes using a chemical reaction.* Journal of Fluid Mechanics, 1981. **109**: p. 1-24.

63. Koochesfahani, M.M. and P. Dimotakis, *Mixing and chemical reactions in a turbulent liquid mixing layer.* Journal of Fluid Mechanics, 1986. **170**: p. 83-112.

64. Shea, J.R., *A chemical reaction in a turbulent jet.* Journal of Fluid Mechanics, 1977. **81**: p. 317-333.

65. Zhang, S., P. Schneider, and S.H. Collicott, *Quantitative molecular-mixing measurements using digital processing of absroption images.* Experiments in Fluids, 1995. **19**: p. 319-327.

66. Banerjee, A., W.N. Kraft, and M.J. Andrews, *Detailed measurements of a statistically steady Rayleigh-Taylor mixing layer from small to high Atwood numbers.* Journal of Fluid Mechanics, 2010. **659**(-1): p. 127-190.

67. White, J., Oakley, Jason, Anderson, Mark and Bonazza, Riccardo, *Experimental measurements of the nonlinear Rayleigh-Taylor instability using a magnetorheological fluid.* Physical Review E, 2010. **81**(2): p. 026303.

68. Olson, D.H. and J.W. Jacobs, *Experimental study of Rayleigh-Taylor instability with a complex initial perturbation.* Physics of Fluids, 2009. **21**: p. 034103.

69. Livescu, D. and J.R. Ristorcelli, *Buoyancy-driven variable density turbulence.* Journal of Fluid Mechanics, 2007. **591**: p. 43-71.

70. Dimonte, G., Youngs, D.L.,Dimits, A., Weber, S., Marinak, M., Wunsch, S., Garasi, C., Robinson, A., Andrews, M.J., Ramaprabhu, P., Calder, A.C., Fryxell, B., Biello, J., Dursi, L., MacNeice, P., Olson, K., Ricker, P., Rosner, R., Timmes, F., Tufo, H., Young, Y.N. and Zingale, M, *A comparative study of the turbulent Rayleigh-Taylor (RT) instability using high-resolution 3D numerical simulations: The Alpha-Group collaboration,.* Physics of Fluids, 2004. **16**: p. 1668-1693.

71. Ramaprabhu, P. and M.J. Andrews, *Experimental investigation of Rayleigh-Taylor mixing at small Atwood numbers.* Journal of Fluid Mechanics, 2004. **502**: p. 233-271.

72. Andrews, M.J., *Turbulent mixing by Rayleigh-Taylor instability*, in *Mechanical Engineering*. 1986, Imperial College: London.

73. Lane-Serff, G.F., *Heat flow and air movement in buildings.*, in *Mechanical Engineering*. 1989, University of Cambridge: Cambridge.

74. Ramaprabhu, P. and M.J. Andrews, *Simultaneous measurement of velocity and density in buoyancy driven mixing.* Experiments in Fluids, 2003. **34**: p. 98-106.

75. Hecht, E., *Optics* 4th ed. 2002: Addison Wesley.

76. Andrews, M.J., *Accurate Computation of Convective Transport in Transient Two-Phase Flow.* International Journal for Numerical Methods in Fluids 1995. **21**(3): p. 205-222.

77. Ramaprabhu, P. and M.J. Andrews, *On the initialization of Rayleigh-Taylor simulations.* Physics of Fluids, 2004. **16**: p. L59-L62.

78. Danckwerts, P., *The definition and measurement of some characteristics of mixtures.* Applied Scientific Research, 1952. **3**(4): p. 279-296.

VITA

Lakshmi Ayyappa Raghu Mutnuri was born in Amalapuram, India on 16th December, 1983. He received his B.Tech in Mechanical Engineering from Pondicherry University, Pondicherry, India in May, 2005. He then worked at Infosys Technologies Ltd as a software engineer till July 2008. In August 2008, he joined Missouri University of Science and Technology (formerly University of Missouri, Rolla) as a graduate research assistant. He received his M.S. degree in Mechanical Engineering from the Missouri University of Science and Technology, Rolla, Missouri, USA, in Spring 2011.He is a member of American Physical Society (APS) since 2010.